Study of the crystal and magnetic structures of the quasi-one-dimensional iron-based superconductor BaFe Se

Wen-Gen Zheng

université PARIS-SACLAY

Study of the crystal and magnetic structures of the quasi-one-dimensional iron-based superconductor $BaFe_2Se_3$

Étude des structures cristalline et magnétique du supraconducteur à base de fer quasi unidimensionnel $BaFe_2Se_3$

Thèse de doctorat de l'université Paris-Saclay

École doctorale n°564 Physique en Île-de-France (PIF)
Spécialité de doctorat: Physique
Graduate School: Physique. Référent: Faculté des sciences d'Orsay

Thèse préparée dans l'unité de recherche **Laboratoire de Physique des Solides** (Université Paris-Saclay, CNRS), sous la direction de **Pascale FOURY-LEYLEKIAN**, professeure, et le co-encadrement de **Victor BALÉDENT**, Maître de Conférences.

Thèse soutenue à Paris-Saclay, le 5 juillet 2022, par

Wen-Gen ZHENG

Composition du jury

Fabrice BERT Professeur, Université Paris-Saclay	Président
Fabienne DUC Chargée de recherche (HDR), Laboratoire National des Champs Magnétiques Intenses, Toulouse	Rapporteure & Examinatrice
Andrea GAUZZI Maître de Conférences (HDR), Sorbonne Université	Rapporteur & Examinateur
Béatrice GRENIER Maître de Conférences, Université Grenoble Alpes	Examinatrice
Pascale FOURY-LEYLEKIAN Professeure, Université Paris-Saclay	Directrice de thèse

THESE DE DOCTORAT

NNT : 2022UPASP063

université PARIS-SACLAY | ÉCOLE DOCTORALE Physique en Île-de-France (PIF)

Titre : Étude des structures cristalline et magnétique du supraconducteur à base de fer quasi unidimensionnel $BaFe_2Se_3$

Mots clés : multiferroïque, supraconductivité, structure magnétique, $BaFe_2Se_3$

Résumé : Il a été récemment observé qu'une phase supraconductrice (SC) émerge sous pression dans les échelles de spin à base de Fe $BaFe_2Se_3$. La faible dimensionnalité des échelles de spin, qui simplifie l'élaboration de modèles théoriques, devrait aider à comprendre le mécanisme de supraconductivité. De plus, en dessous de 250 K, une multiferroïcité a été promise dans $BaFe_2Se_3$. La compétition ou la coopération entre ces deux ordres est au coeur de mon travail de thèse.

Dans cette thèse, nous avons étudié la structure cristalline polaire de $BaFe_2Se_3$ par les mesures de diffraction des rayons X sur monocristal. De plus, un couplage magnétoélectrique est observé dans les mesures diélectriques. Nous avons ensuite étudié l'évolution de la structure magnétique avec l'augmentation de la pression. En utilisant la technique de diffraction des neutrons sur monocristal, nous avons déterminé le groupe d'espace magnétique C_am, compatible avec la structure magnétique du Bloc-A. Par ailleurs, un ordre magnétique de type parapluie a été déterminé à pression ambiante. En revanche, une transition magnétique du type bloc vers un type bande a été observée à environ 3 GPa par les mesures de diffraction neutronique sur poudre. Cet ordre magnétique de bande a persisté jusqu'à 7,7 GPa. Notre découverte montre que l'ordre magnétique de type stripe est une phase cruciale à proximité du dôme SC. Les fluctuations magnétiques particulières de cet ordre de bande pourraient être impliquées dans la stabilisation de la supraconductivité dans ces échelles de spin à base de Fe. Ce tout nouvel archétype de supraconducteur pourrait frayer la voie à de nouveaux efforts de recherche théorique.

Title: Study of the crystal and magnetic structures of the quasi-one-dimensional iron-based superconductor $BaFe_2Se_3$

Keywords: multiferroic, superconductivity, magnetic structure, $BaFe_2Se_3$

Abstract: It has been recently observed that a superconducting (SC) phase emerges under pressure in the Fe-based spin-ladders $BaFe_2Se_3$. The low dimensionality of the Fe spin-ladders, which simplifies the elaboration of theoretical models, should help to understand the mechanism of superconductivity. Besides, a multiferroicity was predicted to emerge in $BaFe_2Se_3$ below 250 K.

In this thesis, we have investigated the polar crystal structure of $BaFe_2Se_3$ by the single-crystal X-ray diffraction measurements. In addition, a magnetoelectric coupling is observed in the capacitance measurements. We then have studied the evolution of the magnetic structure with increasing pressure. Using the single-crystal neutron diffraction technique, a space group of C_am compatible with the Block-A magnetic structure was identified. Besides, an umbrella-type magnetic order was determined at ambient pressure. On the other hand, a magnetic transition from the block type to a stripe type was observed around 3 GPa by powder neutron diffraction measurements. This stripe magnetic order persisted up to 7.7 GPa. Our discovery shows that the stripe magnetic order is a crucial phase close to the SC dome. The particular magnetic fluctuations of this stripe order could be involved in the stabilization of superconductivity in Fe-based spin ladders. This very new archetype of superconductor could pave the way to further theoretical research efforts.

This thesis is dedicated to my parents.
谨以此论文献给我的父母。

Acknowledgment

Standing at the end of my doctoral life and looking back, my heart is full of gratitude. As an ordinary young man born in a small Chinese village, in the first twenty years of my life, I never imagined that I could go abroad in the future. These four years in France will become a fond memory for me and benefit me for the rest of my life. I thus sincerely thank those who have accompanied me on this journey.

First and foremost, I want to thank my primary supervisor Pascale Foury-Leylekian for offering me this precious opportunity. Besides, she has shown me all the good characteristics of a scientist: honesty, deliberation, enthusiasm, diligence, curiosity, and so on. Without her support and wise perspective, this study and many others not mentioned in this thesis would never have been achieved.

Similar gratitude belongs to my co-supervisor, Victor Balédent, who dedicates his whole heart to academic research. I have learned a lot from him, not only the knowledge about the techniques of X-rays and neutrons but also his enthusiasm for science. He and Pascale nurtured my passion for physics and encouraged me to pursue my academic career.

I would like to thank Béatrice Grenier and Fabrice Bert to be part of my jury. Special thanks to Fabienne Duc and Andrea Gauzzi for being the reviewers of this manuscript. It is a great pleasure to present my work to you all.

I also want to thank our collaborators. I would like to thank Dorothée Colson and Anne Forget for synthesizing samples for us. Without their high-quality samples, my study would have been in vain initially. I thank Françoise Damay, Claire Colin, and Eric Ressouche for their help on neutron experiments. Special thanks should be given to Pierre Fertey for helping us perform the synchrotron diffraction experiments and teaching me the crystallographic knowledge. I also thank Pascal Retailleau for the excellent single-crystal X-ray diffraction experiments.

Furthermore, I want to thank other members of LPS. Many thanks to Pascale Senzier, Jean-Pierre Dalac, Claude Pasquier, and Miguel Monteverde for their experimental support of SQUID and PPMS. I would like to thank Véronique Thieulart, Ciham Zaaboul-Aliane, Marie-France Mariotto, and Sabine Hoarau for all the administrative support. Meanwhile, I need to thank my lovely MATRIX group: Pascale Launois, Pierre-Antoine Albouy, Erwan-Nicolas Paineau, Stéphane Cabaret, Gilles Guillier, Yifan Pan, and Stéphane Rouziere. Everyone in the group is so kind. I also thank my parrain Véronique Brouet and my tutor Edwin Kermarrec for their concern and encouragement.

我要感谢我的父母，感谢他们的无私奉献，感谢他们能够迁就我的学术理想。我还要感谢我的大姑，由于她，我才能够有机会去市里上初中。那是我一切幸运的开始。同时，感谢读博期间相互扶持的好哥们：闫兴成，刘荣兴，陈有为，喻云亮，还有不辞辛苦帮我审稿的朱云峰。当然，我还要感谢胡蕴华，没有你我就遇不到我亲爱的杨菁菁。最后，我要感谢现在已经是我的未婚妻的杨菁菁，感谢你爱着我。

And finally, I would like to thank the China Scholarship Council (CSC) for funding my Ph.D. study. This opportunity is priceless for me.

Contents

List of Abbreviations

ADP:	atomic displacement parameter
AFM:	antiferromagnetic
CuSC	cuprates superconductor
EOS:	equation of state
DAC:	diamond anvil cell
DFT:	density functional theory
FeSC:	iron-based superconductor
FM:	ferromagnetic
HTSC:	high-temperature superconductor
INS:	inelastic neutron scattering
ME:	magnetoelectric
n-PDF:	neutron pair-distribution function
PND:	powder neutron diffraction
SC:	superconducting
SEM:	Scanning Electron Microscope
SHG:	second harmonic generation
STEM:	Scanning Transmission Electron Microscope
VRH:	variable-range-hopping
XES:	x-ray emission spectroscopy
μSR:	muon spin relaxation

Introduction

In the last decades, the studies of multiferroicity and superconductivity laid at the center of condensed matter physics. The multiferroic materials can present strong magnetoelectric (ME) couplings, and thus novel functionalities could emerge. One example is the control of the magnetic properties by electric fields and vice versa. This can be applied in the field of energy or information technology. However, multiferroicity usually arises from electronic correlations at a microscopic level. Due to the quantum nature of their origin, such properties often appear at low temperatures, drastically restricting their potential applications. Therefore, the discovery of new materials with nearby room temperature transitions is of particular interest.

On the other hand, the recent discovery of iron-based superconductors appeals a new description of the superconductivity mechanism. The intimate relationship between magnetism and superconductivity is still puzzling. One obstacle is that the quantitative comparison between experimental and theoretical results is still a challenge since the exact solution of many-body Hamiltonians in two and three dimensions remains unclear. One potential route to conquer this difficulty is the analysis of quasi-one-dimensional systems. Such possibilities have been recognized in theory, but the lack of suitable experimental materials has hindered further investigation.

Recently, a superconducting phase was observed in the quasi-one-dimensional iron chalcogenides $BaFe_2Se_3$ under pressure (above 10 GPa) and below 14 K [1]. Besides, a multiferroic state was predicted below a high Néel temperature (250 K), which makes $BaFe_2Se_3$ an ideal candidate to experimentally study and use the multiferroic character [2]. In $BaFe_2Se_3$, the iron atoms of each unit cell form two ladders built by two edge-sharing $FeSe_4$ tetrahedra chains [3]. An exotic block-like magnetic order was determined below T_N [4, 5]. The study of this ladder compound could provide useful information to better confront theory with experiments like in cuprates ladders [6]. However, the correct crystal and magnetic structures of $BaFe_2Se_3$ were missing before the present work. In particular at the boundary of the magnetic and the superconducting phases. This prevents the accurate theoretical study related to the roles of magnetic fluctuations in stabilizing the superconductivity in $BaFe_2Se_3$.

This thesis will focus on the crystal and magnetic structures of $BaFe_2Se_3$. In Chapter 1, a short introduction of superconducting materials, as well as the basic concepts of multiferroic materials, are given. Chapter 2 is devoted to the presentation of the state of the art of $BaFe_2Se_3$. Then, we describe the principles and techniques of X-ray and neutron diffraction in Chapter 3. Several tools used in this work to analyze the data are also introduced. The main results of our study are reported in Chapters 4 and 5. The former focuses on the crystal structure and the multiferroic properties at ambient pressure, while the latter presents the study of the magnetic structures at different pressures.

Résumé en français

Au cours des dernières décennies, les études de la multiferroïcité et de la supraconductivité ont été au centre de la physique de la matière condensée. Généralement, si plusieurs états ferroïques coexistent simultanément dans un matériau, ce matériau peut être appelé matériau multiferroïque. En outre, les états ferroïques peuvent être couplés les uns aux autres dans certains matériaux multiferroïques, comme le montre la figure 1. Par conséquent, l'état interne peut être contrôlé par un autre paramètre externe, tel que l'utilisation du champ électrique pour contrôler le magnétisme, et vice versa. Parmi ces couplages, le couplage magnétoélectrique est le plus étudié et a de nombreuses applications. Selon les différents mécanismes microscopiques de la ferroélectricité, il existe deux groupes de multiferroïques, que nous appelons multiferroïques Type-I et Type-II. Pour les composés multiferroïques de Type-I, la ferroélectricité et le magnétisme ont des sources différentes et se stabilisent indépendamment. Bien qu'il existe également un certain couplage entre la ferroélectricité et le magnétisme dans ces matériaux de Type-I, il est généralement très faible. Au début de ce siècle, une nouvelle classe de multiferroïques a été découverte, appelée multiferroïques de type II. Ce sont des systèmes dans lesquels la ferroélectricité est générée par des états magnétiquement ordonnés, impliquant un fort couplage entre les deux ordres ferroïques. Ces matériaux attirent énormément l'attention en raison des questions fondamentales qu'ils soulèvent.

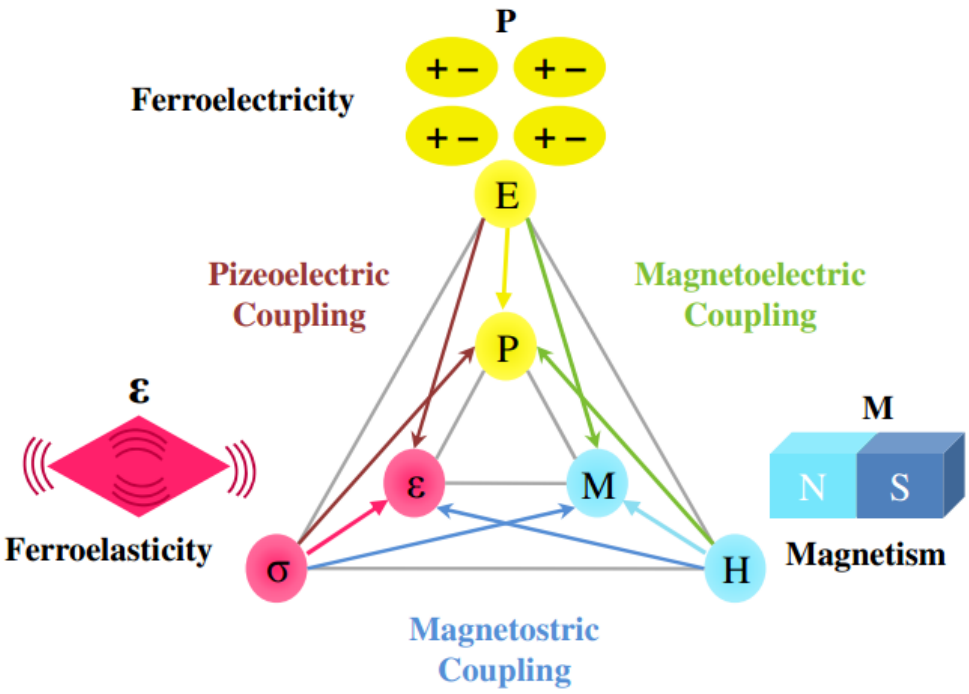

Figure 1: Le champ électrique **E**, le champ magnétique **H** et le contrôle des contraintes de la polarisation électrique **P**, de l'aimantation **M** et de la déformation δ, respectivement. Dans un matériau ferroïque, **P**, **M** ou ϵ se forment spontanément pour produire respectivement du ferromagnétisme, de la ferroélectricité ou de la ferroélasticité. [7]

D'autre part, la supraconductivité est bien connue en raison de son extraordinaire potentiel d'application, comme les aimants supraconducteurs dans l'imagerie par résonance magnétique (IRM). Cependant, seuls quelques supraconducteurs découverts ont un T_C supérieur à 77 K qui est le point d'ébullition de l'azote liquide. Parmi eux, les supraconducteurs à base de cuivre et à base de fer sont les candidats les plus prometteurs pour les applications car ils peuvent afficher une supraconductivité à pression ambiante. Comme le montre la figure 2, la supraconductivité dans ces deux familles émerge toutes deux de la déstabilisation de l'ordre antiferromagnétique. Cependant, la relation intime entre l'antiferromagnétisme et la supraconductivité reste déconcertante. Un obstacle est que la comparaison quantitative entre les résultats expérimentaux et théoriques reste un défi puisque la solution exacte des hamiltoniens à plusieurs corps en deux et trois dimensions est difficile. Une voie potentielle pour surmonter cette difficulté est l'analyse de systèmes quasi unidimensionnels. Mais le manque de matériaux appropriés a limité les investigations jusqu'à aujourd'hui.

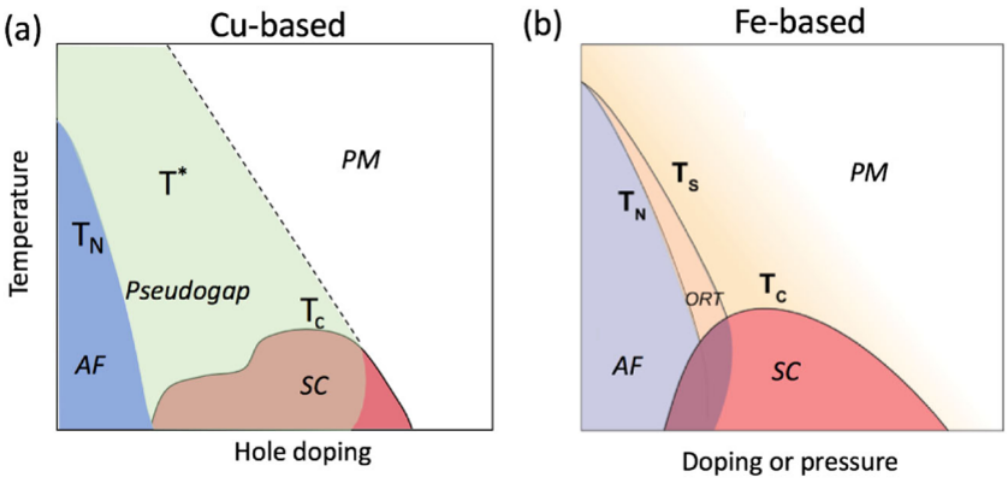

Figure 2: Diagrammes de phase des familles de supraconducteurs à base de cuivre (a) et à base de fer (b).

Récemment, une phase supraconductrice a été observée dans le chalcogénure de fer quasi unidimensionnels $BaFe_2Se_3$ sous pression (supérieure à 10 GPa) et au-dessous de 14K [1]. De plus, un état multiferroïque a été prédit au-dessous de la température de Néel qui est très élevée dans ce composé (250 K). Ceci fait d'une température élevée de Néel (250 K), ce qui fait de $BaFe_2Se_3$ un candidat idéal pour étudier expérimentalement et utiliser le caractère multiferroïque [2]. Comme le montre la figure 3, dans $BaFe_2Se_3$, les atomes de fer de chaque cellule unitaire forment deux échelles construites par deux chaînes de tétraèdres $FeSe_4$ à arêtes partagées [3]. De plus, un ordre magnétique de type bloc exotique a été déterminé sous T_N [4, 5]. L'étude de ce composé à échelle de spins pourrait fournir des informations utiles pour mieux confronter les mécanismes microscopiques à l'origine de la multiferroicité et de la supraconductivité [6]. Cependant, les structures cristallines et magnétiques correctes de $BaFe_2Se_3$ manquaient avant le présent travail. En particulier à la frontière des phases magnétique et supraconductrice. Cela empêche l'étude théorique précise liée aux rôles des fluctuations magnétiques dans la stabilisation de la supraconductivité.

Cette thèse a porté sur l'étude de $BaFe_2Se_3$ dans laquelle la multiferroïcité et la supraconductivité sont observées. Le chapitre 1 est consacré à des connaissances générales sur la multiferroïcité et la supraconductivité. Pour la section multiferroïcité, une brève introduction aux multiferroïques est d'abord présentée. Ensuite, trois types de multiferroïques (Type-I, Type-II et composite) sont introduits, suivis de plusieurs mécanismes de multiferroïcité. Dans la partie supraconductivité, un bref historique de la supraconductivité est donné. Ensuite, les supraconducteurs à haute température (HTSC), en particulier les supraconducteurs cuprate (CuSC) et les supraconducteurs à base de fer (FeSC), sont discutés en détail.

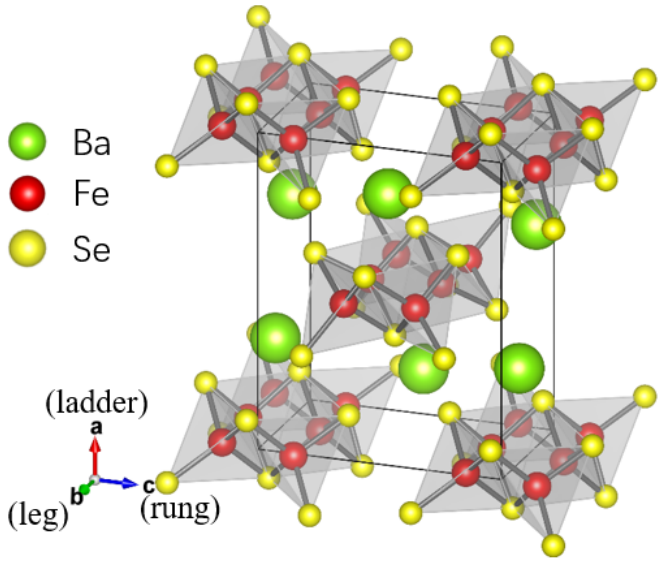

Figure 3: Structure cristalline de $BaFe_2Se_3$.

Dans le chapitre 2, je présent l'état de l'art concernant le système à échelle de spin quasi-1D $BaFe_2Se_3$. Récemment, la supraconductivité et la multiferroïcité ont été observé dans $BaFe_2Se_3$, ce qui suscite beaucoup d'intérêt [1, 2]. Une courte introduction su système est donnée dans Section 2.1. La Section 2.2 présente l'évolution de la structure cristalline et sa variation en fonction de la temp et de la pression. Dans la Section 2.3, les propriétés électriques et magnétiques de $BaFe_2Se_3$ sont introduites. Ensuite, les structures magnétiques sont discutées dans la Section 2.3.2. Dans la dernière section, l'influence de la substitution chimique dans $BaFe_2Se_3$ est détaillée.

L'objectif principal de notre travail est d'étudier la structure cristalline et magnétique de $BaFe_2Se_3$. Par conséquent, les techniques de diffusion des rayons X et des neutrons sont largement utilisées dans cette thèse. Leurs grands principes sont présentés au chapitre 3. La section 3.1 est consacrée à l'introduction de la théorie de base de la diffusion des rayons X et des neutrons. La section 3.2 et la section 3.3 présentent respectivement certaines connaissances communes en cristallographie et en diffraction. Les applications expérimentales des rayons X et des neutrons sont données respectivement dans la section 3.4 et la section 3.5. Ensuite, plusieurs outils d'analyse de données sont introduits dans la section 3.6. Enfin, nous présentons la synthèse et la caractérisation de nos échantillons dans la section 3.7.

Dans le chapitre 4, la structure cristalline de $BaFe_2Se_3$ à pression ambiante est étudiée par analyse de groupe d'espace et mesure de diffraction des rayons X sur monocristal. Le groupe d'espace non polaire $Pnma$, proposé dans la littérature antérieure, est exclu. Nous montrons que le système présente déjà une structure polaire avec le groupe d'espace $Pmn2_1$ à 300 K et est donc ferroélectrique. Les deux échelles de Fe issues de l'affinement de structure dans le groupe de $BaFe_2Se_3$ issues du raffinement dans le groupe d'espace $Pmn2_1$ à 300 K sont représentées sur la figure 4(a). Comme on peut le voir, il n'y a pas de centres d'inversion dans les échelles, ce qui permet une géométrie non centrosymétrique et pourrait produire une polarisation électrique dans le composé. De plus, nous notons qu'à 150 K, c'est-à-dire au-dessous de la transition de Néel, les déplacements de Fe sont plus grands [Fig. 4(b)]. Par conséquent, la polarisation pourrait être renforcée par l'ordre antiferromagnétique. Par ailleurs, un effet magnétoélectrique à 24 K est observé par la mesure de la capacité en fonction du champ magnétique. Ces caractéristiques prouvent sans ambiguïté le caractère multiferroïque de $BaFe_2Se_3$ tel que proposé théoriquement [2].

Le chapitre 5 s'intéresse à la détermination des structures magnétiques de $BaFe_2Se_3$ à différentes

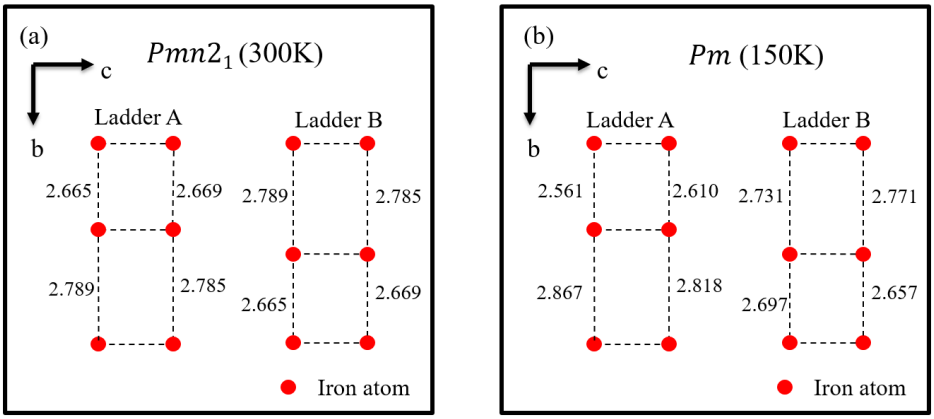

Figure 4: (a) Les échelles de fer issues de l'affinement des données à 300 K avec le groupe d'espace $Pmn2_1$. (b) Les échelles de fer issues de l'affinement des données à 150 K avec le groupe d'espace Pm.

pressions. Dans la section 5.2, une structure magnétique en forme de parapluie a été révélée à pression ambiante par diffraction des neutrons sur monocristal et analyse de la symétrie. Nous avons déterminé le groupe magnétique C_am, qui correspond à un ordre magnétique Block-A. Une inclinaison du moment dans les plans ac et bc a été révélée. De plus, les moments inclinés ont été confirmés par diffusion de neutrons polarisés. Dans la section 5.3, nous avons étudié la frontière entre les phases magnétique et supraconductrice (SC) en effectuant des mesures de diffusion de neutrons sur poudre et de spectroscopie d'émission de rayons X au seuil du Fe K_β (XES) sous pression. Nous avons montré que l'état fondamental à pression ambiante avec un ordre magnétique en forme de bloc est déstabilisé sous pression et remplacé par un nouvel ordre. De plus, nous avons mis en évidence que le moment magnétique local persistait jsuqu'à la phase supraconductrice voire même au-delà.

D'autre part, nos résultats sont étayés par des calculs DFT [8]. Malgré un désaccord entre la pression critique mesurée et prédite, ce résultat théorique a prouvé que, du point de vue énergétique, la phase magnétique CX est proche de l'état fondamental avec une pression suffisante. Plus intéressant encore, pour le composé parent $BaFe_2S_3$, un ordre magnétique de bande très similaire est l'état fondamental à pression ambiante et persiste jusqu'à 10 GPa, à laquelle la supraconductivité émerge [9, 10]. La bibliothèque m'a obligé à écrire un résumé de cinq pages en français. Mais, je ne peux écrire que quatre pages. Par conséquent, certains paragraphes ne sont certainement pas bons. Je suis vraiment désolé pour ça. Les composés $BaFe_2X_3$ (X=Se,S) devraient présenter un mécanisme supraconducteur très similaire puisque leurs structures cristallographiques et magnétiques sont quasi-identiques près de la phase SC. De plus, une substitution isoélectronique au site Se agit comme une pression chimique et ne devrait pas affecter fortement les mécanismes de stabilisation des différents états fondamentaux au sein du diagramme de phase. La stabilisation de la phase magnétique de la bande universelle dans les échelles de spin Fe sous pression est d'un grand intérêt en raison de sa proximité avec le dôme SC. Compte tenu de l'état de l'art des cuprates et dans le contexte actuel de la découverte de la supraconductivité dans les matériaux ferromagnétiques à base d'U tels que UGe_2 [11] et UCoGe [12], on peut prévoir l'importance des fluctuations magnétiques dans le mécanisme SC des échelles de spin Fe.

Sur la base de nos études, le diagramme de phase température-pression (P-T) de $BaFe_2Se_3$ peut être extrait [Fig. 5(a)]. L'ordre magnétique en bloc se déstabilise rapidement avec la pression croissante. Au contraire, l'ordre magnétique en stripe CX est robuste, ressemblant à l'ordre AFM de stripe dans le composé parent $BaFe_2S_3$ [Fig. 5(b)]. La stabilisation de la phase magnétique de la stripe universelle dans les échelles de spin Fe sous pression est d'un grand intérêt en raison de sa proximité avec le dôme SC. Compte tenu de l'état de l'art des cuprates et dans le contexte actuel de la découverte de la supraconductivité dans les matériaux ferromagnétiques à base d'U tels que UGe_2 [11] et UCoGe [12], on peut prévoir l'importance des fluctuations magnétiques dans le mécanisme SC des échelles de spin

Fe. Par conséquent, les fluctuations magnétiques et la dynamique qui pourraient être impliquées dans le mécanisme SC des échelles de spin $BaFe_2X_3$ (X=S,Se), étant associées à cette phase CX universelle, sont nécessairement situées autour de k=($\frac{1}{2}$, 0, $\frac{1}{2}$).

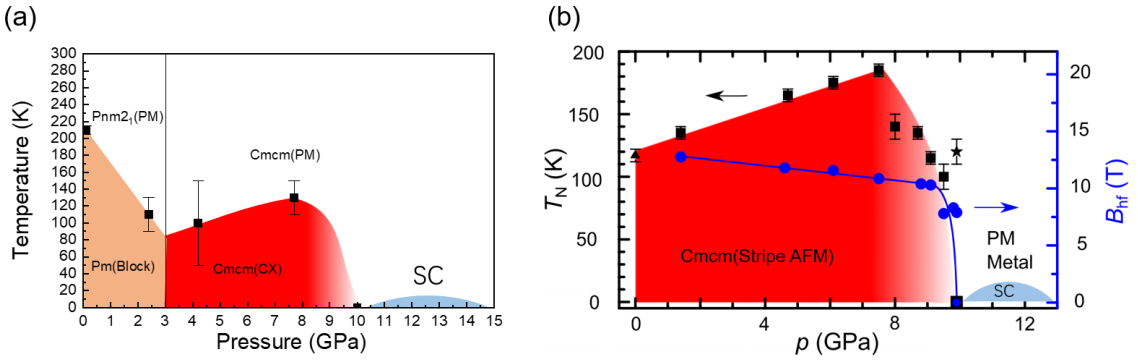

Figure 5: (a) Diagramme de phase de $BaFe_2Se_3$ obtenu à partir de nos résultats. (b) Diagramme de phase de $BaFe_2S_3$ obtenu par spectroscopie synchrotron Mössbauer de référence [10]. L'axe de gauche représente la température de Néel tandis que l'axe de droite est le champ hyperfin magnétique à basse température.

Cette thèse a mis en évidence plusieurs propriétés et ouvert un très large champ d'investigations passionnantes sur le composé à échelle de spin $BaFe_2Se_3$. Le premier problème concerne la structure cristallographique exacte sous pression. Cela peut se faire via un nouveau cryostat développé par notre équipe, installé sur la ligne de lumière CRISTAL du synchrotron SOLEIL. Ce cryostat est capable de faire tourner les cellules de pression selon deux axes et permet ainsi l'enregistrement d'un grand nombre de réflexions de Bragg, nécessaires à l'affinement fin de la structure.

Une autre perspective concerne tous les composés dopés de la série $BaFe_{1-x}M_xB_3$, où M peut être n'importe quel ion métallique et B est un chalcogénure. Nous avons commencé ce travail en dopant avec M = Ni, Co. Les résultats sont encore partiels mais peuvent ouvrir un immense champ d'investigation, qui pourrait conduire à des propriétés très intéressantes en terme de supraconductivité ou en terme de multiferroïcité à température ambiante.

Enfin, tout l'aspect concernant les propriétés inélastiques n'a pas été étudié dans le présent travail. Des biens très originaux sont attendus. En particulier, il serait intéressant d'étudier l'électromagnon, une excitation hybride encore mal connue et spécifique aux systèmes magnéto-électriques. C'est une excitation magnétique électro-active.

1

Multiferroicity and Superconductivity

Contents

This chapter is devoted to give general knowledge about multiferroicity and superconductivity. For the multiferroicity section, a short introduction of multiferroics is first presented. Then, three types of multiferroics (Type-I, Type-II, and composite) are introduced, followed by several mechanisms of multiferroicity. In the superconductivity part, a brief history of superconductivity will be given. Then, the high-temperature superconductors (HTSCs), particularly the cuprate superconductors (CuSCs) and iron-based superconductors (FeSCs), will be discussed in detail.

1.1 Multiferroicity

The term "multiferroic" was created by Hans Schmid in 1994 to define the materials in which more than one primary ferroic state coexists in one phase [13]. By now, four primary ferroic states have been discovered: ferromagnetism, ferroelectricity, ferroelasticity, and ferrotoroidicity [13, 14]. In ferromagnets, a non-vanishing magnetic moment (M), i.e., spontaneous magnetization, emerges because of the alignment of spins in the absence of magnetic field. This spontaneous magnetization can be switched by an external magnetic field [Fig. 1.1(a)]. The most famous ferromagnetic materials are magnetite (Fe_3O_4) and iron. Analogous to ferromagnets, ferroelectric materials present a spontaneous electric polarization (P) that can be reversed by an electric field [Fig. 1.1(b)]. On the other hand,

ferroelasticity is a phenomenon in which a material may exhibit a spontaneous strain. In ferroelastic materials, the crystal has at least two stable orientation states which are switchable by applying mechanical stress. When external stress is applied to a ferroelastic material, one can observe a hysteretic behavior in the strain-stress curve [Fig. 1.1(c)]. As for ferrotoroidicity, a toroidization (T) is generated by a vortex of magnetic moments [Fig. 1.1(d)]. Meanwhile, the toroidization can be switched by a toroidal field defined as $E \times H$, where E and H are the external electric and magnetic fields, respectively. Nowadays, the terminology multiferroics are extended to more compounds such as antiferromagnets and composite materials like laminates and layered (thin film) architectures [15–19]. Among all the multiferroic materials, magnetoelectric (ME) multiferroics attract worldwide interest because of the potential application of the electric and magnetic coupling in them. This coupling enables the control of magnetic order by an electric field, and vice versa [16].

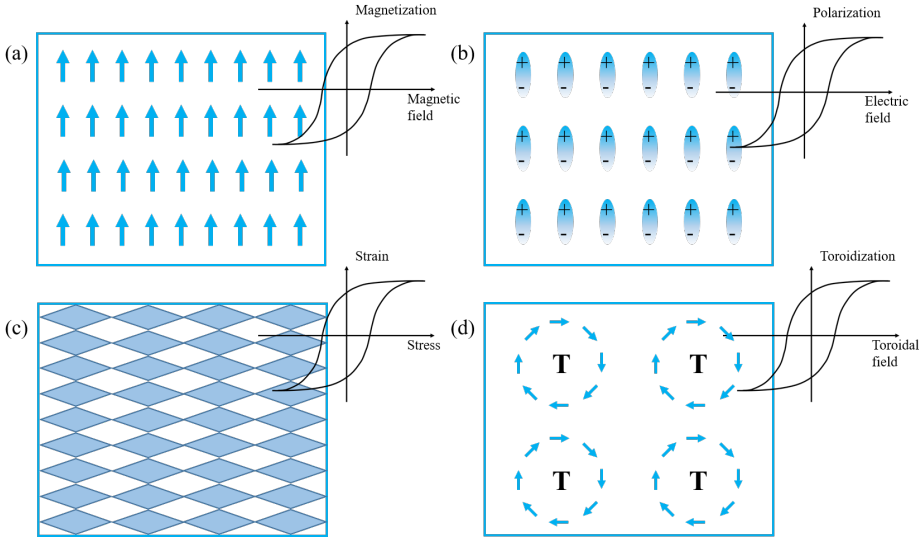

Figure 1.1: Four primary ferroic orders: (a) ferromagnetism, (b) ferroelectricity, (c) ferroelasticity, and (d) ferrotoroidicity.

ME multiferroics display several advantages in devices and applications. **Electric-field control of magnetism.** In the multiferroic devices, the required energy to switch the magnetic moment by the electric field is much less than that in the conventional manipulation of magnetic states by magnetic field [17, 20, 21]. **Radio- and high-frequency devices.** A variety of multiferroic heterostructures provide novel alternative materials in electric field-tunable radio-frequency/microwave signal processing, magnetic field sensor ME random access memory (MERAM), and voltage tunable magnetoresistance [22, 23]. **Ultralow power logic-memory devices.** By using the inverse Rashba–Edelstein (spin Hall) effect (IREE) to convert spin to charge (or voltage) and the multiferroic to perform the opposite conversion of charge to spin [21, 24], the magnetoelectric spin-orbit coupled (MESO) logic device can obtain an increase of voltage output from hundreds of μV to hundreds of mV, as well as a reduction in voltage requirement from the current ±5 V down to ±100 mV.

1.1.1 Category of Magnetoelectric Multiferroics

Although the term multiferroic appeared only about 30 years ago, the attempt to seek the materials with a strong coupling of magnetic and electric orders already started much earlier [25]. The first known antiferromagnetic ferroelectric compound was reported in perovskites by G. A. Smolenskii in the 2nd International Conference on Magnetism in Grenoble, France, in the 1950s [26]. Generally, perovskite materials have the chemical formula of ABO_3 in which O is oxygen, A and B are cations. Their crystal structure is shown in Figure 1.2: the A cations sit at the corners of the cube, the B atoms are in the center, and the oxygen cations form an octahedron around B. Smolenskii and his colleague Ioffe also

suggested that the introduction of magnetic ions into ferroelectric perovskites may create magnetic order in the compound. Based on this hypothesis, a wide search for multiferroic materials started. In the early 1960s, although a linear ME effect was first found experimentally in Cr_2O_3 [19, 27], most attention was given to boracites ($Mg_3B_7O_{13}Cl$) [18, 25]. Ascher et al. observed a strong induction of magnetization by an electric field and the converse effect in nickel iodine boracite $Ni_3B_7O_{13}I$ in 1966 [28]. A decade later, about 50 multiferroic systems were found [29]. However, none of these systems exhibited technologically feasible properties, causing the fading of interest for multiferroics in the following decades.

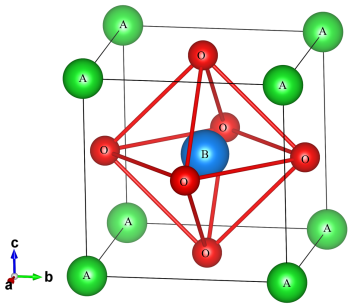

Figure 1.2: The structure of perovskite ABO_3.

The attention for multiferroics revived after the 2nd International Conference on Magnetoelectric Interaction Phenomena in Crystals (MEIPIC-2) in 1993 [30]. This conference identified and interrelated many of the phenomena, systems, and theories surrounding the ME effect. After that, many studies appeared in a short time. The two most studied compounds were $BiFeO_3$ and the hexagonal manganites $RMnO_3$ (R = Tb, Sc, Y, In, Dy-Lu). In 2003, Wang et al. reported that a large polarization exists with a weak ferromagnetic moment in epitaxial $BiFeO_3$ films [31]. In the same year, $TbMnO_3$ was found to display a ferroelectric polarization simultaneously with an incommensurate magnetic structure [32].

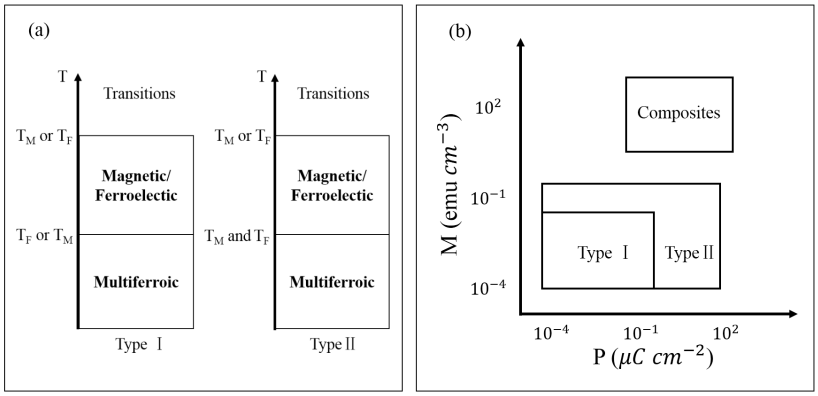

Figure 1.3: (a) Two types of single-phase multiferroics. T_M and T_F are the magnetic and ferroelectic transition temperatures, respectively. In the Type-I multiferroics, the ferroelectricity and magnetism emerge independently. In the Type-II multiferroics, the ferroelectric(magnetic) transition is accompanied by a magnetic(ferroelectric) transition and produces multiferroicity. (b) Schematic representation of the magnitudes of magnetization and polarization in Type-I and Type-II single-phase multiferroics, as well as composite multiferroics. A few multiferroics are outside the boundaries. The figure is intended to provide the relative differences among the multiferroic materials. (Adapted form [19])

Generally, bulk multiferroics are classified into two categories: Type-I and Type-II [15]. The two types are depicted in the figure 1.3(a). In the Type-I multiferroics, the coupling between the two orders is rather small since the magnetic and ferroelectric orders usually emerge from different origins and are stabilized independently. On the other hand, Type-II multiferroics usually display a strong coupling between the two ferroic orders since the ferroelectricity is induced by magnetically ordered states. Therefore, the magnitudes of magnetization and polarization in Type-I multiferroics are generally smaller than that in Type-II [Fig. 1.3(b)].

Except bulk multiferroics, composite multiferroic materials, which consist of distinct ferromagnetic and ferroelectric components, have been also investigated broadly [7, 33, 34]. In the early 1970s, most attempts focused on bulk composites like particulate composites[35, 36]. However, in the 21st century, a multilayer structure was expected to be better than bulk composites [37]. A recent discovery of this kind is the room temperature magnetoelectric multiferroic in $LuFe0_3/LuFe_2O_4$ layers which offers tremendous opportunity since the numerous possibility of available crystal structures and chemistries [38]. Besides, the composite multiferroic materials are generally superior to single-phase multiferroics in the magnitudes of magnetization and polarization [Fig. 1.3(b)].

1.1.2 Mechanism of Magnetoelectric Multiferroics

Along with the discovery of numerous multiferroics, the search for the origin of multiferroicity carries on. The microscopic origin of magnetism is basically the same in all magnetic insulators: partially filled d or f shells of transition-metal or rare-earth ions. On the other hand, there are two mechanisms for conventional ferroelectricity. Most of classical ferroelectric perovskites, like $BaTiO_3$, present a cubic structure at high temperature with a B cation at the center of the cell. However, when the temperature decreases, they undergo a phase transition from a high-symmetry paraelectric phase to a low-symmetry polarized phase accompanied by an off-center shift of the B cation. This displacement of B cation will generate a net polarization and thus the ferroelectricity. In addition, this kind of ferroelectricity is favoured by transition metals with empty d orbitals (d^0-ness) [39]. Such incompatibility between the d^n-ness and d^0-ness of magnetism and ferroelectricity significantly restricted the variety of multiferroic materials [40]. Another mechanism for ferroelectricity is the lone-pair stereochemical activity like on the Pb^{2+} ion in $PbTiO_3$. This will be discussed in detail in the next section. Multiferroicity can arise from the combined interplay of these magnetic and ferroelectric mechanisms [17]. Figure 1.4 shows the multiferroic family tree which outlines how the four ′root′ mechanisms of magnetism and ferroelectricity are responsible for different types of multiferroic materials.

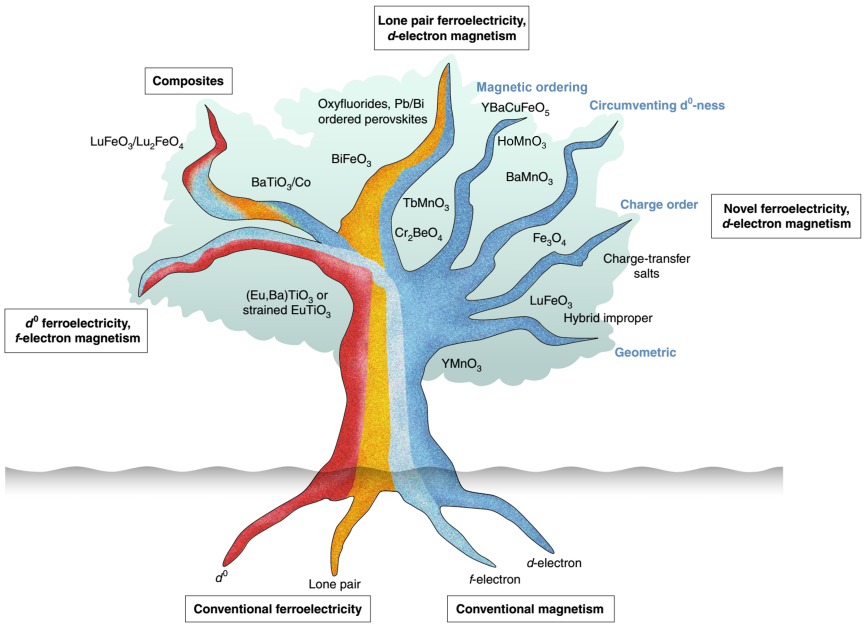

Figure 1.4: The multiferroic family tree [17]. The combination of different 'root' mechanisms can give rise to different types of multiferroic materials.

Type-I Magnetoelectric Multiferroics

Lone-pair ferroelectricity, d-electron magnetism. With the lone-pair ferroelectricity, the d^n-ness and d^0-ness "exclusion rule" can be avoided. In the lone-pair multiferroics, such as $BiFeO_3$, $BiMnO_3$, and $Pb(Fe_{2/3}W_{1/3})O_3$ [41], the magnetism comes from the $3d$ electrons of the B cation while the spontaneous polarization is driven by the $6s^2$ electrons of the A cation. More specifically, two unbonded valence electrons (lone-pair) on the $6s$ orbital of A cation, like Bi^{3+} and Pb^{2+}, are not involved in sp hybridization and create a local dipole [Fig. 1.5(a)]. Since the ferroelectric and magnetic order of this case are associated with different ions, the coupling between them is negligible. The materials with lone-pair ferroelectricity, along with the d^0-nees type, are also known as proper ferroelectrics in which the structural instability towards the polar state is the main driving force of the transition [41].

Geometric ferroelectricity, d-electron magnetism. In geometrically driven ferroelectrics, an ionic shift due to the space-filling effect or geometric constraint can lead to the formation of a polar state. The best known of this kind are the hexagonal (h-) $RMnO_3$ (R=Sc,Y,In or Dy-Lu) [42–44] in which an electric dipole moment is induced by a nonlinear coupling to non-polar lattice distortions, for example, the tilts of manganese-oxygen bipyramids and the buckling of R-O planes [1.5(b)]. This hybrid improper ferroelectrics in which non-polar rotations can yield a net polarization enables new multiferroics in layered perovskites [45–47].

Charge ordering ferroelectricity, d-electron magnetism. The non-uniform distribution of valence electrons instead of a displacement of ions can also induce ferroelectricity in the material. As we can see in Figure 1.5(c), the Fe_2 and Fe_3 ions in $LuFe_2O_4$ may form a superlattice and thus give rise to a net polarization [48]. Although $LuFe_2O_4$ is a prime candidate for charge-order-driven multiferroicity, the occurrence of ferroelectricity in it is still questioned [49]. Recently, a polar charge-ordered state was observed below ~100 K in the first technologically relevant magnet, ferrimagnetic magnetite, Fe_3O_4 [50]. Besides, the coexistence of robust spin-induced electric polarization and magnetic moment is found in organic charge-transfer complexes, and metal-organic frameworks [51–53].

d^0 ferroelectricity, f-electron magnetism. For the three multiferroics above, the magnetism is induced by the d-electron of the transition metal. In this case, the origin of magnetism is the f-electrons which avoids the d^0 vs d^n contradiction. For example, in $(Eu_{0.5}Ba_{0.5})TiO_3$ [54] and strained $EuTiO_3$ film [55], the rare-earth element Eu gives rise to the magnetic order while Ti is responsible for the ferroelectric order. Since the origins of magnetism and ferroelectricity in this compounds are different, they can be classified as Type-I multiferroics.

Circumventing the d_0-ness requirement for ferroelectricity. The incompatibility between the d_0-ness requirement of ferroelectricity and the partially filled d states of magnetism can have some exceptions. For example, an epitaxial-strain-induced multiferroic phase in $SrMnO_3$ was predicted by first-principle calculation [56]. Besides, a ferroelectric ground state driven by the off-centering of magnetic Mn^{4+} ion is predicted in $BaMnO_3$[57] and then observed in $Sr_{1-x}Ba_xMnO_3$ [58] (differ from the geometric ferroelectricity which is due to the displacement of non-magnetic ions). For $Sr_{1-x}Ba_xMnO_3$ (x=0.45 and 0.5), a ferroelectric phase is established below ~400 K while a multiferroic phase emerges below ~200 K [58].

Type-II Magnetoelectric Multiferroics

The ferroelectricity in Type-II multiferroics is driven by the magnetic order. The magnetic order can break inversion symmetry and induce an electric polarization (**P**). There are three main routes for the creation of multiferroicity in this kind of materials [Fig. 1.5(d)].

Firstly, most of materials of Type-II multiferroics present a non-collinear (spiral) magnetic structure,

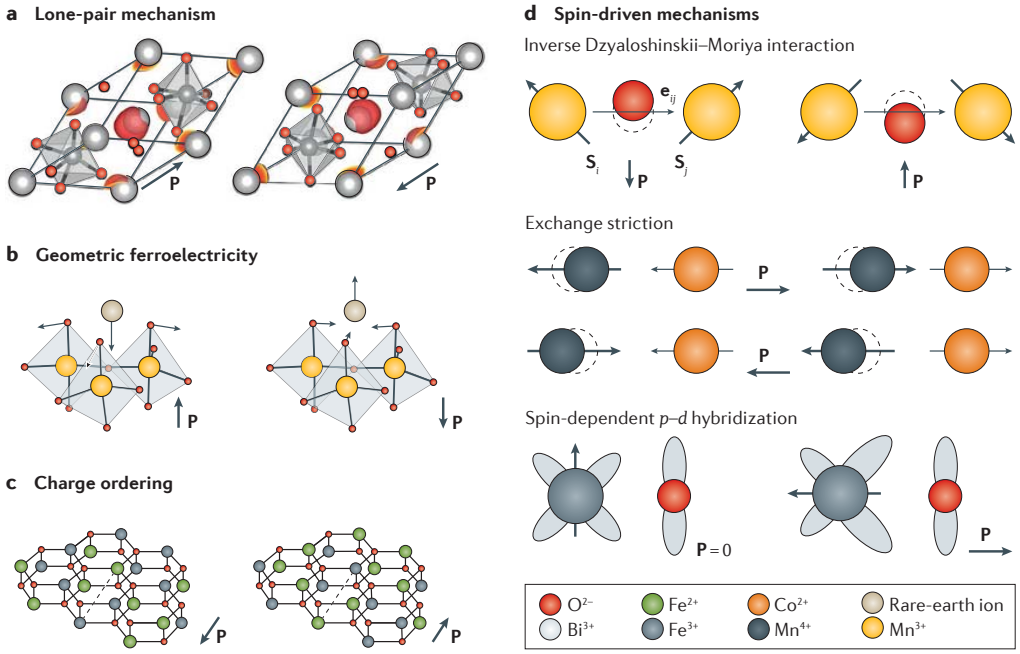

Figure 1.5: (a) Lone-pair ferroelectricity in $BiFeO_3$. The two s electrons of Bi^{3+} shift towards the FeO_6 octahedra. (b) Geometrically driven ferroelectricity in h-$RMnO_3$. The rare-earth ions are displaced by the tilt and deformation of MnO_5 bipyramids and lead to a spontaneous polarization. (c) Ferroelectricity due to the charge ordering in $LuFe_2O_4$. (d) Mechanisms for magnetic ordering ferroelectricity. [16]

such as layered $LaCu_2O_4$[41], Cr_2BeO_4[59] and orthorhombic (o-) $TbMnO_3$ [32]. In these compounds, $\mathbf{P}$ is produced by the inverse Dzyaloshinskii–Moriya (DM) interaction in which an acentric spin structure drives a non-centrosymmetric displacement of charges [60, 61]. As shown in the top of Figure 1.5(d), the polarization vector of (o-)$TbMnO_3$ is $\mathbf{P} \propto \mathbf{e}_{ij} \times (\mathbf{S}_i \times \mathbf{S}_j)$, where $\mathbf{e}_{ij}$ is the unit vector connecting neighbouring spins and $\mathbf{S}_{i,j}$ are the spins at neighbouring sites i and j.

Secondly, although relatively rare, the collinear magnetic structure can also induce polarization in the material. In this case, the polarization can be induced by the magnetism via exchange striction (ES) mechanism such as for Ca_3CoMnO_6 [62] and $TbMn_2O_5$ [63]. In contrast to the DM interaction, the exchange striction describes an acentric displacement of charges derived from the optimization of the symmetric spin scalar product $\mathbf{S_i} \cdot \mathbf{S_j}$, i.e., $\mathbf{P} \propto \mathbf{R}_{ij} \cdot (\mathbf{S}_i \cdot \mathbf{S}_j)$, where $\mathbf{R}_{ij}$ denotes the direction along which the magnetostriction occurs [see the middle of Figure 1.5(d)]. Therefore, the direction of $\mathbf{P}$ depends on the relative direction of neighbouring spins. According to reference [2], $BaFe_2Se_3$ is also in this case.

The last mechanism of this kind is the spin-dependent $p-d$ hybridization [see the bottom of Figure 1.5(d)]. A spontaneous polarization along the bond direction could be induced by the spin-orbit coupling of the hybridization between the $3d$ orbitals of the magnetic ion and the $2p$ orbitals of oxygen in $Cu(Fe,Al)O_2$ [64]. The polarization is expressed by the relation $\mathbf{P} \propto (\mathbf{S}_i \cdot \mathbf{e}_{ij})^2 \mathbf{e}_{ij}$.

Composite multiferroics

For the composites branches, the multiferroicity is produced by combining a non-magnetic ferroelectric with a non-ferroelectric magnet. The ME coupling in most of the composite systems depends on the elastic interactions among the ferroelectric and magnetic phases [65, 66]. In these composites, the ferroelectric and magnetic domains are coupled via electrostriction and magnetostriction. Besides, the ME coupling could be also mediated by the charge effect which is generally observed in layered heterostructures [67]. By applying an electric field, bound charges at the ferroelectric interface

accumulate, which modifies the charge density of the magnetic layer via charge screening [68].

1.1.3 Summary

In this section, we introduced some basic knowledge about multiferroicity. Three types of multiferroics and their mechanisms are discussed in detail. The spin-driven Type-II multiferroic materials is the most potential candidate because of its strong ME effect and abundant room-temperature systems [69–71]. This hope is also guaranteed by the driving mechanism itself, which leaves ample room for improvement towards higher ordering temperatures or polarization values by chemical doping, pressure effects, and strain. Therefore, the investigation of Type-II multiferroic materials with high transition temperature is a battle horse in condensed matter physics.

1.2 Superconductivity

Superconductivity is a physical phenomenon in which electrical resistance vanishes and magnetic field is expelled in the material. It is one of the most important discoveries in the 20th century and has been widely used in academic research and daily life. People can easily buy a small piece of $YBa_2Cu_3O_7$ alloy with the critical temperature (T_C) of superconductivity ~92 K and a bottle of liquid nitrogen on the Internet and then observe the superconducting levitation themselves at home [Fig. 1.6]. Besides, the high-temperature superconducting magnets are indispensable for magnetic resonance imaging (MRI) and particle accelerators. In this section, I will first introduce a short history of superconductivity. Then, the general knowledge of cuprate superconductors is presented. At the end, I will focus on the new high-temperature superconducting material: iron-based superconductors.

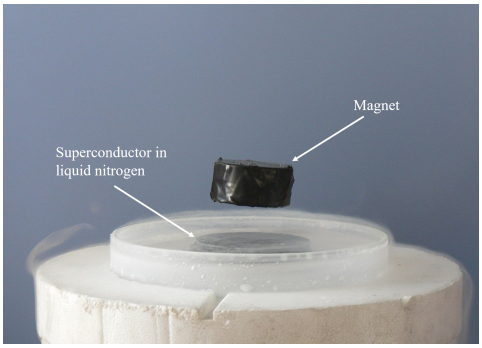

Figure 1.6: A magnet levitated above a high-temperature superconductor, cooled with liquid nitrogen.

1.2.1 A Brief History of Superconductivity

In the first decade of the 20th century, there were three theories about how metal resistance will behave as temperature falls to absolute zero [Fig. 1.7(a)]. First, Matthiessen claimed that the resistance would remain at a certain value at low temperature depending on the amount of impurities in the metal. Several years later, Lord Kelvin insisted that the electrons would start to freeze and thus cause the resistance to rise. A third possibility proposed by Dewar was that the resistance would drop inexorably to zero as temperature falls.

At that time, the Dutch physicist Kamerlingh Onnes was working at Leiden University in the Netherlands, one of the best low-temperature laboratories in the world. Following the ideas of Johannes Diderik van der Waals on the governing equation determining the properties of a gas, Onnes was striving to establish a governing equation for electrons. On 8 April 1911, Onnes started to measure the resistance of mercury for the first time [72]. The mercury was chosen because, as a liquid metal,

mercury can be repeatedly distilled to make it as pure as possible when other solid metals inevitably contain impurity which may disturb an electric current and confuse experimental results. His team succeeded in cooling down the mercury below 4.2 K (the boiling point of liquid helium) by reducing the vapor pressure of the helium. And then a completely unexpected phenomenon occurred: the resistance vanished abruptly [Fig. 1.7(b)]. This can not be explained by the three models. Later, this phenomenon was named by Onnes as *supragleider*. When translated from Dutch into English, it became *supraconductivity* and rapidly mutated into *superconductivity*.

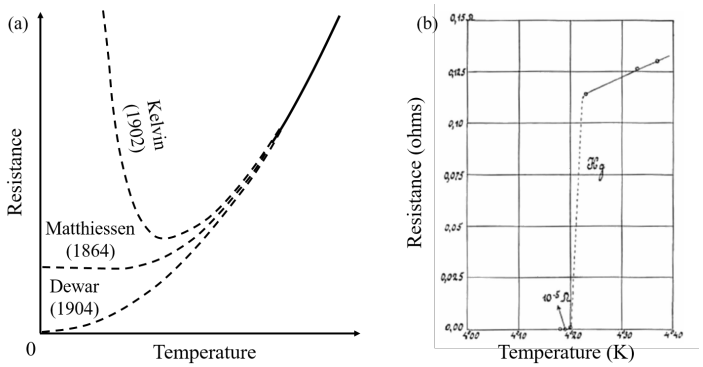

Figure 1.7: (a) The low-temperature resistance of metal according to three popular theories at the turn of the 20th century (reproduced from Ref. [73]). (b) The temperature dependence of the resistance of mercury from Onnes' experiment at 26th October 1911 shows the superconducting transition around 4.20 K [72].

Soon after the discovery of Onnes, in 1912, superconductivity was found in tin and lead with T_Cs of 3.7 K and 7.2 K, respectively. From then on, more and more elements were proven to be superconducting below a certain temperature. Until now, over fifty elements have been found to display superconductivity [Fig. 1.8].

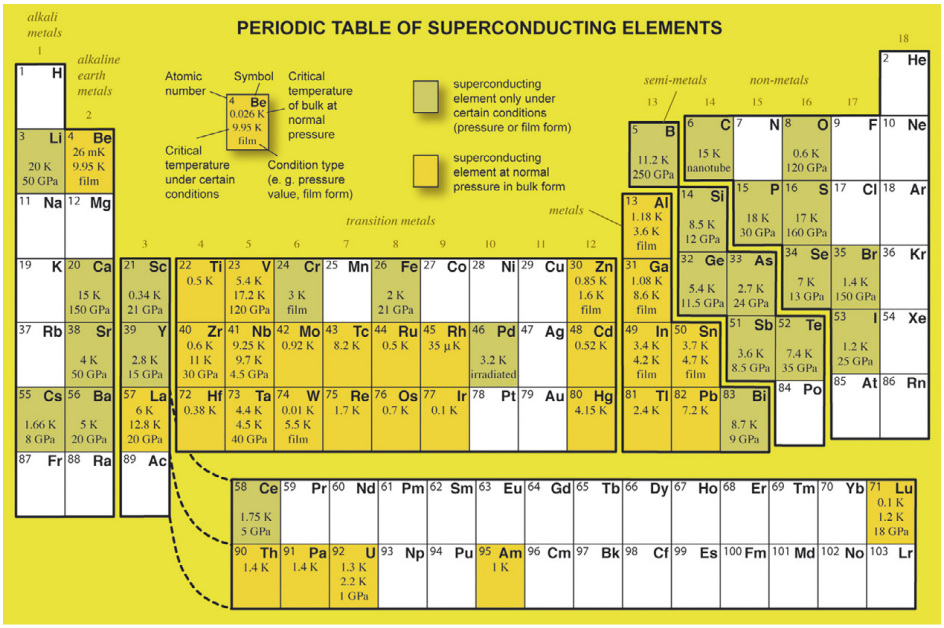

Figure 1.8: The periodic table of superconducting elements [74].

Despite the progress people already made, back to the 1910s, superconductivity remained completely without a satisfactory explanation. In the next two decades, the brightest minds in theoretical physics tried and failed to develop a microscopic understanding of the effect. In 1922, Albert Einstein, when he stated during the 40th anniversary of Kamerlingh Onnes's professorship in Leiden, concluded that "with our far-reaching ignorance of the quantum mechanics of composite systems we are very far from being able to compose a theory out of these vague ideas" [75].

The experimental breakthrough was made by Walter Meissner and Robert Ochsenfeld [76], followed by the pioneering theory of Heinz and Fritz London [77]. In 1933, Meissner and Ochsenfeld observed that the magnetic field is expelled from the superconductor when they were measuring the magnetic field distribution outside superconducting tin and lead samples [76]. This phenomenon was named as Meissner effect and became one of the fundamental properties of superconductivity. This strong expulsion of magnetic fields from a superconductor is responsible for the levitation of magnet in figure 1.6. The phenomenological theory of Meissner effect was proposed by the London brothers two years after [77]. The London brothers were trying to figure out how to make something like Ohm's law work for superconductors. Ohm's law itself would not help since superconductors allow a current to flow without a voltage. From the Meissner effect, they deduced that instead of being independent of each other like in a regular conductor, the electrons in a superconducting wire act together as if they were a single entity [78]. Therefore, the London brothers proposed an equation which connects the current in a superconductor with the magnetic field instead of an applied voltage:

$$\nabla \times \mathbf{j}_s = -\frac{n_s e^2}{m}\mathbf{B}, \tag{1.1}$$

where $\mathbf{j}_s$ is the superconducting current density, $\mathbf{B}$ is the magnetic field within the superconductor, e is the charge of an electron or proton, m is electron mass, and n_s is a phenomenological constant loosely associated to the number density of superconducting carriers (superfluid density). The London equation is the simplest meaningful description of superconductivity. Another significant contribution London brothers made in superconductivity is that they deduced that the magnetic flux penetrating a superconducting loop should be quantized to certain fixed values [79]. This prediction inspired John Bardeen to solve the microscopic explanation for superconductivity several years later.

Another critical discovery that indicates the origin of superconductivity is the isotope effect. In 1950, Herbert Fröhlich was trying to include the effect of the vibration of the crystal lattice in the explanation of superconductivity [80, 81]. It is well known that the frequency of the lattice vibration is inversely proportional to the square root of the mass of the atoms. Therefore, he proposed that if the vibration of atoms are involved in superconductivity, the transition temperature of superconductivity would depend on the mass of the atoms. Soon this prediction was proved by Emanuel Maxwell at the National Bureau of standards and also by Bernard Serin et al. at Rutgers University [82, 83]. By carefully determining the transition temperature of different mercury isotopes, they found that the transition temperature is related to its atomic atoms via the relation $T_C \sim M^{-1/2}$ [84]. This is a strong evidence that atomic vibrations are closely tied to superconductivity.

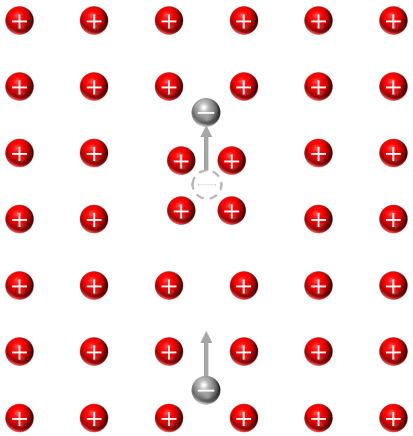

Figure 1.9: A Cooper pair in the lattice of positively charged ions. The first electron attracts nearby ions. But when it leaves, the cations take a longer time to respond. There is still an excess positive charge to help the second electron of the Cooper pair travel through.

Based on the ideas of London equation and isotope effect, in 1957, John Bardeen, Leon Cooper, and John Robert Schrieffer proposed a microscopic theory for superconductivity (BCS theory) [85]. According to the BCS theory, the electrons near the Fermi surface of superconductors, instead of being

independent, form Cooper pairs. The Cooper pairs were discovered by Leon Cooper in 1956. He proposed that two electrons can be bound by an arbitrarily small attraction [86]. In superconductors, this attraction is generally attributed to an electron-lattice interaction, i.e., electron-phonon interaction. Figure 1.9 shows a Cooper pair moving in the lattice of cations. The electron can distort the ions around it by pulling them slightly towards itself. When the electron passes through, the heavier ions take longer to respond and get back to their initial position, giving rise to a little region of positive charge. This positively charged region will attract the second electron and result in the binding of two electrons. In the BCS framework, superconductivity is a macroscopic effect, resulting from the condensation of Cooper pairs. In the superconducting state, an enormous number of electrons acted in concert, as if each was part of a larger, inseparable whole. The materials which can be described by BCS theory are classified as conventional superconductors.

Before the 1980s, although the BCS theory is a successful explanation for superconductivity, it provides little hope to find superconductors working at a much higher temperature than 20 K. In this theory, the superconducting critical temperature (T_C) has the relation:

$$k_B T_C = 1.13\hbar\omega e^{-1/N_0 V_0}, \tag{1.2}$$

where ω and V_0 are the phenomenological parameters of the model Hamiltonian, N_0 is the density of electronic levels for a single spin population in the normal metal [87]. Since these parameters are not expected to vary greatly beyond what had already been found, it is hard to find superconductors with higher T_C. The record T_C of 23.2 K in Nb_3Ge had stood since 1973.

The breakthrough occurred from a completely unexpected direction: the perovskites. In 1986, the IBM researchers Georg Bednorz and Karl Alex Müller found that the $La_{2-x}Ba_xCuO_4$ system can exhibit superconductivity below 35 K [88]. Within one year, M.-K. Wu et al. expanded the record value of T_C to 93 K by replacing La with Y ($YBa_2Cu_3O_{7-\delta}$) [89]. Soon, the superconductivity was also confirmed in the ceramics La–M–Cu–O, where M = Ba, Sr, Ca [90]. These materials were named as cuprate superconductors.

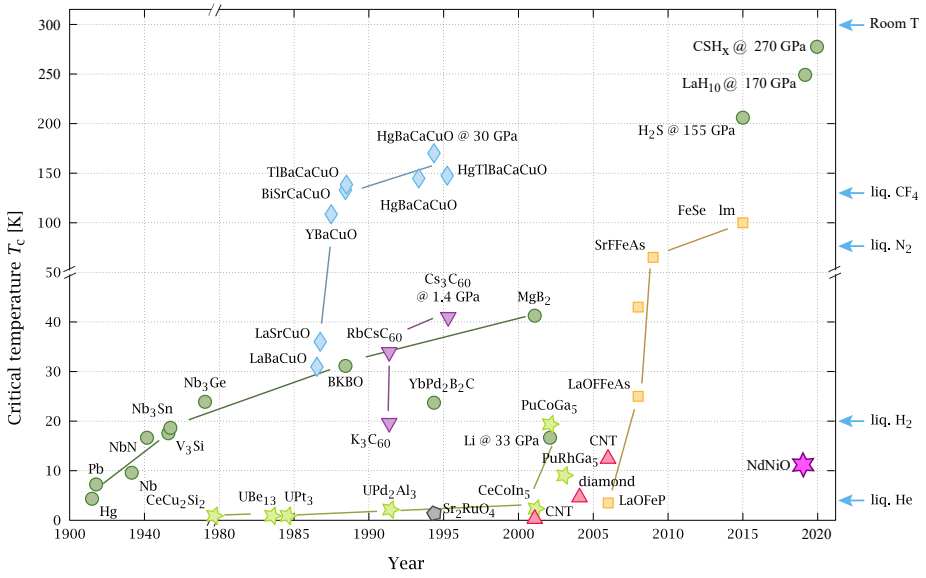

Figure 1.10: History of some discovered superconducting compounds [91]. Note in particular the BCS superconductors (green circles), the cuprates (blue diamonds), and the iron-based superconductors (yellow squares).

In the 21st century, the discovery of superconductors has been expanded to organic [92], heavy

fermion [93], and iron-based compounds [94] as shown in Figure 1.10. The conventional superconductors are marked by green circles. Others are unconventional superconductors that can not be explained by the BCS theory. Despite the numerous amount of discovered unconventional superconductors, a proper interpretation of their superconductivity is still missing. It seems that the mediation of superconductivity is still Cooper pairs, but the "glue" that keeps them together is different from the phonons used in the BCS theory [95]. The cuprate and iron-based superconductors are called real high-temperature superconductors (HTSCs) since only they display the T_C higher than the liquid-nitrogen boiling temperature (77 K) at ambient pressure. Besides, a T_C value of 203 K has been found in highly pressurized sulphur hydride H_2S [96].

1.2.2 Cuprate Superconductors

The superconductivity in cuprates can be achieved by applying pressure [97] or doping [88]. Since replacing atoms with smaller atoms will cause the unit cell to shrink and applying pressure will compress the unit cell, it is not surprised they display similar effect in the compound. Until now, dozens of cuprate superconductors have been discovered [98]. They all exhibit a layered crystal structure with a stacking sequence of CuO_2 planes and charge-reservoir blocks. Figure 1.11 shows the unit cells of some typical cuprates. In these structures, the Cu and O atoms form layers separated by the neighboring layers, e.g., lanthanum, yttrium, strontium, or barium, which help to stabilize the structure. Since these metallic cations can provide charge carriers by introducing extra electrons or holes into the CuO_2 layers, they are also called the charge-reservoir. It is generally believed that the high value of T_C and the anomalous state of cuprate materials are determined by the unique electronic and magnetic structure of the CuO_2 plane [98].

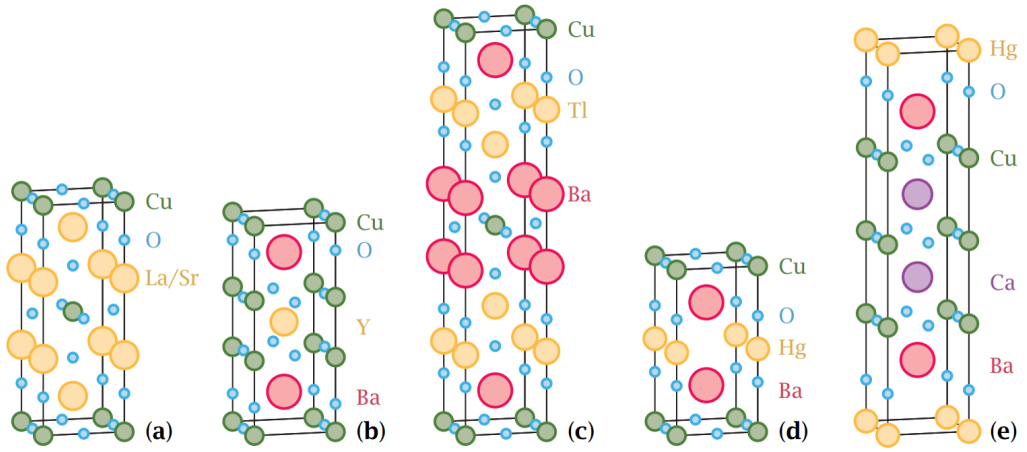

Figure 1.11: The crystal structures of (a) $La_{2-x}Sr_xCuO_4$, (b) $YBa_2Cu_3O_6$, (c) $Tl_2Ba_2CuO_6$, (d) $HgBa_2CuO_4$, (e) $HgBa_2Ca_2Cu_3O_8$ [91].

Generally, the parent compounds of cuprates are Mott-Hubbard insulators with an AFM long-range order. Upon doping, the AFM phase is suppressed, and the SC phase is stabilized at low temperature. Figure 1.12 shows the generic phase diagram of the cuprate superconductors in the temperature (T) and hole concentration (p) per CuO_2 coordinates. Generally, the T_Cs of cuprates has a parabolic dependence on the concentration of charge carriers p with a maximum at an optimal doping p_{opt}. Presland et al. proposed a universal formula for $T_C(p)$ [99]:

$$T_C(p) = T_{C,max}[1 - \beta(p - p_{opt})^2], \tag{1.3}$$

where the parameters β and p_{opt} are constants. In the under-doped region ($p < p_{opt}$), the cuprates exhibit anomalous physical properties when a pseudogap in the electronic spectrum is opened below a characteristic temperature T^*. In the over-doped region ($p > p_{opt}$), metallic properties are recovered.

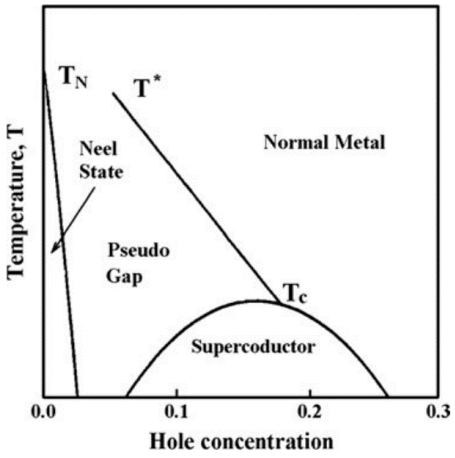

Figure 1.12: Generic phase diagram of the cuprate superconductors. [98]

Superconductivity requires a pairing mechanism that can overcome the Coulomb repulsion of electrons. In conventional superconductors, the phonons play an essential role in the pairing of electrons. However, the isotope effect in cuprates is rather weak, indicating that the electron-phonon pairing is less important [100]. As discussed above, the superconducting phase in cuprates emerges by suppressing the AFM phase of the parent compounds. It is thus natural to suppose that the AFM excitation is related to the superconductivity in the cuprates. The magnetic pairing mechanism was first proposed for the superconductors with heavy fermions where the d-wave pairing was suggested [101, 102], and soon expanded to the cuprates [103]. It was shown that an attraction appears in the d-channel and acts effectively near the AFM instability due to the exchange of AFM paramagnons [104, 105]. As for cuprates, the pairing mechanism is under debate over decades. Multiple models have been presented, like spin-charge separation [106], stripe formation [107], and Fermi surface nesting [108].

1.2.3 Iron-based Superconductors

In 20th century, a number of superconducting compounds containing iron have been discovered: U_6Fe (T_C = 3.9 K, 1958) [109], Th_7Fe_3 (T_C = 1.8 K, 1961) [110], $Lu_2Fe_3Si_5$ (T_C = 6.1 K, 1980) [111], β''-(bedt-ttf)$_4$ [$(H_2O)Fe(C_2O_4)_3$]·PhCN (T_C = 8.5 K, 1995) [112]. However, they did not attract a lot of attention from researchers since their critical temperature is quite low. The breakthrough happened when Hideo Hosono and his coworkers observed superconductivity in the iron pnictide LaFePO with $T_C \sim 5$ K [113] in 2006. Just two years later, they increased the superconducting transition temperature to 26 K in $LaFeAsO_{1-x}F_x$ with x=0.11 [114]. This demonstrated a promising new way to obtain high-temperature superconductors apart from the cuprates, since then, the iron-based superconductors (FeSCs) with higher T_C were discovered continually, as indicated by the yellow squares in Figure 1.10.

So far, six different structural classes of FeSCs have been found [94, 115]: the original LaFeAsO ("1111") family (T_C = 26 K) [114], the K doped $BaFe_2As_2$ ("122") family (T_C = 38 K) [116], the LiFeAs ("111") family (T_C = 18 K) [117], the FeSe ("11") family (T_C = 8 K) [118], the $Sr_2ScFePO_3$ ("21113") family (T_C = 17 K) [119, 120], the defect structure $K_{0.8}Fe_{1.6}Se_2$ ("122*" or "245") family (T_C = 32 K) [121]. These structures, shown in Figure 1.13, all share a common two-dimensional (2D) lattice structure in which the iron atoms are surrounded by tetrahedrally coordinated pnictogen or chalcogen anions. Besides, the iron layers are separated by alkali, alkaline-earth or rare-earth and oxygen 'blocking layers'. This Fe pnictide/chalcogenide layer of FeSCs, resembling the CuO layer in cuprates, is now widely thought to play an essential role in raising the high-T_C superconductivity in the FeSCs.

The phase diagram of FeSCs is similar to that of cuprates. The superconducting phase of FeSCs is derived from an antiferromagnetic (AFM), non-superconducting parent phase by chemical doping or

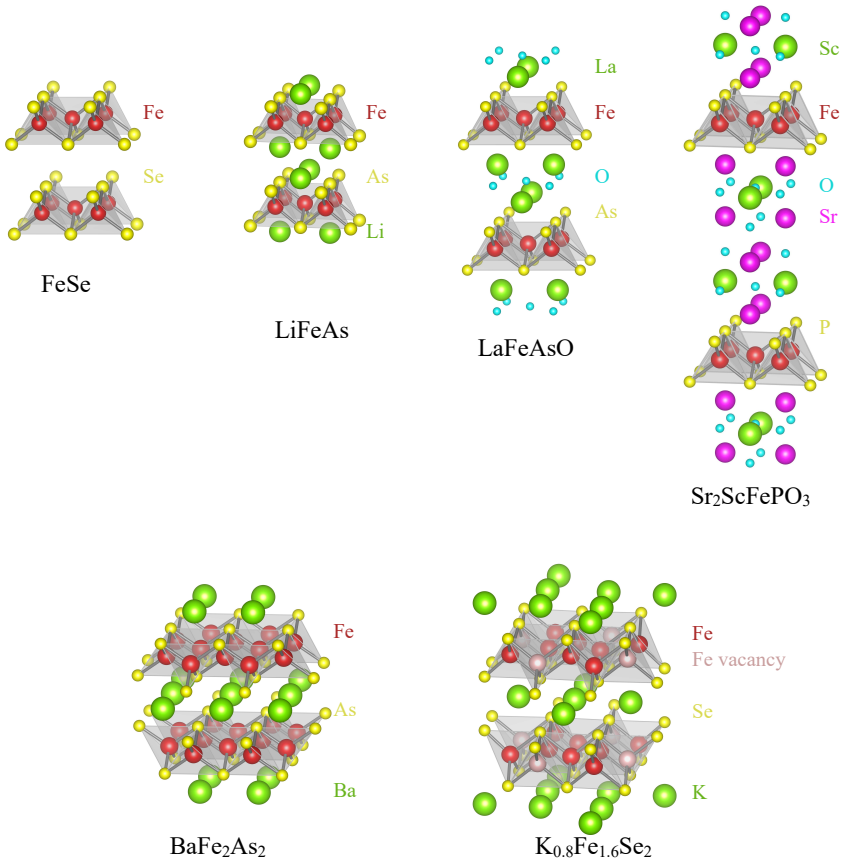

Figure 1.13: The crystal structures of the six classes of FeSCs. Note that the Fe layers in $K_{0.8}Fe_{1.6}Se_2$ are the same as in $BaFe_2As_2$ but with Fe vacancies.

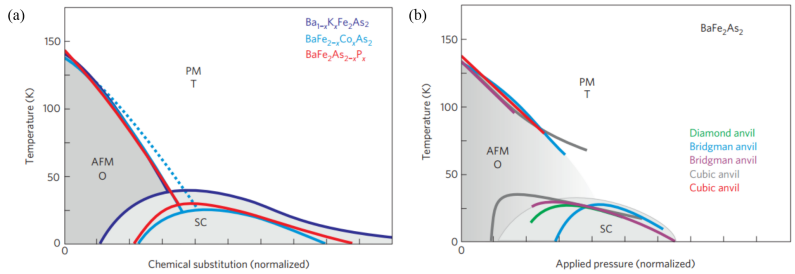

Figure 1.14: Experimental phase diagrams of the $BaFe_2As_2$ family [115].

applying external pressure. An example of experimental phase diagrams is presented in Figure 1.14. The Ba-based 122 family is the most studied and captures the main characters of all FeSCs. In $BaFe_2As_2$, the AFM state is suppressed by the substitution of either the alkaline-earth (Ba), transition-metal (Fe), or pnictogen (As) with different elements [Fig. 1.14(a)], as well as the applying of pressure [Fig. 1.14(b)], and followed by a superconducting state. On the other hand, FeSCs also exhibit many unique characteristics compared to the cuprates. The parent compounds of FeSCs (except 245 family) are metals, in distinction to cuprate superconductors for which the parent compounds are Mott insulators. Besides, the cuprates are much more anisotropic and display d-wave gap symmetry versus primarily s-wave symmetry for FeSCs. One can also see from the comparison between Figure 1.12 and Figure 1.14, the decreasing of T_C upon doping in cuprates is rapider than that in FeSCs.

Soon after the discovery of superconductivity in the iron pnictides, the antiferromagnetic spins

fluctuations are proposed to mediate the superconductivity in undoped $LaFeAsO_{1-x}F_x$ [122]. The proximity of the SC phase to an AFM state suggested that the magnetic fluctuation could be intimately related to the superconductivity in the FeSCs. Besides, this new pairing mechanism on its own or in combination with phonon-mediated pairing may boost the superconducting transition temperature much higher. However, the real pairing mechanism of FeSCs remains controversial [123].

1.2.4 Summary

An introduction of conventional superconductors and the new high-temperature superconductors is given in this section. Both CuSCs and FeSCs exhibit much higher T_Cs than the conventional superconductors, which cannot be interpreted by the conventional BCS theory. Therefore, a new pairing mechanism is required. The most prominent analogy between the CuSCs and FeSCs is the proximity of an AFM phase to the SC phase. Thus, the magnetic fluctuations are speculated to participate in the electric pairing in the superconducting phase. This makes the magnetic structure of HTSCs an important ingredient in understanding the superconductivity and developing a microscopic pairing model.

2

Quasi-one-dimensional ladder compound $BaFe_2Se_3$

Contents

This chapter will introduce the state of the art of quasi-1D spin ladder antiferromagnet $BaFe_2Se_3$. Recently, superconductivity and multiferroicity have been observed in $BaFe_2Se_3$ which attracts a lot of interest [1, 2]. A short introduction of $BaFe_2Se_3$ is given in Section 2.1. Section 2.2 presents the evolution of the crystal structure of $BaFe_2Se_3$ with the variation of temperature and pressure. In Section 2.3, the electrical and magnetic properties of $BaFe_2Se_3$ are introduced. Then, the magnetic structure of $BaFe_2Se_3$ is discussed in Section 2.3.2. In the last section, the influence of the chemical substitution in $BaFe_2Se_3$ is given in details.

2.1 Introduction

$BaFe_2X_3$ (X=Se or S) single crystals were first synthesized and studied by Hong et al. in 1972 [3]. Orthorhombic *Pnma* (No. 62) and *Cmcm* (No. 63) structures were identified for X=Se and S, respectively. However, during the next decades, these compounds were neglected by researchers. The situation changed after the discovery of superconductivity in $LaFeAsO_{1-x}F_x$ [114] in 2008. As we can see in Figure 2.1, the number of publications about $BaFe_2X_3$ increased exponentially after the discovery of $LaFeAsO_{1-x}F_x$. $BaFe_2X_3$ are composed of infinite double chains of FeX_4 tetrahedra resembling the FePn/Ch (Pn: pnictide, Ch: chalcogenide) layers in the FeSCs. Therefore, they are considered as potential candidates of FeSCs. In 2011, Krzton-Maziopa and his coworkers studied the crystal and magnetic structures of $BaFe_2Se_3$ and observed possible superconductivity [5]. Although the superconductivity in $BaFe_2Se_3$ at ambient pressure seems to arise from the impurities after further researches, it successfully raised the attention of researchers on this iron chalcogenide compound. Finally, after several years, the superconducting phases in $BaFe_2X_3$ were observed under pressure (10−15 GPa for Se, 10−17 GPa for S) [1, 9]. This makes $BaFe_2X_3$ a new '123' iron-based superconductor. Moreover, a possible magnetic multiferroic state was predicted in $BaFe_2Se_3$ by first-principles study [2]. The coexistence of superconductivity and multiferroicity in $BaFe_2Se_3$ makes it more intriguing for further research. This is why we focus on the study of $BaFe_2Se_3$ in the present thesis.

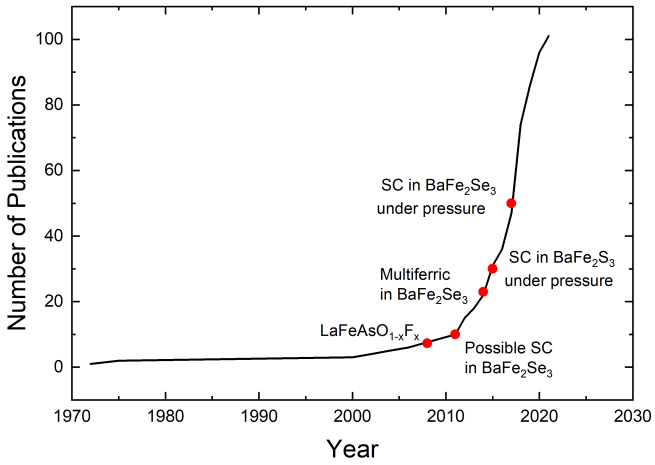

Figure 2.1: Integrated number of publications about $BaFe_2X_3$ (X= Se, S) from 1972 to 2021. The red points indicate the years of these important discoveries for $BaFe_2Se_3$. (Data from the web of science, key words: $BaFe_2Se_3$ or $BaFe_2S_3$)

2.2 Crystallographic Structure

$BaFe_2X_3$ presents a quasi-one-dimensional structure, resembling the copper oxide laddered system $Sr_{14-x}Ca_xCu_{24}O_{41}$ [124, 125]. The crystallographic structures of $BaFe_2Se_3$ and $BaFe_2S_3$ are shown in figure 2.2. Each unit cell consists of double chains of edge-sharing FeX_4 tetrahedra separated by Ba atoms. At ambient condition, $BaFe_2Se_3$ and $BaFe_2S_3$ crystallize in *Pnma* and *Cmcm* space groups, respectively. One should notice that the ladder, leg, and rung directions are a, b, and c axes in *Pnma* but b, c and, a axes in *Cmcm*. Compare to $BaFe_2S_3$, in $BaFe_2Se_3$, the iron ladders are slightly tilted between each other [Fig. 2.2(b) and (e)]. Besides, the Fe-Fe bonds along the chains of $BaFe_2S_3$ are identical while they alternate in $BaFe_2Se_3$ [Fig. 2.2(c) and (f)].

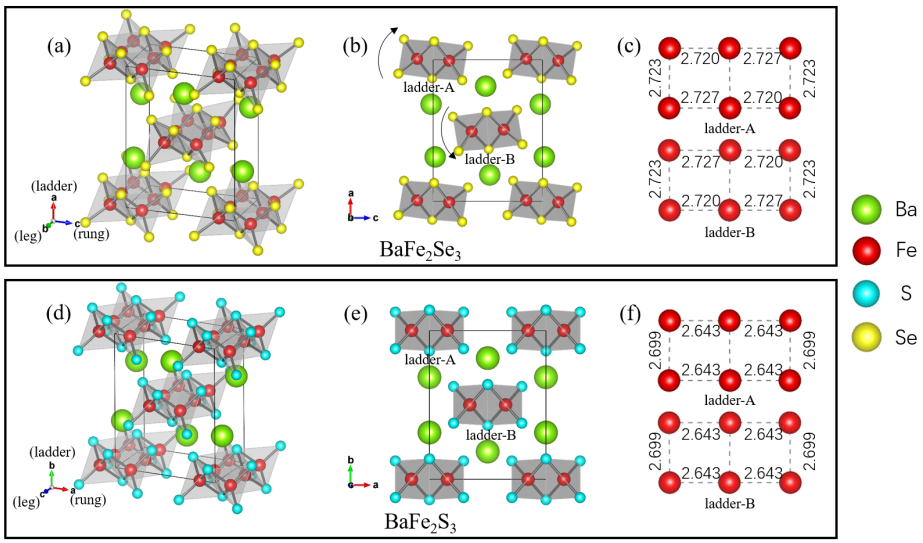

Figure 2.2: Crystallographic structures of $BaFe_2Se_3$ and $BaFe_2S_3$ at ambient condition [3]. (a), (b) and (c) for $BaFe_2Se_3$ in *Pnma* space group. (d), (e) and (f) for $BaFe_2S_3$ in *Cmcm* space group. The lattice parameters of $BaFe_2Se_3$ are a = 11.878(3) Å, b = 5.447(2) Å, and c = 9.160(2) Å. The lattice parameters of $BaFe_2S_3$ are a = 8.7835 Å, b = 11.219 Å, and c = 5.2860 Å. The tilts of the ladders in *Pnma* are shown by the black arrows in (b). (c) and (f) are the projections of the two iron ladders (Ladder-A and Ladder-B) along the ladder direction for $BaFe_2Se_3$ and $BaFe_2S_3$, respectively. The lengths of Fe-Fe bonds are given in Å.

2.2.1 Temperature Dependence

The crystal structure of $BaFe_2Se_3$ has been widely studied by X-ray[3, 126–128], synchrotron [5, 129], and neutron[4] diffractions. The *Pnma* space group was determined at low temperature in pure $BaFe_2Se_3$ [3] and in Fe deficient compound [126]. A first-order isostructural transition from α-*Pnma* to β-*Pnma* and a second-order phase transformation from β-*Pnma* to γ-*Cmcm* were observed around 425 K and 660 K, respectively [129]. As we can see in Figure 2.3 (a), with temperature increasing, the $FeSe_4$ tetrahedra rotate within the ac plane and the Ba atoms shift mainly along the c-axis with a small component along a-axis and reach a *Cmcm* symmetry above 660 K [129]. Besides, an optical second harmonic generation (SHG) study evidence the existence of electric polarization in $BaFe_2Se_3$ below 400 K [130]. Since the centrosymmetric *Pnma* space group should not induce polarization, they proposed that the polar $Pmn2_1$ space group (No.31) may stabilize below 400 K. In $Pmn2_1$, the inversion centers in the ladder are broken, driving by block-type lattice distortions [Fig. 2.3(c)]. However, SHG is not a proper method to determine the crystal structure which makes the correct structure of $BaFe_2Se_3$ at low temperature still unrevealed. This problem will be further discussed in Chapter 4.

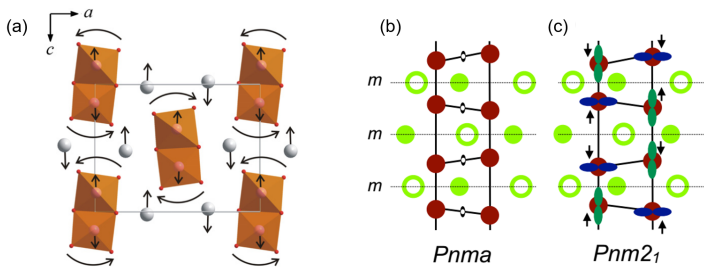

Figure 2.3: (a) Evolution of crystal structure of $BaFe_2Se_3$ with temperature increasing [129]. (b) and (c) Schematic illustrations of the local ladder structure in *Pnma* (b) and $Pmn2_1$ (c), respectively [130]. The circles in the ladder of (b) show the inversion centers, the black arrows in (c) indicate the block-type lattice distortions, and the mirror planes (m) are also shown.

2.2.2 Pressure Dependence

The crystallographic structure of $BaFe_2Se_3$ under pressure was studied by powder and single-crystal synchrotron diffraction at room temperature [129, 131]. A second order transition from α-*Pnma* to γ-*Cmcm* around 4 GPa and a first order transformation from γ-*Cmcm* to δ-*Cmcm* around 16 GPa were determined. As shown in Figure 2.4, the a-axis in the δ-*Cmcm* phase is larger than the b-axis while it is the opposite in the γ-*Cmcm* phase. Within the pressure and temperature (P-T) phase diagram, the total number of known $BaFe_2Se_3$ polymorphs is four: α (*Pnma*), β (high-temperature *Pnma*), γ (*Cmcm*), and δ (high-pressure *Cmcm*) [Fig. 2.5]. On the other hand, a first-principle study proposed a vanishing of the tilting angle of the iron ladder in $BaFe_2Se_3$ at around 6GPa, implying a structural transition from *Pnma* to *Cmcm* [8]. The difference between the experiment and calculation is acceptable considering the error caused by the pressure transmitting medium (PTM).

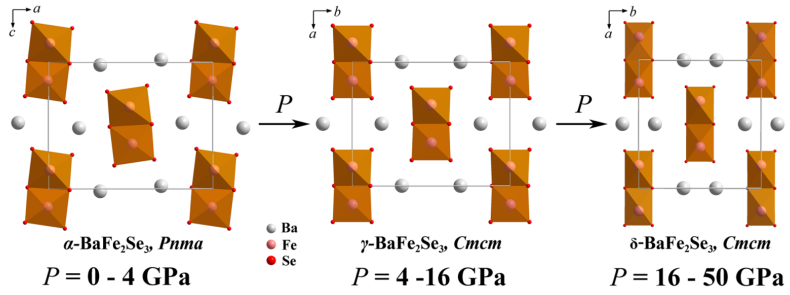

Figure 2.4: The series of $\alpha - \gamma - \delta$ phase transitions in $BaFe_2Se_3$ at room temperature [131]. b is larger than a in the γ-*Cmcm* while a is larger than b in the δ-*Cmcm*.

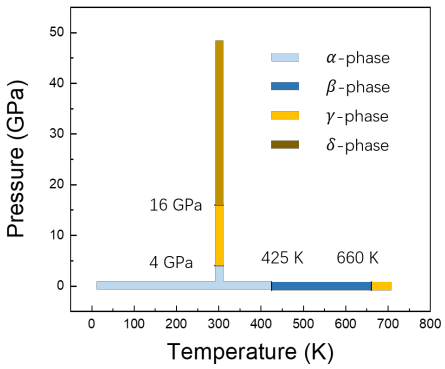

Figure 2.5: The Pressure-Temperature phase diagram of $BaFe_2Se_3$. Four phases are determined.

2.3 Magnetic Properties and Magnetic structure

2.3.1 Magnetic Properties

.

Normally, magnetic susceptibility measurement is a powerful way to determine the magnetic transition temperature and magnetic order in a compound. Figure 2.6 shows the temperature dependence of susceptibility $\chi(T)$ for paramagnetic (a), ferromagnetic (b) and antiferromagnetic (c) materials. $\chi(T)$ of a paramagnet obeys the Curie law

$$\chi = \frac{C}{T}, \tag{2.1}$$

where C is the Curie constant [Fig. 2.6(a)]. In the ferromagnet or antiferromagnet, the critical temperature above which magnetic ordering vanishes is known as the Curie temperature T_C and the Néel temperature T_N, respectively. Above T_C, $\chi(T)$ can be fitted by the Curie-Weiss law [Fig. 2.6(b)], while the curve above T_N obeys another modification of Curie law [Fig. 2.6(c)]. The susceptibility of a ferromagnet has a singularity at $T = T_C$ while an antiferromagnet exhibits a maximum value at T_N.

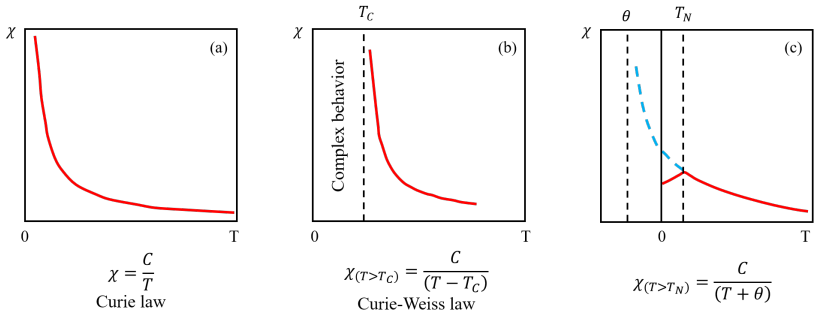

Figure 2.6: Temperature dependence of the magnetic susceptibility for paramagnetic (a), ferromagnetic (b) and antiferromagnetic (c) materials. Adapted from reference [132].

The definition of the transition temperature from the magnetic susceptibility measurements is more difficult. Although the PND experiment shows a clear antiferromagnetic order below the Néel transition ~ 250 K [4, 5, 133], the susceptibility sometimes shows no anomaly at T_N [4, 133]. Besides, $\chi(T)$ cannot be fitted using a standard Curie-Weiss law up to 390 K, which makes T_N impossible to determine [133, 134]. Even a weak ferromagnetic behavior below T_N is reported in previous work [4]. Moreover, a hysteresis behavior between the $\chi(T)$ curves after field-cooling (FC) and zero-field-cooling (ZFC) was observed when the applied field is along a, b and c directions [Fig. 2.7 (a) and (b)] [127, 134]. The weird behaviors of $\chi(T)$ are attributed to ferromagnetic impurities or short-range order in $BaFe_2Se_3$ [4, 127, 134]. A bifurcation between ZFC and FC curves persists below 50 K even after minimizing the effect from the ferromagnetic component [Fig. 2.7(c)] [133]. This may indicate a spin glass behavior caused by small randomness at low temperature in $BaFe_2Se_3$. However, all these unusual magnetic properties require further studies.

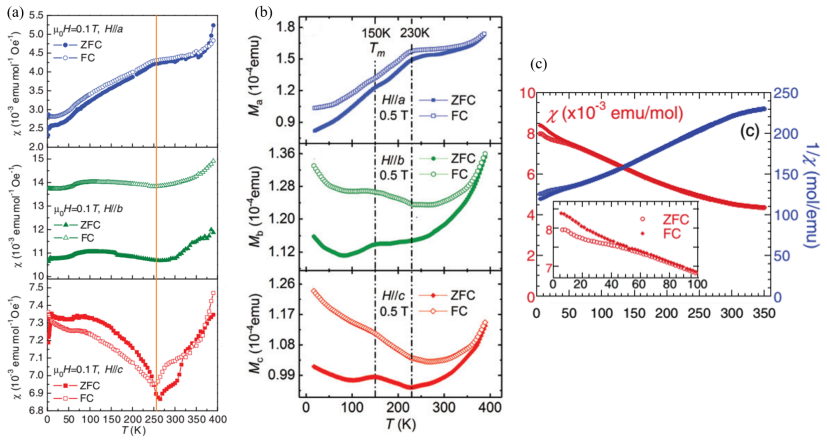

Figure 2.7: Temperature dependencies of dc magnetic susceptibility $\chi(T)$ for $BaFe_2Se_3$ under ZFC and FC modes from reference [134] (a), [127] (b). The applied field is along a (top), b (middle), and c (bottom). (c) $\chi(T)$ curves of $BaFe_2Se_3$ after ZFC and FC from reference [133]. The susceptibility are deduced under applied field of 5 T and subtract the one at 1 T to minimize effects from ferromagnetic impurity.

2.3.2 Magnetic Structure

Since the magnetism and superconductivity in FeSCs are closely related, the research of the magnetic structures of $BaFe_2Se_3$ becomes essential to study its superconductivity. In 2011, Krzton-Maziopa et al. observed a long-range antiferromagnetic order in $BaFe_2Se_3$ below 240 K by neutron powder diffraction [5]. Meanwhile, a short-range AFM order was identified above 240 K and persisted up to room temperature. At low temperature, a block-like AFM order with the propagation wave vector of $\mathbf{k} = (1/2, 1/2, 1/2)$ was determined by representation analysis [5]. The magnetic order is characterized by the AFM arrangement of ferromagnetically ordered 2×2 iron superblocks along the b-axis [Fig. 2.8]. The spins of Fe are parallel or antiparallel to the ladder direction. Besides, the block-AFM state is also proved to be the ground state of $BaFe_2Se_3$ by first-principles calculation [135]. Meanwhile, two block magnetic models in Figure 2.8 are proposed for $BaFe_2Se_3$ and can not be distinguished by the refinements of PND data [5]. However, these two models are actually the same model. Model (b) can be obtained by an origin shift of $(1/2, 1/2, 1/2)$ from model (a) [Fig. 2.8]. This block-like model is named as Block-A magnetic structure in this thesis.

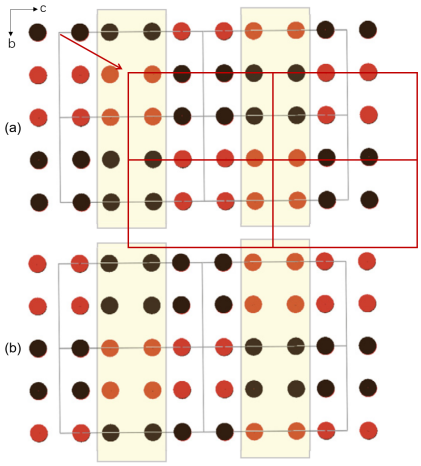

Figure 2.8: Projections of Fe on the bc-plane of the two possible magnetic structures for $BaFe_2Se_3$. The black and red circles correspond to the up and down spin directions. The two ladders are separated by different background colors. The red grid indicates the crystal lattices after an origin shift $(1/2, 1/2, 1/2)$ of (a). (Figure modified from [136]. Notice that ref. [136] is a correction of ref. [5]).

Not long after Krzton-Maziopa, Caron and his coworkers found another magnetic structure (Block-B) for $BaFe_2Se_3$ also by PND and representation analysis [4]. The new magnetic model is also observed by Nambu et al. [133]. The Block-B magnetic structure is shown in Figure 2.9(a) while its projection on the bc-plane is shown in Figure 2.9(b). The difference between Block-A and Block-B relies on the ferromagnetic 2×2 superblocks between ladder-A and ladder-B. They are antiferromagnetically ordered in the Block-A model while there is a phase shift of one Fe-Fe distance between them in the Block-B model. However, the PND method cannot distinguish the slight difference between Block-A and Block-B models. Therefore, single-crystal neutron diffraction measurement is required to reveal the real magnetic structure of $BaFe_2Se_3$.

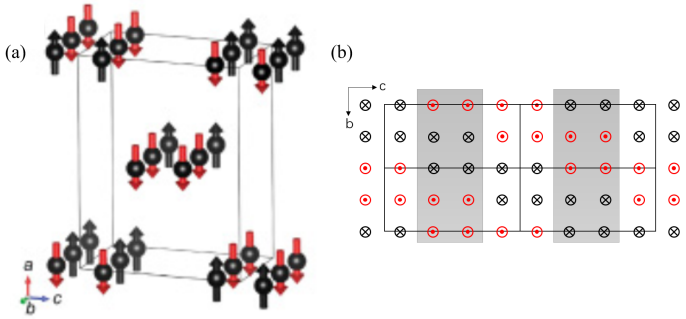

Figure 2.9: (a) Block-B magnetic structure of $BaFe_2Se_3$ [4]. (b) Projection on the bc-plane of (a). The Ladder-A and Ladder-B are indicated by the white and grid backgrounds, respectively.

On the other hand, $BaFe_2S_3$, a parent compound of $BaFe_2Se_3$, exhibits a stripe-like antiferromagnetic order below 120 K at ambient pressure [9]. The moments in $BaFe_2S_3$ are along the rung direction. Besides, two ferromagnetically coupled Fe form a stripe while the stripes are antiferromagnetically ordered along the leg direction [Fig. 2.10].

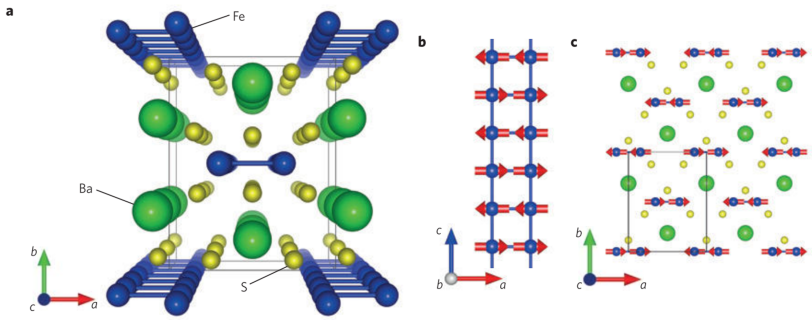

Figure 2.10: Magnetic structure of $BaFe_2S_3$. (a) The crystal structure of $BaFe_2S_3$. (b) Spin direction in the ladder. (c) Magnetic structure viewed from the c-axis. [9]

The block AFM magnetic order is also reported in two dimensions with iron vacancies, such as in $Rb_{0.89}Fe_{1.58}Se_2$ [137] and $K_{0.8}Fe_{1.6}Se_2$ [121, 138], and is believed to be closely relevant to the orbital-selective Mott phase (OSMP) [139, 140]. In this OSMP, the competition between a standard Hubbard U repulsion and a robust Hund interaction J can lead to the coexistence of the metallic and Mott-insulating bands [Fig. 2.11(a)]. It follows that the narrow-band localized electrons are coexisting with the wide-band itinerant electrons [Fig. 2.11(b)] [141–143]. Recently, Mourigal et al. confirmed the relevance of the OSMP and block AFM order in $BaFe_2Se_3$ by inelastic neutron scattering (INS) experiments [144]. Besides, a theoretical study showed that a multi-orbital Hubbard model in the OSMP is compatible with the INS spin spectra [145]. Furthermore, the origin of block magnetism and its relation to the OSMP was also studied numerically within low-dimensional multi-orbital Hubbard models [146]. Besides, it was predicted that the magnetic phase of the ladder geometry can be mediated between different types, as shown in Figure. 2.11(c), by the global filling $n = N/L$, where N is the number of electrons and L is the system size [146].

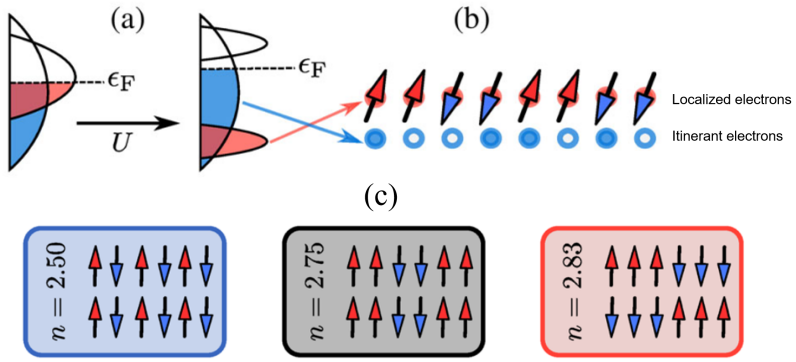

Figure 2.11: (a) Schematic representation of the orbital-selective Mott phase. The system is in a mixed state of metallic (left) and Mott-insulating (right) bands. (b) The block AFM state and itinerant electrons in the system. (c) Schematics of the spin configuration of magnetic orders induced by different n. Adapted from [146].

2.3.3 Under Pressure

Since $BaFe_2Se_3$ presents superconductivity only under pressure, a clear description of its magnetic state under pressure, particularly close to the SC phase, is very important. By first-principles calculation, Zhang et al. studied the pressure dependence of the magnetic structures of $BaFe_2Se_3$ [8] and $BaFe_2S_3$

[147]. Several magnetic arrangements have been tested, but only three of them stand out: Block-A, Block-B, and CX. These three magnetic models are shown in Figure 2.12 (a), (b), and (c), respectively. One should notice that the CX order of $BaFe_2Se_3$ differs from the stripe-type magnetic order of $BaFe_2S_3$ concerning the direction of the Fe moments. The moments are along the ladder direction for $BaFe_2Se_3$ and along the rung direction for $BaFe_2S_3$. For $BaFe_2Se_3$, at low pressure, the Block-B magnetic order has the lowest energy while the energy of Block-A is only 2.8% higher [Fig. 2.12(d)]. A transition from Block-B to CX occurs around 12 GPa, suggesting a pressure-induced magnetic phase transition. Besides, the local moments remain nonzero up to 30 GPa [Fig. 2.12(e)]. For $BaFe_2S_3$, the magnetic structure remains CX for all the pressure range, and the local moment vanishes before the superconducting phase [Fig. 2.12(f)].

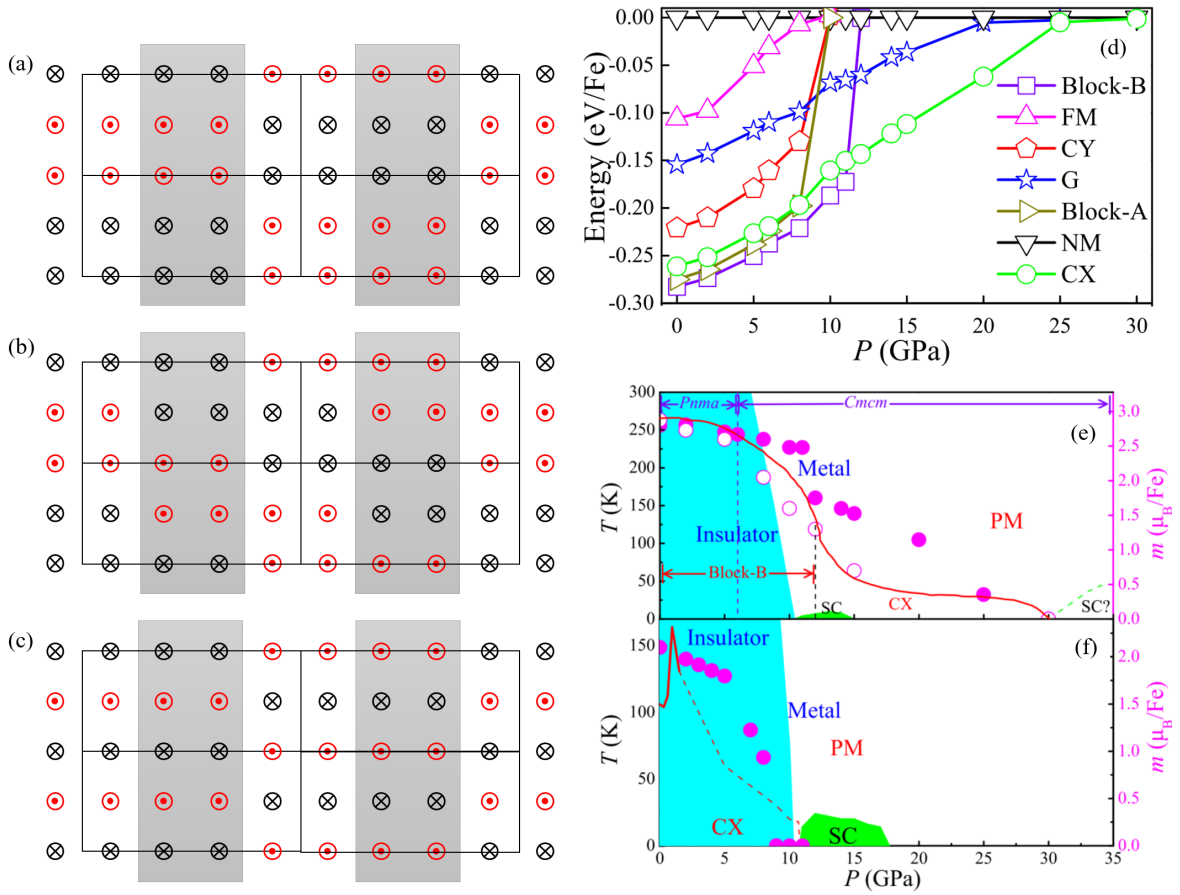

Figure 2.12: Projections of Fe viewed along the ladder direction for Block-A (a), Block-B (b), and CX (c) magnetic orders. The crystal axis is shown in *Pnma* setting. (d) Energies per Fe of the various magnetic orders [8]. (e) and (f) show the Pressure-Temperature phase diagrams of $BaFe_2Se_3$ and $BaFe_2S_3$, respectively [8]. The red solid lines are the AFM Néel temperatures from experimental results [1, 148]. Right axis: local magnetic moments. Open and solid circles come from experiment [1] and calculations [8, 147] respectively.

The evolution of the magnetic structure of $BaFe_2Se_3$ with pressure increasing was also studied by PND measurements and muon spin relaxation (μSR) spectroscopy [149]. The PND was performed at pressure up to 6.8 GPa and temperature down to 120 K. The long-range block magnetic state persists up to 4 GPa at 120 K. However, at 5.5 and 6.8 GPa, a short-range peak replaces the long-rang magnetic reflection. This indicates the transition to long-range magnetic order decreases below 120 K for 5.5 and 6.8 GPa. The μSR experiment was used to study the pressure dependence of T_N up to 2.43 GPa. A slight enhancement of T_N from 250 to 275 K is observed. Combine with the results from reference [1], the P-T phase diagram is shown in Figure 2.13.

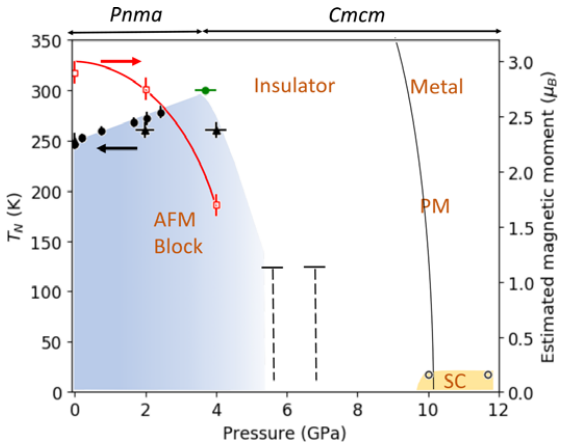

Figure 2.13: Pressure versus temperature phase diagram for $BaFe_2Se_3$ from experimental results [149]. The antiferromagnetic (AFM) transition temperature T_N (black symbols, left axis) and estimated ordered moment (red symbols, right axis) are shown. For the T_N determination, the filled circles and triangles represent the μSR and neutron diffraction results, respectively. The horizontal lines at the pressures of 5.5 and 6.8 GPa mark the lowest measured temperature of 120 K, at which the block-type short range magnetic correlations were observed. The green filled circle marks the structural transition [3.7(3) GPa] identified at room temperature. The superconducting dome and black line marking the metal-insulator transition are inferred from [1].

2.4 Electrical Properties

2.4.1 Resistivity and Superconductivity

The electrical resistivity of $BaFe_2Se_3$ shows an insulating behavior at ambient pressure [126, 127, 133, 134]. Besides, a 1D variable-range-hopping-type (VRH) behavior is confirmed, indicating a Mott-Anderson insulating nature, for $BaFe_2Se_3$ [133]. The energy gap deduced from the resistivity measurement varies from 0.09 to 0.3 eV, which may be caused by the inevitable defects or non-stoichiometry in the different samples. In addition, Ying et al. studied the resistance of $BaFe_2Se_3$ under pressure [1]. As we can see in Figure 2.14, the resistance gradually decreases with increasing pressure, and an insulator-metal transition starts to appear above 7.3 GPa. Most important, a superconducting phase is observed between 10 and 15 GPa below ~ 11 K.

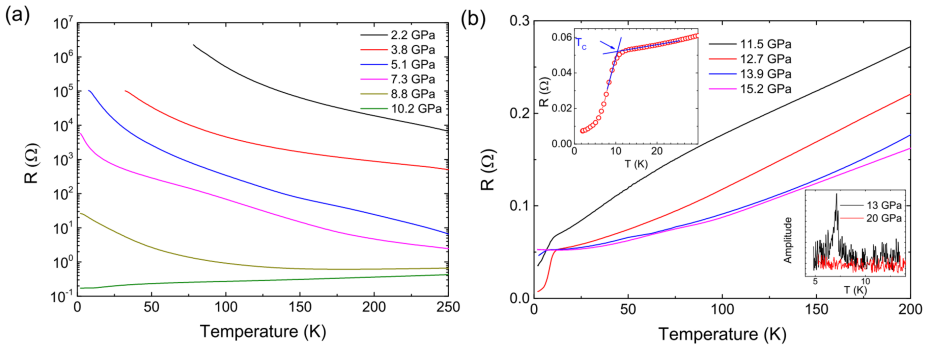

Figure 2.14: The temperature dependence of the resistance of $BaFe_2Se_3$ at various pressures. [1]

2.4.2 Electrical Polarization and Multiferroicity

.

Multiferroicity in $BaFe_2Se_3$ was first predicted by first-principles calculations based on density functional theory (DFT) [2]. From a symmetry analysis point of view, the block AFM order can break parity symmetry and display exchange striction effects. The Fe displacements induce the inequality of the Se-Fe distances above and below the ladder [Fig. 2.15(b)]. Combine with the tilting of the Fe ladders [Fig. 2.15(a)], a polarization will be produced in the magnetic phase. Meanwhile, the magnetic order of Block-A gives rise to a large polarization along the a-axis while Block-B introduces a small one along the c-axis [Fig. 2.15(d) and (e)]. Furthermore, the value of the polarization can be calculated by Landau theory. The possibility of a ferroelectric state in magnets can be examined by considering the symmetry allowed terms in the Landau potential [61, 150, 151]. Similar to AFM o-$HoMnO_3$ [152], the magnetoelectric coupling energy of each ladder in $BaFe_2Se_3$ can be expressed as [2]

$$F = \alpha(\mathbf{B}_1^2 - \mathbf{B}_2^2)P_\perp + \frac{1}{2\chi}\mathbf{P}^2, \tag{2.2}$$

where χ is the dielectric susceptibility of the paraelectric phase, α is the coefficient of exchange striction, $P_\perp$ is the ferroelectric component perpendicular to the Fe ladder plane. The parity order parameters $\mathbf{B}_1$ and $\mathbf{B}_2$ are defined as

$$\begin{aligned} \mathbf{B}_1 &= \mathbf{S}_1 + \mathbf{S}_2 + \mathbf{S}_3 + \mathbf{S}_4 - \mathbf{S}_5 - \mathbf{S}_6 - \mathbf{S}_7 - \mathbf{S}_8, \\ \mathbf{B}_2 &= \mathbf{S}_1 + \mathbf{S}_2 - \mathbf{S}_3 - \mathbf{S}_4 - \mathbf{S}_5 - \mathbf{S}_6 + \mathbf{S}_7 + \mathbf{S}_8, \end{aligned} \tag{2.3}$$

where $\mathbf{S}_i$ is the spin of the ith Fe atom in the ladder, as shown in Figure 2.15(b). By minimizing the energy F, the induced P perpendicular to the ladder can be obtained as $-\alpha\chi(\mathbf{B}_1^2 - \mathbf{B}_2^2)$. By the DFT calculations, $P_{Block-A}$ is determined as 2.01 $\mu C/cm^2$ without U (electronic interaction) and 3.02-3.22 $\mu C/cm^2$ with U which is almost along the a-axis [2]. On the other hand, $P_{Block-B}$ is one order of magnitude smaller (0.19 $\mu C/cm^2$ without U) and almost along the c-axis [Fig. 2.15(e)]. Thus, the results of the DFT calculations perfectly agree with the symmetry analysis above.

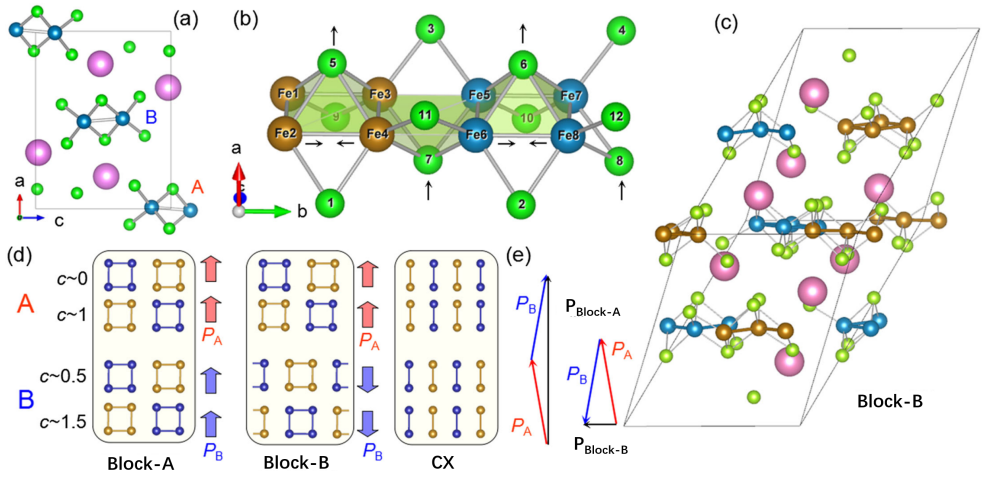

Figure 2.15: (a) Crystal structure of $BaFe_2Se_3$. (b) A Fe-Se ladder of $BaFe_2Se_3$ and its magnetic order. Partial ionic displacements driven by the exchange striction are marked by black arrows. (c) One unit cell of Block-B magnetic order. (d) Spin structures of Block-A, Block-B, and CX orders. The arrows denote the local electrical polarization of each ladder. in (b)-(d), the up and down spins are distinguished by colors (e) Vector of polarization of Ladders A and B. (Adapted from [2])

The direct measurement of electrical polarization in $BaFe_2Se_3$ is difficult because of two aspects. Firstly, $BaFe_2Se_3$ is too conductive at high temperatures (see in Figure 2.14). Secondly, the electric polarization is probably too weak to be evaluated by ferroelectric hysteresis measurement. Liu et al. tried to determine the transition temperature from the multiferroic phase to the paraelectric phase by measuring the dielectric properties [127]. They observed an anomaly around 150 K. However, this temperature is not the Néel transition temperature (~230 K) of this sample, making the macroscopic

ferroelectricity of $BaFe_2Se_3$ under debate. On the other hand, Chan et al. declared that no sign of ferroelectricity was observed in their dielectric study [153]. Another attempt to determine the polarization in $BaFe_2Se_3$ was made by Du and his coworkers [154]. A ferrielectric structural evolution was observed by the scanning transmission electron microscope (STEM). Figure 2.16 (a) and (b) show the color-enhanced high-angle annular dark-field scanning transmission electron microscopy (HAADF-STEM) images of the two ladders of $BaFe_2Se_3$ along b-axis and c-axis. The images are collected at room temperature. Displacements of Se and Fe ions can be clearly seen. Besides, the displacements are stronger in the top ladder (Strong ladder) than the other one (Weak ladder). This could be due to the different valence of Fe ions of the two ladders. Such ionic displacement can induce a polarization in the ladder according to reference [2] [indicated by the arrows in Figure 2.16(a)]. And the residual polarization of the two ladders is almost along the a-axis which is contrary to the expected small polarization along the c-axis [2]. Furthermore, Du et al. also characterized the polarity of $BaFe_2Se_3$ by SHG experiment [154]. The temperature dependence of the intensity of SHG signal and the polarization along a calculated based on HAADF-STEM images are shown in Figure 2.16(c). Both the SHG signal and the STEM data indicate that $BaFe_2Se_3$ exhibits ferroelectricity above $T_N \sim 250$ K, indicating the ferroelectricity is not magnetically induced but a primary polar property (contrary to the DFT calculation results of reference [2]). The polarization above T_N was also observed in reference [130].

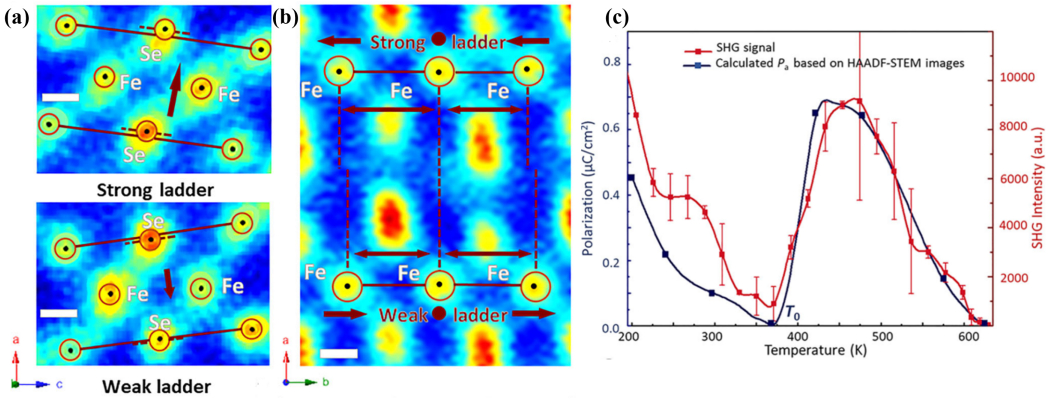

Figure 2.16: (a) and (b) Color-enhanced HAADF-STEM images of $BaFe_2Se_3$ along the b-axis and c-axis, respectively. The strong and weak ladders are distributed in an alternating order. Scale bar, 1 Å. (c) Left axis: the polarization along the a-axis (DFT calculated using the STEM structural data). Right axis: the SHG signal, which mainly reflects the evolution of polarization along the a-axis. (Adapted from [154])

2.5 Influence of Chemical Substitution

Table 2.1: Basic magnetic properties of several AFe_2B_3 compounds.

Compound	Space group	T_N (K)	m (μ_B), direction	Magnetic Structure	**k**	Ref.
$BaFe_2Se_3$	*Pnma*	256	2.8, ladder	Block-like	(1/2, 1/2, 1/2)	[4]
$BaFe_2S_3$	*Cmcm*	120	1.2, rung	Stripe-like	(1/2, 1/2, 0)	[9]
$CsFe_2Se_3$	*Cmcm*	175	1.8, leg	Stripe-like	(1/2, 1/2, 0)	[155]
KFe_2Se_3	*Cmcm*	250	2.1, leg	Stripe-like	(1/2, 1/2, 0)	[156]
$RbFe_2Se_3$	*Cmcm*	230	1.8-2, leg	Stripe-like	(1/2, 1/2, 0)	[157]

Before discussing the chemical substitution in $BaFe_2Se_3$, we first look at the analogues of $BaFe_2Se_3$. So far, several isomorphic compounds, such as AFe_2B_3 (A= K, Rb, Ba, Cs, Tl and B=Se, S, Te), in the

iron-based chalcogenide spin ladder family, have been discovered [3, 158–161]. Table 2.1 shows five widely studied compounds. Most of them crystallize in the *Cmcm* space group, except $BaFe_2Se_3$ which displays a crystal structure of *Pnma* space group. Meanwhile, they all display antiferromagnetism at low temperature. $BaFe_2Se_3$ has a block-like antiferromagnetic order with a propagation wave vector $\mathbf{k} = (1/2, 1/2, 1/2)$ while the others exhibit stripe-like order with $\mathbf{k} = (1/2, 1/2, 0)$. One should notice that the propagation wave vector $(1/2, 1/2, 0)$ in *Cmcm* would transfer to $(1/2, 0, 1/2)$ in *Pnma* setting. For the stripe-like orders, the direction of moments is along the rung for $BaFe_2S_3$, while it is along the leg for the others. Figure 2.17 shows the two types of stripe magnetic orders.

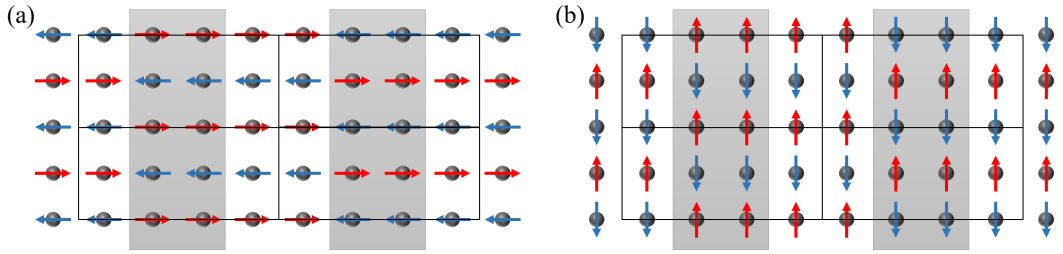

Figure 2.17: (a) Magnetic structure of $BaFe_2S_3$. (b) Magnetic structure of $CsFe_2Se_3$, KFe_2Se_3, and $RbFe_2Se_3$.

2.5.1 $Ba_{1-x}(K/Cs)_xFe_2Se_3$

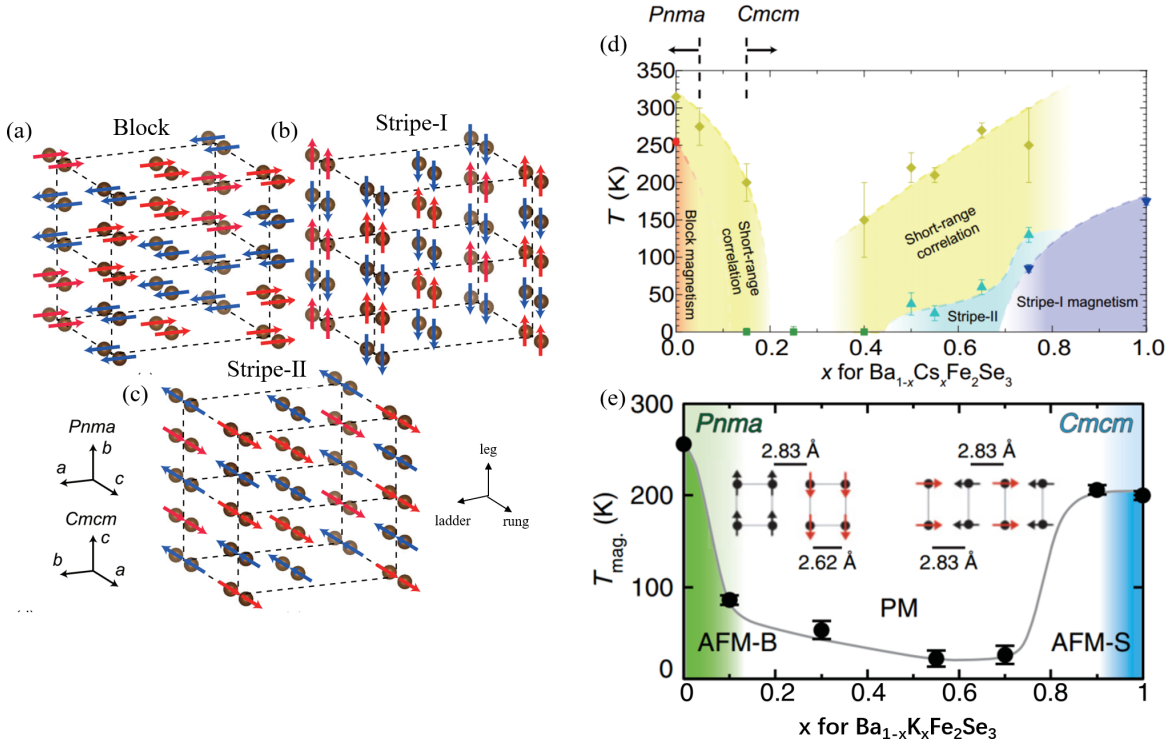

Figure 2.18: Block (a), Stripe-I (b), and Stripe-II (c) magnetic structures of $Ba_{1-x}Cs_xFe_2Se_3$. Adapted from reference [162]. (d) Magnetic phase diagram of $Ba_{1-x}Cs_xFe_2Se_3$ [162]. (e) Magnetic phase diagram of $Ba_{1-x}K_xFe_2Se_3$ [156]. The insets show the block-like order (AFM-B) of $BaFe_2Se_3$ and stripe-like order (AFM-S) of KFe_2Se_3. The black circles corresponds to susceptibility measurements.

Hawai et al. studied the magnetic phase diagram of $Ba_{1-x}Cs_xFe_2Se_3$ by PND [Fig. 2.18(d)] [162]. They showed that the block order of $BaFe_2Se_3$ is destabilized by the Cs doping. Only 5% of Cs doping can lead to the suppression of the long-range order and the appearance of a short-range order up to 290 K. For $x = 0.25$, the magnetic orders are completely suppressed. On the other hand, the stripe order of $CsFe_2Se_3$ is more robust. When x increases above 0.75, a stripe order (Stripe-I) with k-vector

of $(1/2, 1/2, 0)$ is stabilized at low temperature. In addition, a Stripe-II magnetic order emerges for x between 0.4 and 0.75. Note that stripe-II order is also a stripe-like magnetic structure but with a propagation vector of $(1/2, 0, 0)$. Besides, the direction of Fe moments shifts to the rung direction like in $BaFe_2S_3$. The Block, Stripe-I, and Stripe-II magnetic structures are shown in Figure 2.18 (a), (b), and (c), respectively. The electrical resistivity under pressure have been also studied for $Ba_{1-x}Cs_xFe_2Se_3$ [163]. Surprisingly, neither metallization nor superconductivity is observed for $BaFe_2Se_3$ ($x = 0$) and $CsFe_2Se_3$ ($x = 1$) up to 30 and 17 GPa, respectively. This is not consistent with the discovery of SC behavior in $BaFe_2Se_3$ by reference [1]. However, the superconductivity in $BaFe_2Se_3$ was confirmed by a recent research [164]. This difference between researches may be caused by a slight deviation from the ideal stoichiometry. Besides, a metallic behavior is confirmed for $x = 0.25$ and $x = 0.65$ for pressures greater than 11.3 and 14.4 GPa, respectively.

The magnetic structure of KFe_2Se_3 was studied by PND and pair-distribution function (PDF) analysis [156]. A stripe-like order with the moments along the leg direction was determined [Fig. 2.17(b)]. Besides, the magnetic transitions of $Ba_{1-x}K_xFe_2Se_3$ were studied by susceptibility measurements [156]. The phase diagram of $Ba_{1-x}K_xFe_2Se_3$ as a function of doping is shown in Figure 2.18(e). As in $Ba_{1-x}Cs_xFe_2Se_3$, the block-like order is suppressed quickly by K doping. At intermediate x, long-range magnetic order is likely replaced by a spin glass state. Besides, all samples are insulating and exhibit VRH behavior according to resistivity measurements.

2.5.2 $Ba(Fe_{1-x}Co_x)_2Se_3$

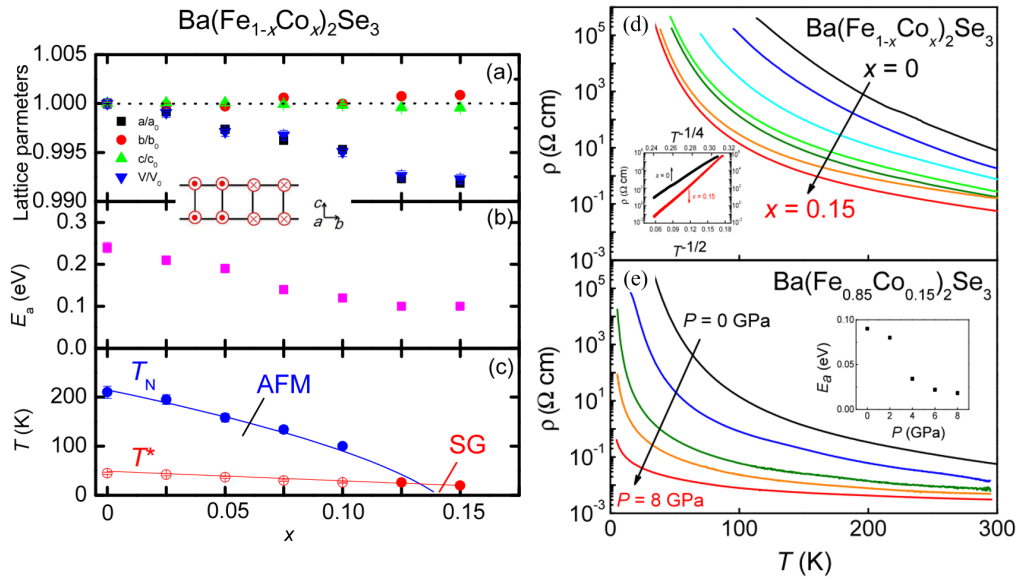

Figure 2.19: Doping dependences of the relative lattice parameters and volume (a), activation energy (b), and magnetic transition temperatures (c). (d) Temperature dependence of resistivity along the ladder direction for $Ba(Fe_{1-x}Co_x)_2Se_3$ at ambient pressure. The inset shows the fitting curves with the variable-range-hopping model. (e) Temperature dependence of resistivity under pressure for $Ba(Fe_{0.85}Co_{0.15})_2Se_3$. The inset shows the activation energy under pressure. Adapted from [165].

The highest Co substitution of 15% in $BaFe_2Se_3$ was achieved by a slow-cooling method [165]. The evolution of crystal structure, resistivity, and magnetic susceptibility of $Ba(Fe_{1-x}Co_x)_2Se_3$ was studied. Figure 2.19(a) shows a relative change of the unit cell parameters and volume extracted from powder x-ray diffraction measurements [165]. With the increase of Co, a decreases rapidly while b and c are slightly changed. Besides, the shrinkage of the volume is consistent with the smaller radius of Co^{2+} ions [166]. The insulating nature of $Ba(Fe_{1-x}Co_x)_2Se_3$ ($0 \leq x \leq 0.15$) is confirmed by temperature

dependence of the resistivity (ρ) measurement along the leg direction [Fig. 2.19(d)]. The system becomes closer to a metallic state with Co substitution. Besides, the charge gap (E_a), estimated by the fitting of ρ between 230 and 300 K with the thermal-activation-type equation, decreases from 0.24 eV to 0.09 eV by doping [Fig. 2.19(b)]. Figure 2.19(c) shows the evolution of the magnetic transition temperature with the Co substitution extracted from magnetic susceptibility measurements. Moreover, an anomaly (T^*) is observed for all samples. This anomaly is interpreted by a spin-glass-like transition [126, 133]. Both T_N and T^* are suppressed by increasing the Co concentration. The temperature dependence of the resistivity under pressure is studied for $Ba(Fe_{0.85}Co_{0.15})_2Se_3$ [Fig. 2.19(e)]. No metallic state is observed up to 8 GPa. The obtained activation energy is plotted in the inset of Figure 2.19(e).

2.5.3 $BaFe_2S_{3-x}Se_x$

Since both $BaFe_2Se_3$ and $BaFe_2S_3$ exhibit superconductivity under pressure, the intermediate compound $BaFe_2S_{3-x}Se_x$ is very intriguing and thus have been strongly investigated [164, 167–170]. A comprehensive phase diagram of $BaFe_2S_{3-x}Se_x$ ($0 \leq x \leq 3$) showing the evolution of the crystal structure, magnetic order, and thermal activation gap as a function of x is plotted in Figure 2.20. The abrupt enhancement of the activation gap around $x = 1.0$ is consistent with a first-order structural transition [Fig. 2.20(a)]. Between $x = 0.7$ and 1.0, the crystal structure changes from *Cmcm* to *Pnma* accompanied with a magnetic transition from stripe-like to block-like [Fig. 2.20(b)]. This indicates that the magnetic order is closely related to the crystal structure in $BaFe_2S_{3-x}Se_x$. Moreover, the resistance under pressure for $BaFe_2S_{2.25}Se_{0.75}$, which is close to the critical point of the system, has been investigated [164]. The temperature dependence of the electrical resistance of $BaFe_2S_{2.25}Se_{0.75}$ is shown in Figure 2.20(c) and (d). A metallization was achieved by increasing the pressure. Besides, the superconductivity was observed in the pressure range of 10-12 GPa below 11 K.

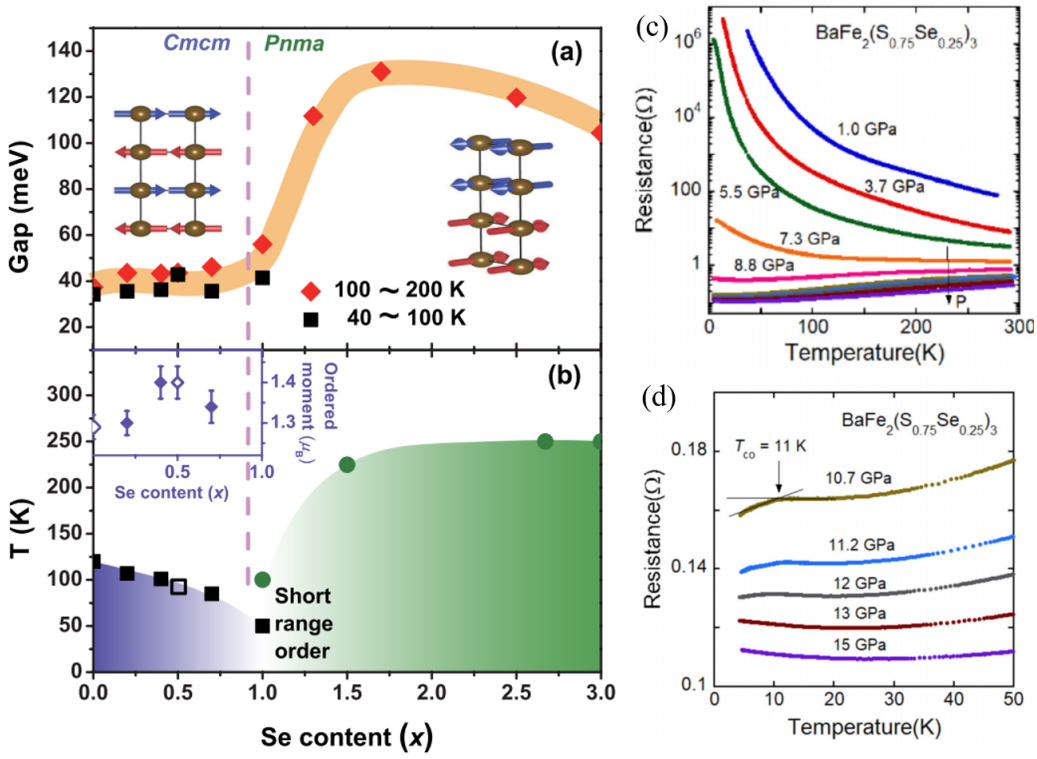

Figure 2.20: Phase diagram for the electronic state (a) and magnetic state (b) of $BaFe_2S_{3-x}Se_x$ [167]. (c) Temperature dependence of the electrical resistance of $BaFe_2S_{2.25}Se_{0.75}$. (d) The resistance curves between 10.7 GPa and 15 GPa in the low temperature range. [Figures (c) and (d) are from reference [164]]

2.5.4 $BaFe_{2+\delta}Se_3$

The Fe defaulted compounds $BaFe_{1.83}Se_3$ ($\delta = -0.17$) [126] and $BaFe_{1.79}Se_3$ ($\delta = -0.21$) [128] have been studied. The long-range antiferromagnetic order is strongly affected by the Fe deficiency: T_N decreases to 140 K for $BaFe_{1.83}Se_3$ and vanishes for $BaFe_{1.79}Se_3$. On the other hand, the Fe deficiency seems to have little influence on the crystal structure of $BaFe_2Se_3$. A *Pnma* space group was determined for both $BaFe_{1.83}Se_3$ and $BaFe_{1.79}Se_3$. As for the magnetic properties, a bifurcation between ZFC and FC magnetization curves was observed below 44 K for $\delta = -0.17$ when the applied field was along a and c axes, but not along b-axis [Fig. 2.21(a)]. The authors proposed $BaFe_{1.79}Se_3$ may be a canted antiferromagnet or spin glass which can give rise to a small FM component in the compound [126]. On the other hand, a ferromagnetic hysteresis loop is observed at 10 K in $BaFe_{1.83}Se_3$ [Fig. 2.21(b)]. The existence of two valence states of iron (Fe^{2+} and Fe^{3+}) in $BaFe_{1.83}Se_3$ was revealed by X-ray photoelectron spectroscopy measurements. The valence fluctuation or Fe_7Se_8 impurity could cause the FM behavior in the magnetization measurements.

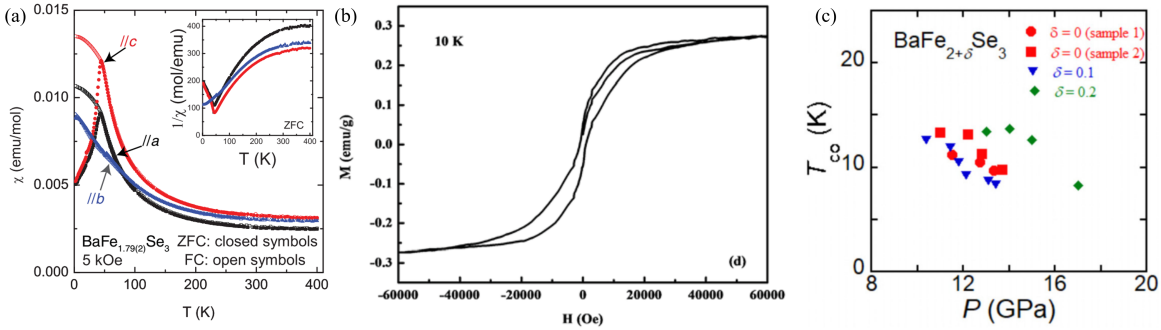

Figure 2.21: (a) Temperature dependence of the magnetization for $BaFe_{1.79}Se_3$ measured along a, b, and c axes under 5 kOe. The inset shows the reverse of the zero-field-cooled susceptibility data vs T [126]. (b) Magnetization hysteresis loop of $BaFe_{1.83}Se_3$ at 10 K [128]. (c) Pressure dependence of T_{co} for $BaFe_2Se_3$, $BaFe_{2.1}Se_3$, and $BaFe_{2.2}Se_3$ [164].

The Fe excess $BaFe_{2+\delta}Se_3$ has been also studied [164]. Contrary to the Fe defaulted compounds, the extra Fe did not vary transition temperature of $BaFe_{2+\delta}Se_3$ too much. The T_Ns of $BaFe_{2+\delta}Se_3$ are 242 K, 241 K, and 245 K for $\delta = 0$, $\delta = 0.1$, and $\delta = 0.2$, respectively. Besides, the electric resistivity under pressure was measured for $BaFe_{2+\delta}Se_3$. Figure 2.21(c) shows the pressure dependence of the transition temperature (T_{co}) of superconductivity for $BaFe_2Se_3$, $BaFe_{2.1}Se_3$, and $BaFe_{2.2}Se_3$. A relatively higher pressure is necessary for $BaFe_{2.2}Se_3$ to induce superconductivity.

2.6 Summary of this Chapter

In the present chapter, the state of the art of $BaFe_2Se_3$ has been presented. Two interesting properties, multiferroicity and superconductivity, were observed. Besides, plenty of chemical substitutions have been investigated by previous researches. Several magnetic structures were discovered in this family. Among them, $BaFe_2Se_3$ displays a unique block-like magnetic order with the propagation vector of $(1/2, 1/2, 1/2)$. Besides, the crystal structure of $BaFe_2Se_3$ under pressure was studied. A transition from *Pnma* to *Cmcm* was unveiled around 4 GPa. However, the crystal and magnetic structures at ambient pressure are still controversial. Besides, the magnetic structure under pressure, which is important to understand the relation between magnetism and superconductivity, remains unclear. This thesis is devoted to reveal these questions.

3

Experimental Techniques

Contents

The main proposal of our work is to study the crystal and magnetic structures of $BaFe_2Se_3$. Therefore, the X-ray and neutron scattering techniques are widely used in this thesis. Section 3.1 is devoted to the introduction of the basic theory of X-ray and neutron scattering. Section 3.2 and Section 3.3 present some common knowledge of crystallography and diffraction, respectively. The experimental applications of X-ray and neutron are given in Section 3.4 and Section 3.5, respectively. Then, several data analysis tools are introduced in Section 3.6. Finally, we present the synthesis and characterization of our $BaFe_2Se_3$ sample in Section 3.7.

3.1 Scattering

In condensed matter physics, scattering is a term to describe a physical process where a beam of certain particles, such as electrons, photons (X-ray), and neutrons, interacts with a sample and deviates from its original path. By studying the variation of the beam after scattering, researchers can obtain information about both the static and dynamic properties of the sample. Besides, there are two types of scattering: i) the elastic scattering in which the energy of the probing particles does not change during the scattering process; ii) the inelastic scattering in which the energy of the probing particles changes during the scattering process.

3.1.1 Elastic and Inelastic Scatterings

Figure 3.1 shows the geometric illustration of the two scattering processes. The incident and scattered beams are indicated by the wave vector $\mathbf{k}_i$ and $\mathbf{k}_f$. The wave vector $|\mathbf{k}| = 2\pi/\lambda$, where λ is the beam's wavelength and can be deduced from the energy of the particles. For X-rays $\lambda[\text{Å}] = 12.4/E[\text{keV}]$, for neutrons $\lambda[\text{Å}] = 0.24/(E[\text{eV}])^{1/2}$. The scattering vector $\mathbf{Q}$ is defined as $\mathbf{Q} = \mathbf{k}_i - \mathbf{k}_f$. In the elastic scattering, the kinetic energy of the scattered beam is identical to the incident one ($|\mathbf{k}_f| = |\mathbf{k}_i|$), but its direction is changed. As for the inelastic scattering, the energy of the incident particle is lost or increased by interacting with the sample ($|\mathbf{k}_f| \neq |\mathbf{k}_i|$). In summary, the kinetic energy of the beam is conserved in the elastic scattering but not in the inelastic scattering.

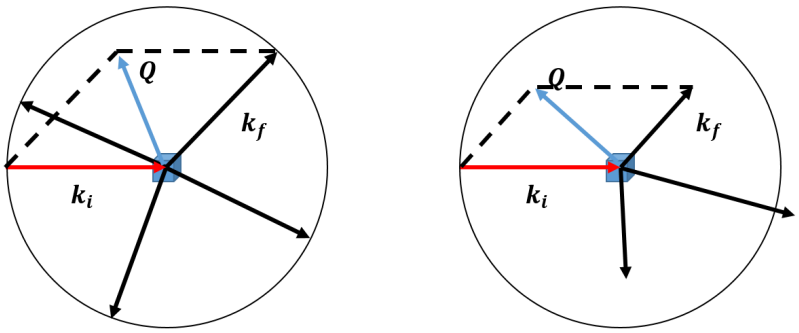

Elastic scattering
$|k_i| = |k_f|$

Inelastic scattering
$|k_i| \neq |k_f|$

Figure 3.1: Geometric illustrations for the elastic and inelastic scatterings. Adapted from [171].

3.1.2 Scattering Cross-Section

The cross-section is a measure describing the ability of a sample to scatter the probing particles. Moreover, it is also the quantities actually measured in a scattering experiment. As shown in Figure 3.2, an incident beam is put on the sample along the z direction. The total scattering cross-section is defined as:

$$\sigma_{total} = \frac{\text{total number of particles scattered per second in all directions}}{\Phi}, \tag{3.1}$$

where Φ is the flux of the incident beam. Generally, σ_{total} is given for each atom or nucleus instead of for the entire sample. The unit of the cross-section is an area, more specifically the barn (b) and 1 b = 10^{-28} m^2. It can be thought as the effective area of the atom which interacts with the beam.

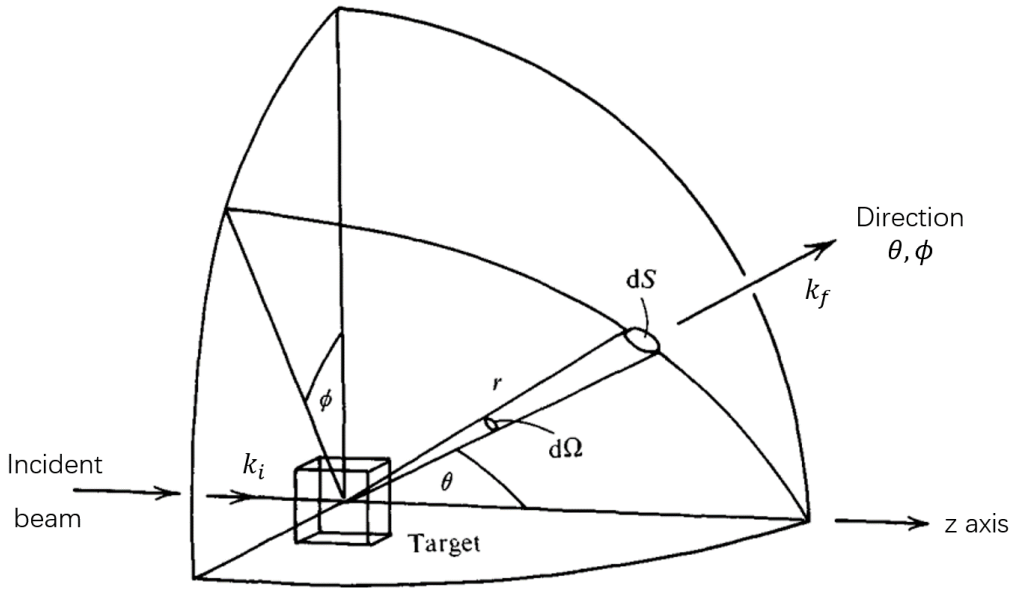

Figure 3.2: Geometry for a scattering experiment. (Adapted from [171])

If we consider the number of scattered particles in a certain direction θ, ϕ [Fig. 3.2], the differential cross-section can be obtained:

$$\frac{\mathrm{d}\sigma}{\mathrm{d}\Omega} = \frac{\text{number of particles scattered per second into a solid angle d}\Omega \text{ in the direction } \theta, \phi}{\Phi \mathrm{d}\Omega}. \tag{3.2}$$

This cross-section is usually measured in the elastic scattering as it does not include an energy component. On the other hand, the partial differential cross-section will be measured in the inelastic scattering. The partial differential cross-section is defined as:

$$\frac{\mathrm{d}^2\sigma}{\mathrm{d}\Omega \mathrm{d}E_f} = \frac{\begin{array}{c}\text{number of particles scattered per second into d}\Omega \text{ in the} \\ \text{direction } \theta, \phi \text{ with an energy between } E_f \text{ and } E_f + \mathrm{d}E_f\end{array}}{\Phi \mathrm{d}\Omega \mathrm{d}E_f}, \tag{3.3}$$

where E_f is the energy of scattered beam.

3.1.3 Scattering Length

Scattering for a single atom

When a beam is scattered by a single atom, as shown in Figure 3.3(a), the incident beam at point $\mathbf{r}$ can be treated as a plane wave $\psi_i(\mathbf{r})$ with the form:

$$\psi_i(\mathbf{r}) = e^{i\mathbf{k}_i\cdot\mathbf{r}}. \tag{3.4}$$

If the wave length of the beam (λ) is close to the size of an atom (~1 Å), the scattering will result in a spherical wave [Fig. 3.3(a)]. Assuming the atom is placed at $\mathbf{r}'$, the scattered wave ψ_f at point $\mathbf{r}$ can be written as:

$$\psi_f(\mathbf{r}) = \psi_i(\mathbf{r}')\frac{-b}{|\mathbf{r}-\mathbf{r}'|}e^{ik_f|\mathbf{r}-\mathbf{r}'|}, \tag{3.5}$$

where b is the scattering length which describes the scattering strength of the atom. In the scattering experiments, the actually measured intensity is the modulus square of the final wave function ($|\psi_f(\mathbf{r})|^2$), instead of the wave function directly. The differential cross-section $\mathrm{d}\sigma/\mathrm{d}\Omega$ in the elastic scattering can be calculated from the expressions for $\psi_i(\mathbf{r})$ and $\psi_f(\mathbf{r})$ in (3.4) and (3.5). If the velocity of the particles is v and keeps the same value before and after scattering, the number of neutrons passing through the area $\mathrm{d}S$ per second is

$$v\mathrm{d}S|\psi_f(\mathbf{r})|^2 = v\mathrm{d}S\frac{b^2}{r^2} = vb^2\mathrm{d}\Omega, \tag{3.6}$$

(see Fig. 3.2). The flux of incident beam is

$$\Phi = v|\psi_i(\mathbf{r})|^2 = v. \tag{3.7}$$

Therefore, the differential cross-section is obtained as

$$\frac{\mathrm{d}\sigma}{\mathrm{d}\Omega} = \frac{vb^2\mathrm{d}\Omega}{\Phi\mathrm{d}\Omega} = b^2, \tag{3.8}$$

and the total cross-section is

$$\sigma_{total} = 4\pi b^2. \tag{3.9}$$

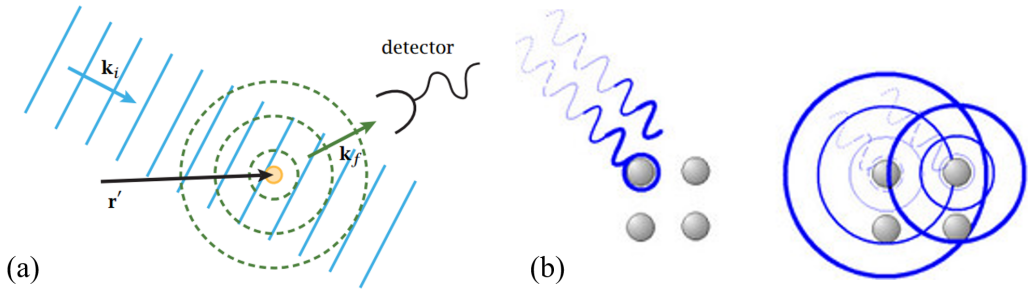

Figure 3.3: (a) A plane wave is scattered by a single atom. (b) A plane wave is scattered by multiple atoms.

Scattering for multiple atoms

If the beam is scattered by more than one atom in the sample, as shown in Figure 3.3(b), the wave function after scattering will be a sum of the scattered waves of individual atoms:

$$\psi_f(\mathbf{r}) = \sum_j \psi_i(\mathbf{r}_j)\frac{-b_j}{|\mathbf{r}-\mathbf{r}_j|}e^{ik_f|\mathbf{r}-\mathbf{r}_j|}. \tag{3.10}$$

Here it has been assumed that the flux of the incident beam is the same for each atomic position $\mathbf{r}_j$. Now, we apply a coordinate system with an origin far away from the sample, i.e. $r \gg |\mathbf{r}_i - \mathbf{r}_j|$ for any i, j. Since the components of $\mathbf{r}_i$ parallel to $\mathbf{k}_f$ are much bigger than the perpendicular components, $k_f|\mathbf{r} - \mathbf{r}_j|$ can be rewritten as $\mathbf{k}_f \cdot (\mathbf{r} - \mathbf{r}_j)$, and $|\mathbf{r} - \mathbf{r}_j|$ in the denominator becomes r. Consider (3.4), equation (3.10) thus can be rewritten as

$$\begin{aligned} \psi_f(\mathbf{r}) &= \sum_j e^{i\mathbf{k}_i \cdot \mathbf{r}_j} \frac{-b_j}{r} e^{i\mathbf{k}_f \cdot (\mathbf{r} - \mathbf{r}_j)} \\ &= e^{i\mathbf{k}_f \cdot \mathbf{r}} \sum_j \frac{-b_j}{r} e^{i\mathbf{Q} \cdot \mathbf{r}_j}. \end{aligned} \tag{3.11}$$

Therefore, the actual measured scattered intensity can be calculated as

$$\frac{\mathrm{d}\sigma}{\mathrm{d}\Omega} = |\sum_j b_j e^{i\mathbf{Q} \cdot \mathbf{r}_j}|^2. \tag{3.12}$$

3.2 A Little Crystallography

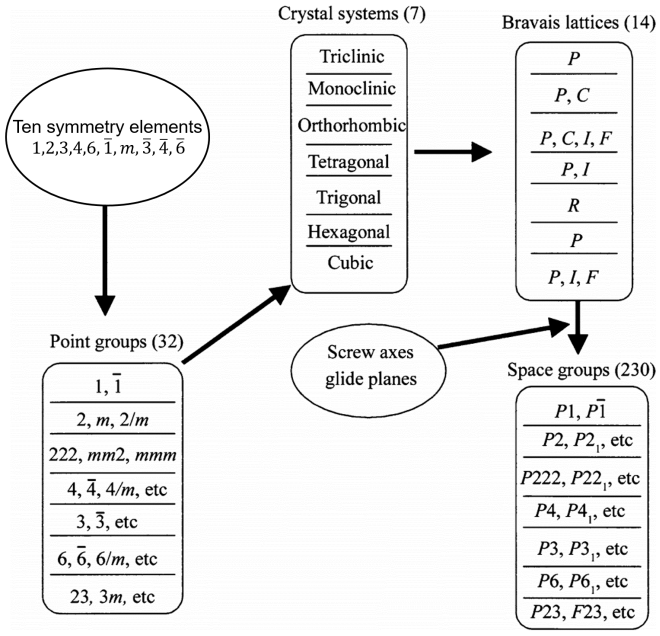

Figure 3.4: Symmetry elements in crystals and their relationships for classification [172].

Crystallography is a systematic method to describe how crystals are built: the infinite repetition of identical structural units (unit cells) in space. Crystals are solids in which the atoms, ions, or molecules are periodically arranged in three dimensions. Moreover, the arrangement of particles in a crystal follows certain symmetries. Mathematically, if we think of the particles as points, these symmetries can be classified into 32 point groups on the basis of ten symmetry elements: identity (1), n-fold rotation axis ($n = 2, 3, 4, 6$), inversion centre ($\bar{1}$), reflection plane (m), and n-rotoinversion axis ($\bar{n} = \bar{2}(m), \bar{3}, \bar{4}, \bar{6}$). There are seven crystal systems for classification, consisting of 14 Bravais lattices. Furthermore, by considering the additional symmetries due to the fact that a crystal is made of particles instead of points, several other symmetry operations can occur: screw axes and glide planes. Finally,

the symmetry of the crystal can be extended to 230 space groups. These relations are illustrated in Figure 3.4.

Generally, space groups are written by the international (Hermann–Mauguin) symbols such as *Pnma*. The Hermann–Mauguin symbols consist of two parts. (i) The first capital letter indicates the centering type of the conventional cell, such as *P* for primitive, *C* for C-face centered, etc. (ii) The one, two, or three symbols (letter and/or number) after the centering letter refer to the one, two, or three symmetry directions of the lattice belonging to the space group. The symmetry directions and their relation with different lattices are summarized in Table 3.1. Symmetry directions occur either as singular directions (as in orthorhombic lattice) or as sets of symmetrically equivalent symmetry directions (as cubic lattice). Besides, symmetry planes are represented by their normal direction. For example, in the *Pnma* space group, the normal of the *n* diagonal glide plane is along the *a*-axis. The details are available in the *International Tables for Crystallography* published by the International Union of Crystallography [173].

Table 3.1: Lattice symmetry directions for three dimension [173].

Bravais Lattice	Symmetry direction		
	Primary	Secondary	Tertiary
Triclinic	None		
Monoclinic	[010] (unique axis b) [001] (unique axis c)		
Orthorhombic	[100]	[010]	[001]
Tetragonal	[001]	$\{[100]\ [010]\}$	$\{[1\bar{1}0]\ [110]\}$
Hexagonal	[001]	$\{[100]\ [010]\ [\bar{1}\bar{1}0]\}$	$\{[1\bar{1}0]\ [120]\ [\bar{2}\bar{1}0]\}$
Rhombohedral (hexagonal axes)	[001]	$\{[100]\ [010]\ [\bar{1}\bar{1}0]\}$	
Rhombohedral (rhombohedral axes)	[111]	$\{[1\bar{1}0]\ [01\bar{1}]\ [\bar{1}01]\}$	
Cubic	$\{[110]\ [010]\ [001]\}$	$\{[111]\ [1\bar{1}\bar{1}]\ [\bar{1}1\bar{1}]\ [\bar{1}\bar{1}1]\}$	$\{[1\bar{1}0][110]\ [01\bar{1}][011]\ [\bar{1}01][101]\}$

3.2.1 Crystal Structure

In crystallography, the crystal structure is a description of the ordered arrangement of atoms in a crystalline material. The periodic arrangement of atoms is described by Bravais lattice. The Bravais lattice is a coordinate system which can be described in three dimensional space by:

$$\mathbf{R} = n_1\mathbf{a} + n_2\mathbf{b} + n_3\mathbf{c}, \tag{3.13}$$

where n_i are integers, **a**, **b**, and **c** are the basis vectors. Besides, the lattice parameters a, b, c, α, β, and γ indicate the lengths and angles of the basis vector, as shown in Figure 3.5. A unit cell is defined as

the smallest repeating unit of the lattice. The atomic position **r** in the unit cell is described in terms of the fractional coordinates (x, y, z) along the basis vectors:

$$\mathbf{r} = x\mathbf{a} + y\mathbf{b} + z\mathbf{c}. \tag{3.14}$$

Therefore, in Figure 3.5, there are two atoms per unit cell with the coordinates $(0, 0, 0)$ and $(1/2, 1/2, 1/2)$. Moreover, the absolute position of atom j in the unit cell n can be written as:

$$\mathbf{r}_{j,n} = \mathbf{r}_j + \mathbf{R}_n. \tag{3.15}$$

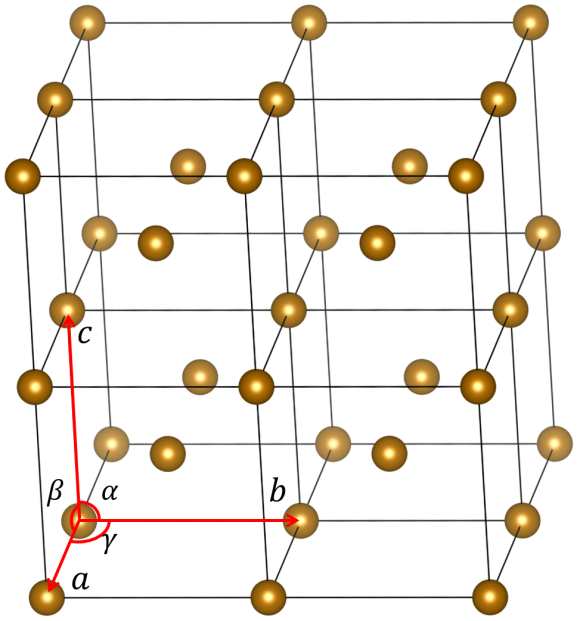

Figure 3.5: Illustration of a body-centered lattice. The unit cells are indicated by the black lines. The lattice parameters a, b, c, α, β, and γ are also shown.

3.2.2 Reciprocal Space

The reciprocal space is a three-dimensional (3D) space which has a reciprocal relationship with the real crystalline space. It can simplify the interpretation of the diffraction patterns. For given basis vectors of real space **a**, **b**, and **c**, the corresponding basis vectors $\mathbf{a}^*$, $\mathbf{b}^*$, and $\mathbf{c}^*$ in the reciprocal space can be written as:

$$\begin{aligned} \mathbf{a}^* &= \frac{2\pi}{V}\mathbf{b} \times \mathbf{c}, \\ \mathbf{b}^* &= \frac{2\pi}{V}\mathbf{c} \times \mathbf{a}, \\ \mathbf{c}^* &= \frac{2\pi}{V}\mathbf{a} \times \mathbf{b}, \end{aligned} \tag{3.16}$$

where $V = \mathbf{a} \cdot (\mathbf{b} \times \mathbf{c})$ is the volume of the real-space unit cell. Besides, it is worth to notice that these basis vectors are usually used in the inelastic scattering. And for the elastic scattering, researchers usually use the basis vectors without 2π ($\mathbf{a}^* = \frac{\mathbf{b}\times\mathbf{c}}{V}$, $\mathbf{b}^* = \frac{\mathbf{c}\times\mathbf{a}}{V}$, and $\mathbf{c}^* = \frac{\mathbf{a}\times\mathbf{b}}{V}$).

Each point in the reciprocal space corresponds to a family of planes in the real space. These lattice planes are indicated by the Miller indices (hkl) and orthogonal to the reciprocal vector

$$\boldsymbol{\tau}_{hkl} = h\mathbf{a}^* + k\mathbf{b}^* + l\mathbf{c}^*, \tag{3.17}$$

where h, k, and l are integers. Therefore, the distance between two planes can be calculated from the corresponding reciprocal lattice vector:

$$d_{hkl} = \frac{2\pi}{|\boldsymbol{\tau}_{hkl}|}. \tag{3.18}$$

And, as shown in Figure 3.6, d_{100} is twice of d_{200} while $|\boldsymbol{\tau}_{100}|$ is half of $|\boldsymbol{\tau}_{200}|$.

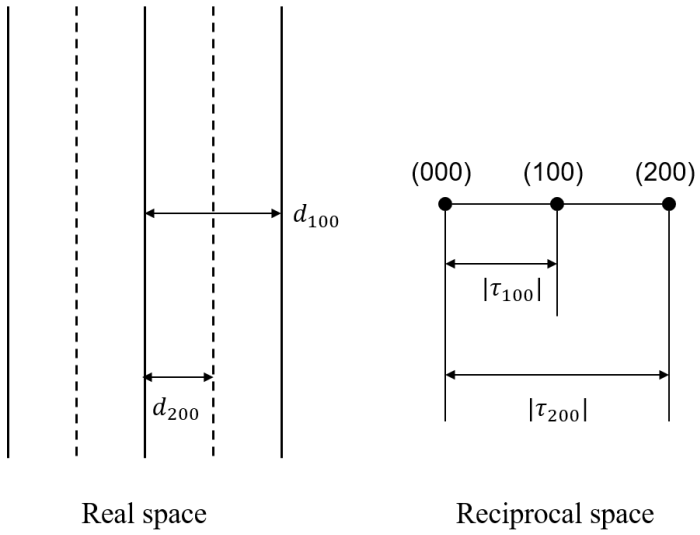

Figure 3.6: Illustration of lattice planes in real space and their corresponding lattice vectors in reciprocal space.

3.2.3 Wyckoff Positions

The Wyckoff positions always appear when one is trying to describe a crystal structure. They tell us where the atoms can be found. Usually, a Wyckoff position consists of a number and a letter such as $8d$. The number is the multiplicity of the site, indicating how many atoms are generated by the symmetry if a single atom is placed at this position. The letter, called Wyckoff letter, is simply a label and assigned alphabetically from the most symmetrical Wyckoff sites to the less symmetrical ones (general positions). Figure 3.7 shows the Wyckoff positions of *Pnma* space group. The first block is the general positions corresponding to an atom at an arbitrary position. The atoms on the general positions are left invariant only by the identity operation (1). The remaining blocks are the special positions corresponding to atoms lying upon one of the symmetry elements (shown with the third column of the block). Each of these atoms will be mapped onto itself by the identity and at least one further symmetry operation of the space group. Therefore, the general position always has the largest multiplicity. Besides, the Coordinates column in Figure 3.7 gives the coordinates of the equivalent atoms in the unit cell for corresponding Wyckoff positions.

3.3 Elastic Scattering or Diffraction

Generally, *diffraction* refers to various behaviors of wave when it encounters an obstacle or opening. It happens when the size of the obstacle/opening is comparable to the wavelength. When people are dealing with the scattered wave by atoms, diffraction is an alternative term for elastic scattering. This section will focus on the diffractions of X-ray and neutron since they are the main probing methods used in this thesis.

Positions

Multiplicity, Wyckoff letter, Site symmetry			Coordinates			
8	d	1	(1) x,y,z	(2) $\bar{x}+\frac{1}{2},\bar{y},z+\frac{1}{2}$	(3) $\bar{x},y+\frac{1}{2},\bar{z}$	(4) $x+\frac{1}{2},\bar{y}+\frac{1}{2},\bar{z}+\frac{1}{2}$
			(5) $\bar{x},\bar{y},\bar{z}$	(6) $x+\frac{1}{2},y,\bar{z}+\frac{1}{2}$	(7) $x,\bar{y}+\frac{1}{2},z$	(8) $\bar{x}+\frac{1}{2},y+\frac{1}{2},z+\frac{1}{2}$
4	c	$.m.$	$x,\frac{1}{4},z$	$\bar{x}+\frac{1}{2},\frac{3}{4},z+\frac{1}{2}$	$\bar{x},\frac{3}{4},\bar{z}$	$x+\frac{1}{2},\frac{1}{4},\bar{z}+\frac{1}{2}$
4	b	$\bar{1}$	$0,0,\frac{1}{2}$	$\frac{1}{2},0,0$	$0,\frac{1}{2},\frac{1}{2}$	$\frac{1}{2},\frac{1}{2},0$
4	a	$\bar{1}$	$0,0,0$	$\frac{1}{2},0,\frac{1}{2}$	$0,\frac{1}{2},0$	$\frac{1}{2},\frac{1}{2},\frac{1}{2}$

Figure 3.7: Wyckoff positions of *Pnma* space group.

3.3.1 The Laue Condition and Bragg's Law

In a diffraction experiment, if the atoms or molecules of the sample are periodically arranged, such as a single crystal, the intensity of the scattered beam will be enhanced along the directions where the scattering vector $\mathbf{Q}$[1] and the reciprocal lattice vector $\boldsymbol{\tau}$ have the relation of

$$\mathbf{Q} = \boldsymbol{\tau}. \tag{3.19}$$

This is called the *Laue condition*. Figure 3.8 shows an illustration of the Laue condition in the reciprocal space. If a detector is placed after the sample, one can obtain a diffraction pattern which contains information about the atomic arrangement of the sample. This is the main purpose of a diffraction experiment.

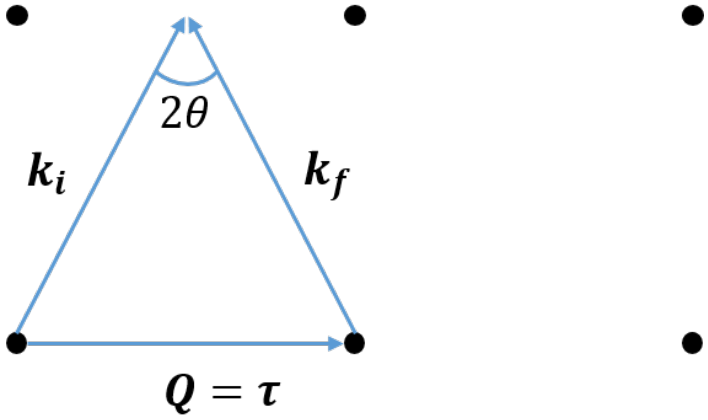

Figure 3.8: Relation between scattering vector ($\mathbf{Q}$) and reciprocal lattice vector $\boldsymbol{\tau}$ for the enhanced beam. 2θ denotes the angle between the incident beam and the scattered beam.

In the real space, an equivalent to the Laue condition is the Bragg's law. As shown in Figure 3.9(a), we can obtain

$$|\boldsymbol{\tau}| = 2|\mathbf{k}_f| \sin\theta. \tag{3.20}$$

From (3.18), we can show that $|\boldsymbol{\tau}| = 2\pi n/d$, where d is the distance of the nearest planes called the d-spacing and n is an integer. Combined with $|\mathbf{k}_f| = 2\pi/\lambda$, equation (3.20) becomes the Bragg's law or Bragg condition:

$$n\lambda = 2d \sin\theta. \tag{3.21}$$

[1]In the elastic scattering, $\mathbf{Q}$ is defined as $\mathbf{Q} = \mathbf{k}_f - \mathbf{k}_i$ while it is $\mathbf{Q} = \mathbf{k}_i - \mathbf{k}_f$ in the inelastic scattering.

Another way to derive the Bragg condition is shown in Figure 3.9(b). Considering that a crystal is made out of parallel planes of atoms with an interplanar distance of d, two beams 1 and 2 are scattered by the nearest lattice planes. For these two planes to interfere constructively, the difference in their path lengths should be an integer multiple of the wavelength ($n\lambda$). From Figure 3.9(b), we can show that the difference between beam 1 and 2 is $2d\sin\theta$. Therefore, we can also obtain equation (3.21).

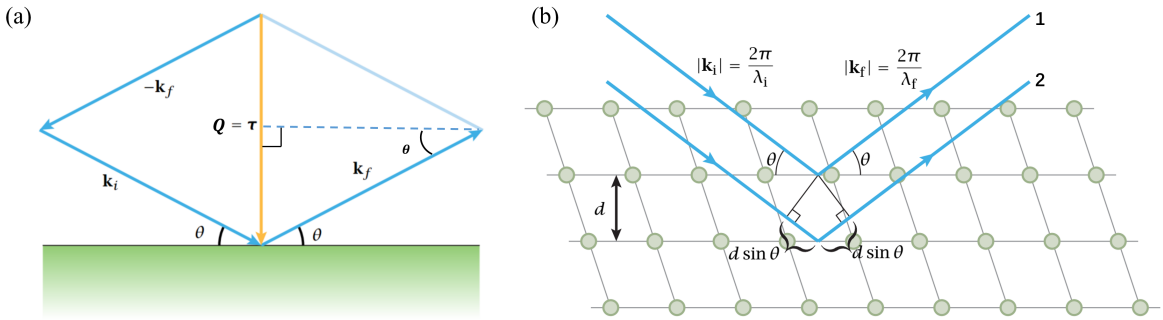

Figure 3.9: (a) Laue condition requires $\mathbf{Q} = \boldsymbol{\tau}$. (b) Illustration of the diffraction of a beam by a crystal (Bragg condition). Adapted from [91].

3.3.2 Ewald's Sphere

While the two conditions above are in numerical forms, Ewald's sphere is a geometrical way to illustrate the condition of diffraction for a certain wavelength λ. As shown in Figure 3.10(a), take the sample as the origin (S) and $2\pi/\lambda$ as the radius, we can obtain an Ewald's sphere. The origin of the reciprocal lattice (O^*) is at the point where the incident beam exits from the sphere. From Bragg's law, we can know that only the reciprocal lattice nodes on the sphere will produce diffraction beams.

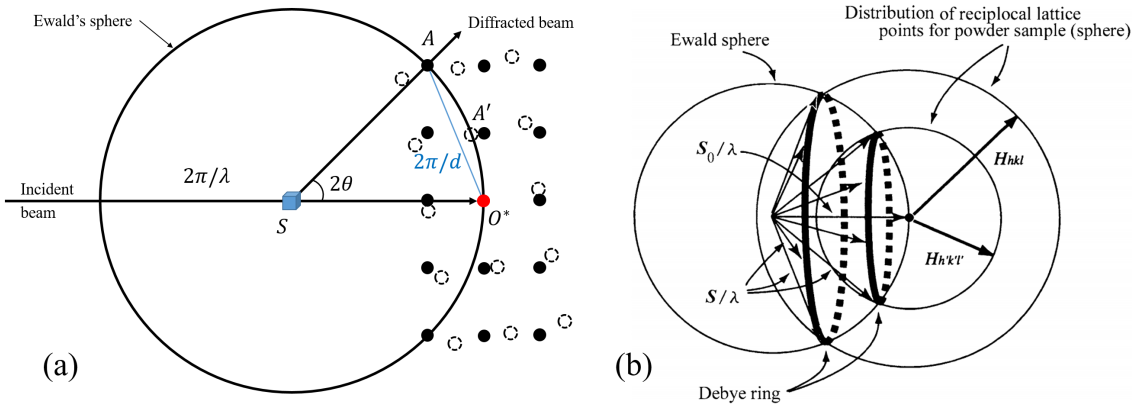

Figure 3.10: (a) Visualization of the diffraction condition in a crystal using the Ewald's sphere with radius $2\pi/\lambda$ and the reciprocal lattice projection in a plane of the reciprocal lattice. The lattice after rotation around O^* is shown as the dash circles. A and A' are the lattice dots on the Ewald's sphere. (b) Illustration of powder diffraction using the Ewald's sphere [172].

If the sample is a single crystal with a specific orientation, only a few reciprocal lattice nodes will be on the Ewald's sphere [A in the Figure 3.10(a)]. However, if the crystal is rotated, the reciprocal lattice will also be turned, leading to additional nodes on the sphere and more diffraction points [A' in the Figure 3.10(a)]. This procedure can be treated as the Ewald's sphere rotates around the center O^*. When Ewald's sphere scans the reciprocal space, the path will constitute a sphere with a radius of $4\pi/\lambda$. It is clear that only the nodes in this sphere will be observed. Thus, this sphere is called the limiting sphere. On the other hand, a crystalline powder sample is approximated by a very small poly-crystalline aggregate in which the orientations of the grains are randomly distributed. Therefore,

the diffraction dots of a powder sample will constitute some rings which are called Debye rings, as shown in Figure 3.10(b).

3.3.3 Diffraction from Crystals

In the diffraction from a crystal, the atomic position $\mathbf{r}_j$ in (3.12) can be split up using (3.15). Therefore, the scattering intensity becomes

$$\begin{aligned}\frac{\mathrm{d}\sigma}{\mathrm{d}\Omega} &= e^{-2W}|\sum_{j,n} b_j e^{i\mathbf{Q}\cdot(\mathbf{r}_j+\mathbf{R}_n)}|^2 \\ &= e^{-2W}|\underbrace{\sum_j b_j e^{i\mathbf{Q}\cdot\mathbf{r}_j}}_{F_{u.c.}(\mathbf{Q})}|^2|\underbrace{\sum_n e^{i\mathbf{Q}\cdot\mathbf{R}_n}}_{S_N(\mathbf{Q})}|^2,\end{aligned} \tag{3.22}$$

where e^{-2W} is the site-independent Debye-Waller factor, also known as the temperature factor. As we know, atoms in a crystal are moving around their mean positions by thermal vibration. The amplitude of such vibration increases with increasing temperature. If u is the displacement of atoms, the quantity of W is calculated by the following equation:

$$W = 8\pi^2 \left\langle u^2 \right\rangle \left(\frac{sin\theta}{\lambda}\right)^2, \tag{3.23}$$

where $\left\langle u^2 \right\rangle$ is the mean square displacement of the atom in the direction normal to the diffraction planes. Therefore, e^{-2W} is close to 1 for low temperature and low θ.

The first term of (3.22) $F_{u.c.}(\mathbf{Q})$ is the unit cell structure factor. The second term $S_N(\mathbf{Q})$ is called the lattice or cell sum, which is non-zero only in the Laue condition (3.19). That means, to make the scattering intensity $\mathrm{d}\sigma/\mathrm{d}\Omega$ non-zero, $\mathbf{Q}$ should be equal to $\boldsymbol{\tau}$. Therefore, the structure factor $F_{u.c.}(\mathbf{Q})$ becomes

$$F_{u.c.}(\mathbf{Q}) = \sum_j b_j e^{i\boldsymbol{\tau}\cdot\mathbf{r}_j}. \tag{3.24}$$

By applying (3.14) and (3.17), we can obtain

$$F_{u.c.}(\mathbf{Q}) = F_{hkl} = \sum_j b_j e^{2\pi i(hx_j+ky_j+lz_j)}. \tag{3.25}$$

which contains both the amplitude and the phase of the scattered wave of all atoms in the unit cell.

According to (3.22) and (3.25), the intensity of the final wave will only be non-zero when $F_{hkl} \neq 0$. For example, in the case of the body-centered cell in Figure 3.5, the two specific positions of atoms in the unit cell are (0,0,0) and $(\frac{1}{2}, \frac{1}{2}, \frac{1}{2})$. Thus, the structure factor is given as

$$F = be^{2\pi i\times 0} + be^{2\pi i\times(\frac{h}{2}+\frac{k}{2}+\frac{l}{2})} = b[1 + e^{2\pi i\times(\frac{h}{2}+\frac{k}{2}+\frac{l}{2})}] \tag{3.26}$$

When the number $(h + k + l)$ is even: $F = 2b$, $F^2 = 4b^2$
When the number $(h + k + l)$ is odd: $F = 0$, $F^2 = 0$.

This means, for the body-centered cell, the diffraction from the planes of the (110), (200), and (211) types will give a Bragg reflection, while the diffraction from the planes of the (111), (210), and (300) types will not. One should notice that the structure factor is completely independent of the shape and

Table 3.2: Reflection conditions of some Bravais lattice types.

Bravai Lattice type	Symbol	Condition for reflection to be present
Primitive	P	none
Face-centered lattice	F	$hkl : h+k, h+l, k+l = 2n$
Body-centered lattice	I	$hkl : h+k+l = 2n$
Base-centered lattice	A	$hkl : k+l = 2n$
	B	$hkl : h+l = 2n$
	C	$hkl : h+k = 2n$

size of the unit cell but depends on the nature of atoms. The conditions for reflection to be present for some Bravais lattice types are shown in Table 3.2.

On the other hand, the space group symmetries will introduce additional reflection conditions. Table 3.3 shows the general reflection conditions of three space groups used in this thesis. The reflection conditions could help to determine the space group of a compound as we will see in Chapter 4.

Table 3.3: General reflection conditions of $Pnma$, $Pmn2_1$, and Pm space groups. Notice that $Pmn2_1$ is a subgroup of $Pnma$ and Pm is a subgroup of $Pmn2_1$. The details can be found in [173].

$Pnma$	$Pmn2_1$	Pm
$0kl : k+l = 2n$	$h0l : h+l = 2n$	none
$hk0 : h = 2n$	$h00 : h = 2n$	
$h00 : h = 2n$	$00l : l = 2n$	
$0k0 : k = 2n$		
$00l : l = 2n$		

3.4 X-ray Diffraction

In 1895, Wilhelm Conrad Röntgen discovered a new kind of ray when he was studying cathode rays. He named it "X-ray" using the mathematical designation ("X"). Then, in 1912, the German physicist Max von Laue observed the diffraction of X-rays by crystals [174]. This discovery was immediately recognized as a sensation. Soon, Bragg's law was first proposed by William Lawrence Bragg and his father William Henry Bragg in 1913 [175]. The theory of X-ray diffraction offered a new way to probe the internal structure of crystals and provided a foundation for the later studies of electron and neutron diffractions.

X-rays are a form of electromagnetic radiation similar to radio waves, microwaves, visible light, and gamma (γ-)rays. The wavelength of X-rays (0.1 – 100 Å) is between ultraviolet rays and γ-rays (Fig. 3.11). X-rays with energy above 10 keV are called hard X-rays, while those with lower energy are called soft X-rays. Since the wavelength of hard X-rays is closed to the size of atoms (1 Å) in the crystal, they are used to determine crystal structures by X-ray crystallography.

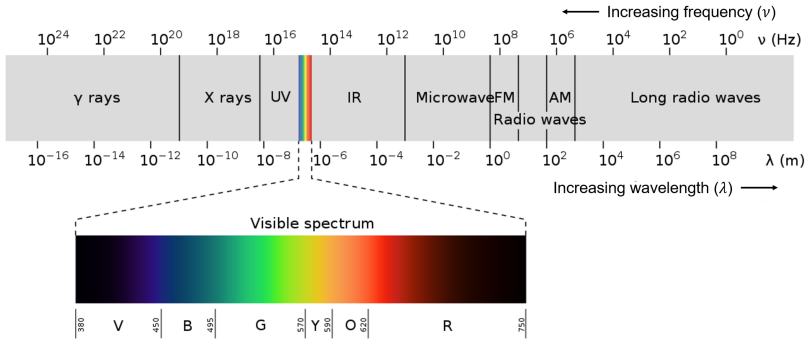

Figure 3.11: Electromagnetic spectrum.

3.4.1 X-ray Production

Generally, X-rays can be produced by variation of the motion of charged particles. The charged particles include electrons, ions, and any ionic groups. The variation of motion can be the change of the velocity or direction.

The most widely used apparatus to produce X-rays is the conventional X-ray tube, as shown in Figure 3.12. The electrons are emitted by the filament at the cathode and accelerated by a voltage induced at the anode. When the electrons hit the target, their kinetic energy will be transformed into X-rays and heat. The anode target materials include Cr, Fe, Co, Ni, Cu, Mo, Ag, and W, in which Cu and Mo are the most common targets.

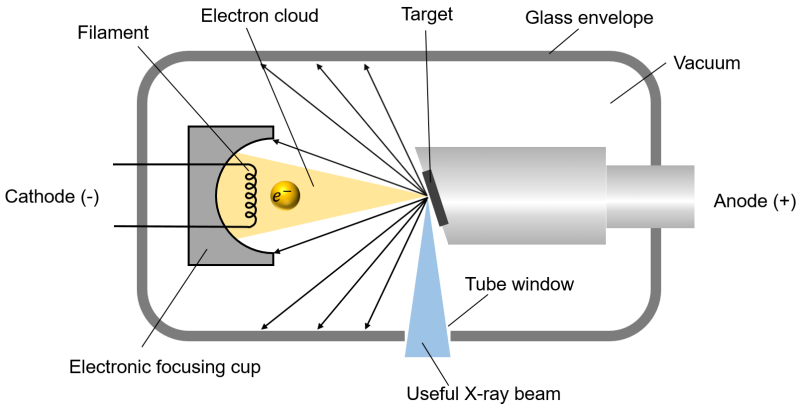

Figure 3.12: Schematics of a conventional X-ray tube [176]. The whole apparatus is under vacuum conditions.

When the electrons are stopped by the target, two different radiations will occur: bremsstrahlung radiation and characteristic radiation. The bremsstrahlung radiation is produced when electrons are decelerated by the interaction with nuclei [Fig. 3.13(a)]. Since the energies of emitted photons are different, a continuum spectrum will be observed [Fig. 3.13(b)]. On the other hand, if the incoming electrons have sufficiently high energy, they will create some electron vacancies in the atoms of the target. And the characteristic radiation will be emitted when outer-shell electrons fill the vacancies in the inner-shell. Since the energy of the emitted photon is equal to the energy difference between the outer-shell and inner-shell electrons, the energy spectrum of characteristic X-rays is a set of well-defined and separated peaks that correspond to the discrete energies between electronic levels [Fig. 3.13(b)]. Thus, the energy of the characteristic X-rays is related to the target material. Table 3.4 shows the wavelengths of characteristic X-rays for some materials. One should notice that the characteristic ray of the K_α spectrum usually splits into two rays, $K_{\alpha 1}$ and $K_{\alpha 2}$. Generally, the ratio of intensities is $K_{\alpha 1} : K_{\alpha 2} = 2 : 1$. Therefore, the intensity (I) of K_α can be calculated as $(I_{K_{\alpha 1}} + 2I_{K_{\alpha 2}})/3$.

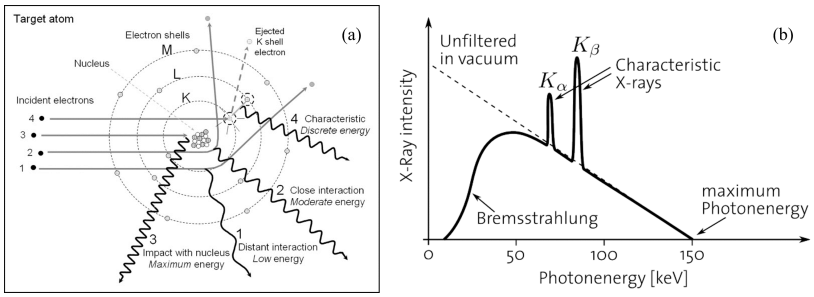

Figure 3.13: (a) Illustration of the bremsstrahlung (1,2,3) and characteristic (4) radiations [177]. (b) Typical X-ray spectrum produced by a X-ray tube [176].

Table 3.4: Wavelengths of characteristic X-rays for some materials.

Target	Wavelength (Å)			
	K_β	K_α	$K_{\alpha 1}$	$K_{\alpha 2}$
Cr	2.08479	2.2909	2.28962	2.29352
Fe	1.75654	1.9373	1.93597	1.93991
Co	1.62073	1.7902	1.78890	1.79279
Ni	1.50008	1.6591	1.65783	1.66168
Cu	1.39217	1.5418	1.54050	1.54434
Mo	0.63225	0.7107	0.70926	0.71354

Another source to produce X-rays is the synchrotron radiation (SR). The synchrotron is a circular particle accelerator which is specifically designed to produce electromagnetic radiation. Figure 3.14(a) shows the schematic illustration of a synchrotron source. The charged particles are accelerated by the linear accelerator and booster synchrotron. Then the high-speed particles travel in the storage ring and produce electromagnetic radiations along the tangent of the path. The energy of the produced X-rays in the synchrotron can be mediated in a wide range (1 meV - 100 keV). Compared to the conventional X-ray tube, the synchrotron source has many advantages, such as high photon flux, wide energy tunability, high spatial resolution, small beam size, etc. In this thesis, we performed synchrotron experiments in Synchrotron SOLEIL (Saint-Aubin, France). Figure 3.14(b) shows its beamlines.

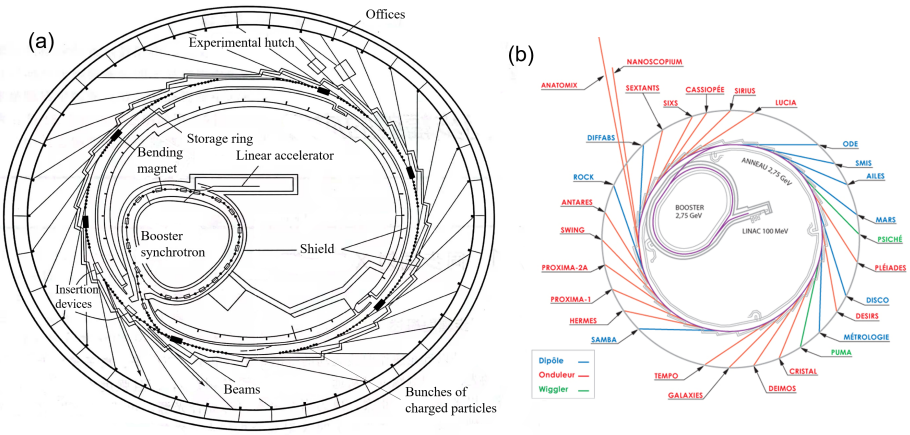

Figure 3.14: (a) Schematic illustration of a typical synchrotron source. The path of the charged particles in the storage ring is deflected by the bending magnets. (b) Beamlines of the synchrotron SOLEIL.

3.4.2 X-ray Diffraction Instruments

Four-circle Single-Crystal Diffractometer

The four-circle single-crystal diffractometer is a powerful instrument for determining the crystal structures (lattice parameters and atomic coordinates) of a crystal. As shown in figure 3.15(a), the sample is mounted at the center of an Eulerian cradle. There are four circles which can be adjusted: the detector circle (2θ), the sample circles ($\omega, \chi,$ and ϕ). According to Ewald's sphere illustration, for single-crystal diffraction measurements, we need to rotate the crystal to obtain more diffraction points. The four-circle diffractometer allows a rotation of the crystal with the three sample circles. Therefore, the collection of all the reciprocal lattice nodes achievable is possible. In this thesis, we used a more advanced Kappa diffractometer characterized by its κ-gonimometer, which differs from the conventional four-circle single-crystal diffractometer [Fig. 3.15(b)]. The sample can be rotated by κ, ϕ_κ, and ω, and the detector is rotated by 2θ. Taking off the Eulerian cradle makes it more flexible.

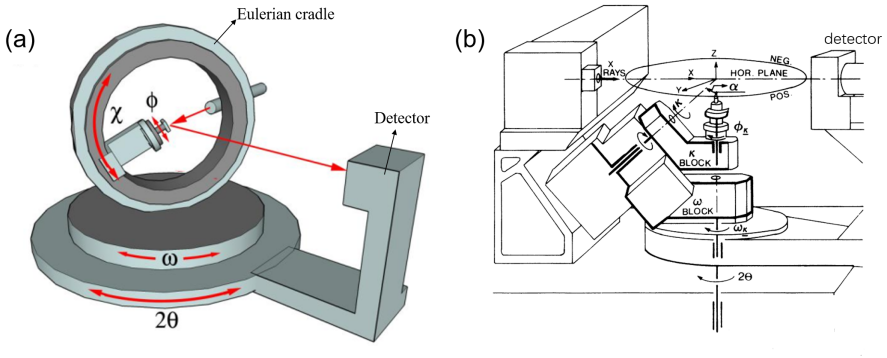

Figure 3.15: (a) Schematic illustration of the configuration of a conventional four-circle X-ray diffractometer [178]. (b) Schematic illustration of a Kappa diffractometer [179].

CRISTAL Beamline at Synchrotron SOLEIL

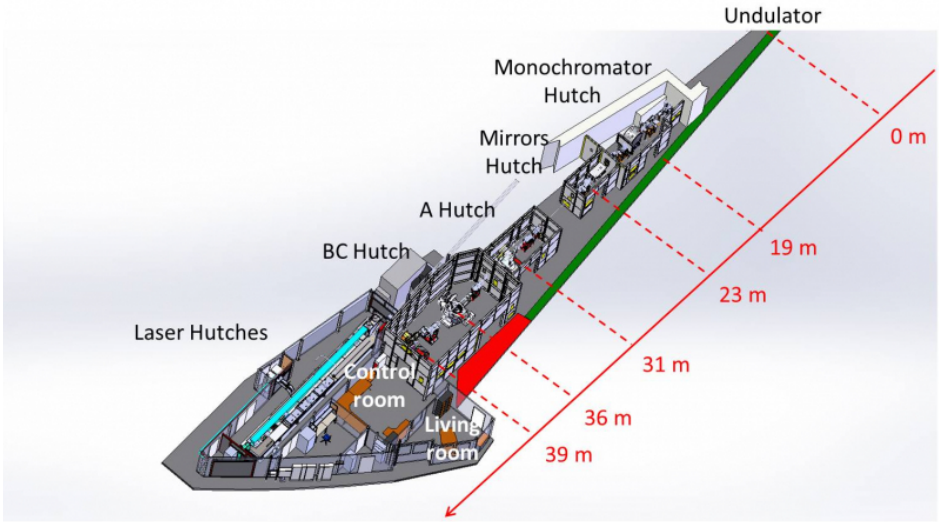

Figure 3.16: 3D schematic view of the CRISTAL beamline.

CRISTAL is an undulator-based multi-technique diffraction beamline, devoted to the studies of the structural properties of condensed matters at various conditions. Figure 3.16 shows the 3D schematic view of the beamline. An in-vacuum U20 undulator source, which offers an energy range between 5

keV and 30 keV, is settled at the beginning of the beamline. A Si(111)-double crystal monochromator and a mirror system consisting of two horizontal 300 mm long Si mirrors are used to mediate the beam. In A hutch, an Oxford Rigaku four-circle diffractometer is settled. It allows an easy, fast and precise data collection on single crystals. A two-circle diffractometer and a six-circle κ diffractometer is placed in the BC hutch. Most of the powder diffraction experiments are performed on the former. A complete powder diagram up to $2\theta = 100°$ can be collected in less than one hour. On the other hand, the six-circle diffractometer consists of four rotation axes for the sample stage (μ, $K\omega$, κ, and $K\phi$) and two rotation axes for the detector stage (Δ and Γ). These axes can accurately position the sample onto the center of the diffractometer.

Diffraction Under Pressure

To perform X-ray measurements under pressure, we used a diamond anvil cell (DAC) to apply the pressure. Compared to other pressure cells such as piston cylinders or indenters, DACs can reach higher pressures depending on the diameter of the diamond culet. Another advantage of DACs is that diamonds are transparent, making the *in situ* pressure measurement possible.

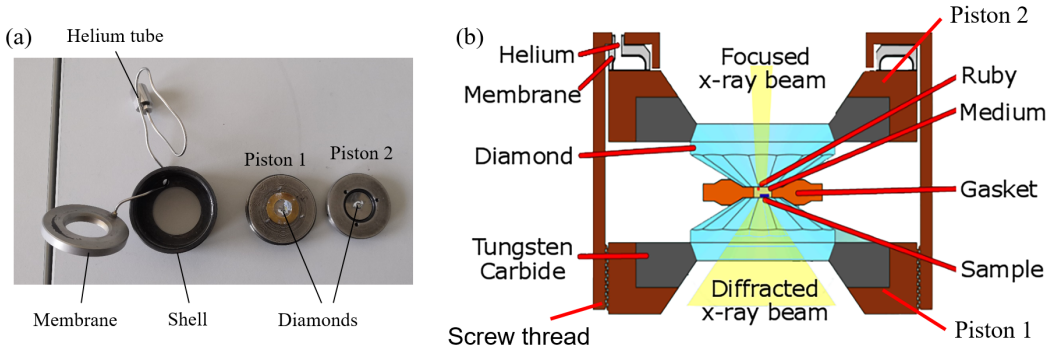

Figure 3.17: Diamond anvil cell. (a) Picture of the main components of a DAC. (b) Schematic diagram of the diamond anvil cell [180].

Figure 3.17 shows the main components and a scheme of a DAC. The sample loading procedure is simple: a gasket with a hole is first placed on the diamond of piston 1. Then, the sample, the pressure indicator (ruby) and the pressure medium (4 : 1 ethanol-methanol) are placed inside the hole. At last, the cell is closed by piston 2 and screwed into the shell. Piston 1 is well fixed with the shell, while piston 2 is movable by the membrane. By injecting helium, piston 2 will compress the hole, thus, increasing the pressure.

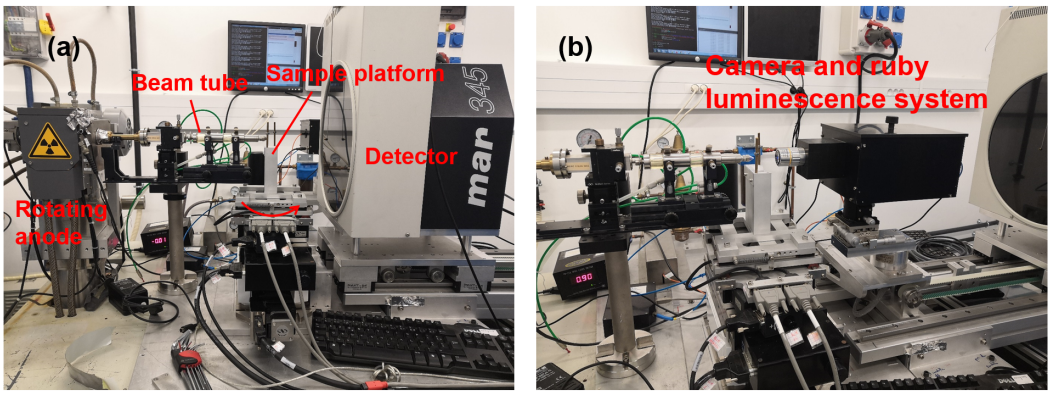

Figure 3.18: High pressure X-ray diffractometer. (a) Main components of the diffractometer. (b) The camera and ruby luminescence system are turned in front of the beam.

Powder X-ray diffraction experiments under pressure were carried out in our laboratory. The main components of the set-up are shown in Figure 3.18. A molybdenum X-ray rotating anode is used and the Mo-K_α emission line (0.71 Å) is selected by a low divergence optics monochromator. The reflection data are collected by a 2D Mar345 detector. The pressure cell is mounted on the sample platform. Besides, this set-up is also able to perform a single-crystal measurement under pressure since the platform can be rotated between ($-30°$) and ($30°$). The pressure inside the cell is measured by the fluorescent intensity of the ruby inside the cell. As shown in Figure 3.18(b), the ruby luminescence system is placed in front of the cell, allowing the measurement of the *in situ* increase of the pressure.

3.5 Neutron Diffraction

Another particle used to probe the properties of matter is neutron. Similar to X-rays, a neutron beam can detect the structural information of materials since its wavelength is comparable with the interatomic space in solids and liquids. However, neutrons also have some unique advantages:

- Neutrons interact with the atomic nucleus via the strong nuclear force, while X-rays interact with the electrons via an electromagnetic interaction. Therefore, the response of neutrons from light atoms is much higher than that of X-rays. Besides, neutrons can also distinguish isotopes while X-rays cannot. A comparison of the scattering lengths of some elements and isotopes for X-rays and neutrons is shown in Figure 3.19.

- For the same wavelength as X-rays, the neutron energy is much lower and comparable to the energy of elementary excitations in the matter. ($E_X[\mathrm{keV}] = 12.4/\lambda[\text{Å}], E_N[\mathrm{meV}] = 81.81/(\lambda[\text{Å}])^2$, where E_X and E_N are the energies of X-ray and neutron, respectively.) Therefore, neutrons allow not only the determination of the static atomic structure but also the investigation of the dynamic properties of atomic arrangements.

- The neutron has a large penetration depth and therefore the bulk properties of matter can be studied. Besides, the large penetration depth can benefit the investigation of materials under extreme conditions such as low/high temperatures, high pressures, high magnetic and electric fields since these experiments all require shields which prevent the application of X-rays.

- The neutron also carries a magnetic moment which can interact with the spins of electrons. This makes neutrons an excellent probe to determine the magnetic properties of matter, such as magnetic ordering, magnetic excitations, and spin fluctuations.

However, the application of neutron scattering is limited by the difficulty of production. Besides, since neutrons interact with nuclei, which are 10^5 times smaller than atoms, the required collection time in the neutron experiments is longer than that in the X-ray experiments. For the same reason, the sample used in neutron scattering is also larger. Table 3.5 gives some advantages and disadvantages of X-ray and neutron scattering.

3.5.1 Neutron Production

The neutron was first discovered by James Chadwick in 1932 [181]. The conventional way to produce neutrons is the nuclear fission reactor which relies on the chain reaction of the fission process

$$^{235}U + n \rightarrow D_1 + D_2 + 2.4n + Q, \tag{3.27}$$

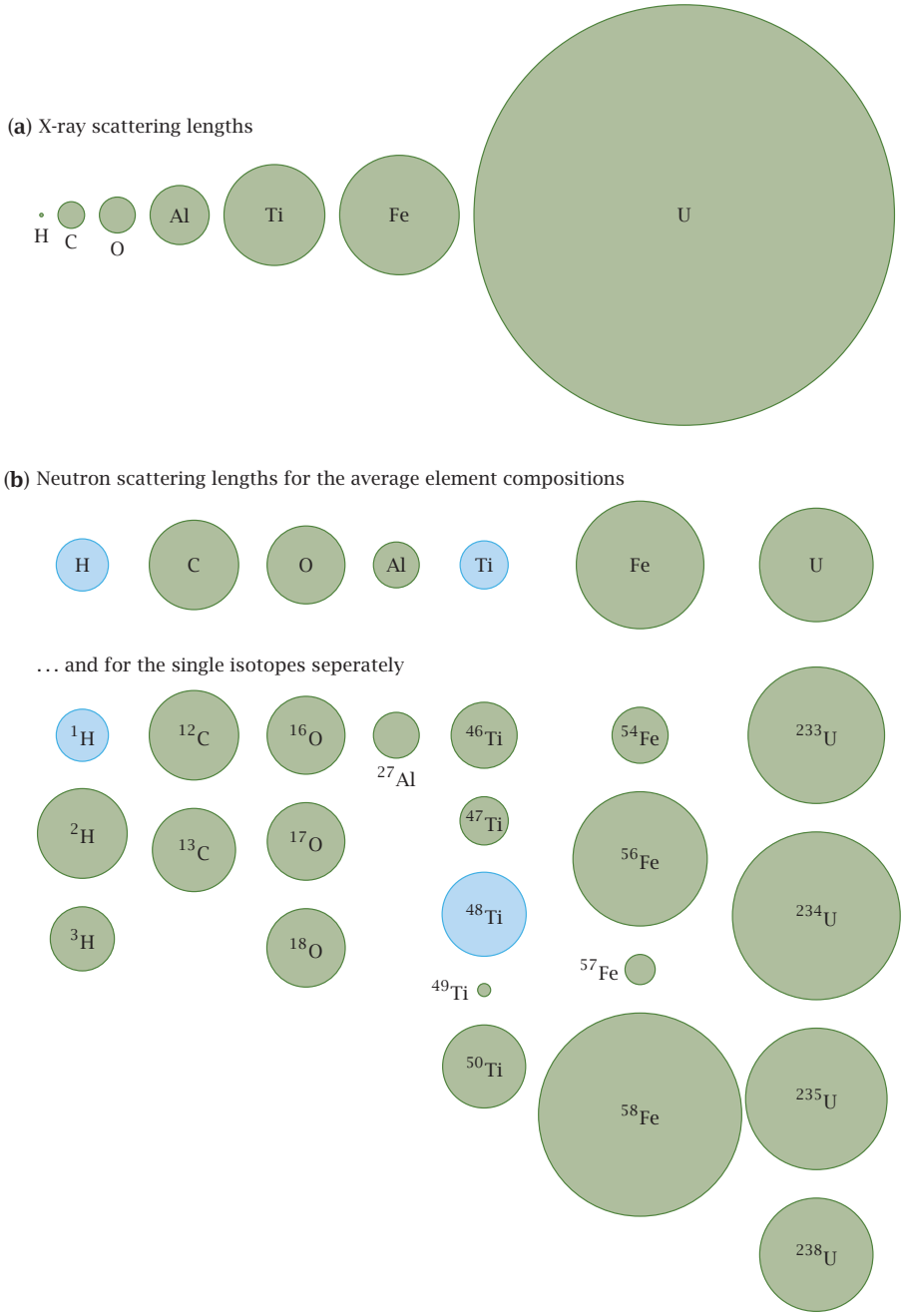

Figure 3.19: Illustration of the scattering lengths for some elements and isotopes with (a) 100 keV X-ray and (b) thermal neutron. Values are proportional to the diameters and the blue colour indicates a negative value. Figure from [91].

Table 3.5: The advantages and disadvantages of X-ray and neutron scattering.

	X-rays	Neutrons
Light elements visible	No	Yes
Distinguish isotopes	No	Yes
Dynamic properties	No	Yes
Magnetic properties	No	Yes
Easy to produce	Yes	No
Measuring time	Short	Long
Required sample size	Small	Big

where the daughter nuclei D_1 and D_2 can be a range of elements, and the released energy Q is of the order of 200 MeV. The average number of neutrons (n) produced by this reaction is 2.4 [182]. Most of the neutron reactors yield a continuous flux. The most powerful neutron source of this kind is located at Institut Laue Langevin (ILL) with a power of 58.3 MW. Besides, fission reactors also produce pulsed neutron beams such as the IBR-2 Pulsed Reactor in Dubna, Russia, with a power of 1850 MW in pulse. However, the limitation of the cooling system prevents the development of higher flux reactors.

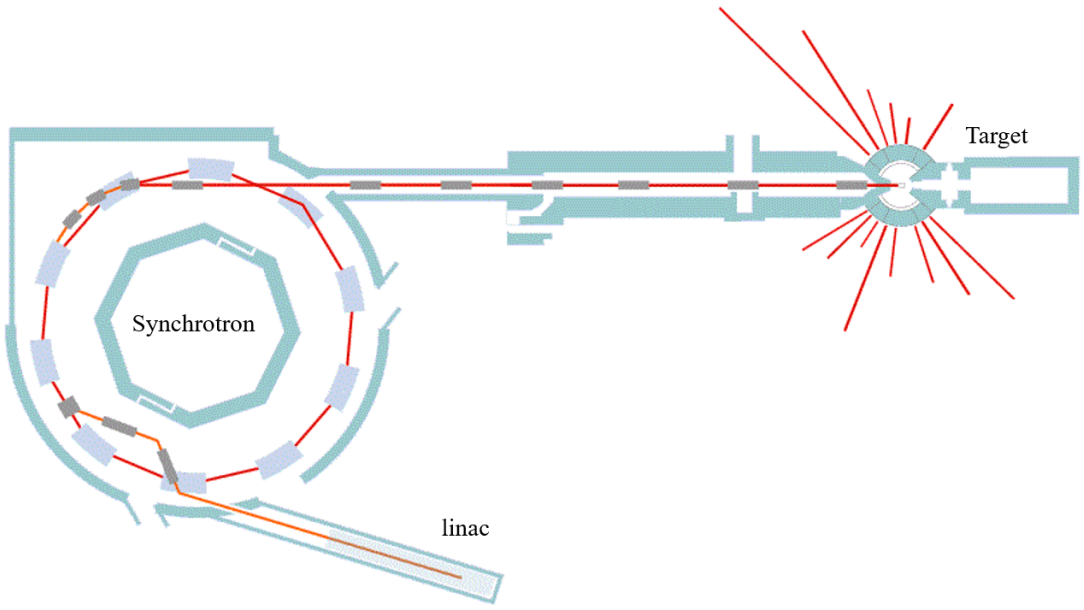

Figure 3.20: Schematic illustration of a spallation neutron source.

Another way to produce neutrons is the spallation source which yields pulsed neutron beams with high flux[2]. Figure 3.20 shows the schematic illustration of a spallation neutron source. Modern spallation sources are usually based on a linear accelerator (linac). A supply of charged heavy particles, typically H^- ions, are accelerated by the linac and fired through a thin carbon sieve which strips off the electrons and produces a proton beam. The protons are then fed into a compressor ring (synchrotron) which collects the protons from a large number of successive bunches fired out of the linac into a single very high intensity proton pulse. After the accumulation of sufficient intensity, the full proton pulse is extracted and propelled towards a target. Generally, the target can be made from mercury (Hg),

[2]Expect the Swiss Spallation Neutron Source (SINQ) which is a continuous source

tungsten (W), or uranium (U). Collision of the proton beam into the nuclei of the target results in a spallation process, which produces two or three smaller nuclei and several (~ 20) neutrons. At last, the yielded neutrons are sent to the surrounding neutron apparatus. The whole process occurs with a pulse repetition i.e., the neutron beam is not continuous as in the fission reactor.

3.5.2 Neutron Diffraction Instruments

In this thesis, three neutron diffraction instruments were used: G4.1 at Laboratoire Léon Brillouin (LLB), D1B and D23 at Institut Laue-Langevin (ILL). All three instruments are the two-axis diffractometers in which the first axis controls the wavelength of the incident beam by a monochromator and the second axis controls the scattering angle by rotating the sample. G4.1 and D1B are powder diffractometers, while D23 is devoted to the study of single crystals.

G4.1[3]: The general layout of G4.1 is shown in Figure 3.21(a). An 800-cells multidetector with a 2θ range of 80° is used to measure the intensity of the scattered beam. The wavelength of the incident beam (λ = 2.43 Å) is selected by a vertical focusing pyrolytic graphite monochromator. In this thesis, G4.1 was used to perform powder neutron diffraction experiments between 1.5 and 300 K at ambient pressure. The patterns are collected between 2θ = 2° and 82°.

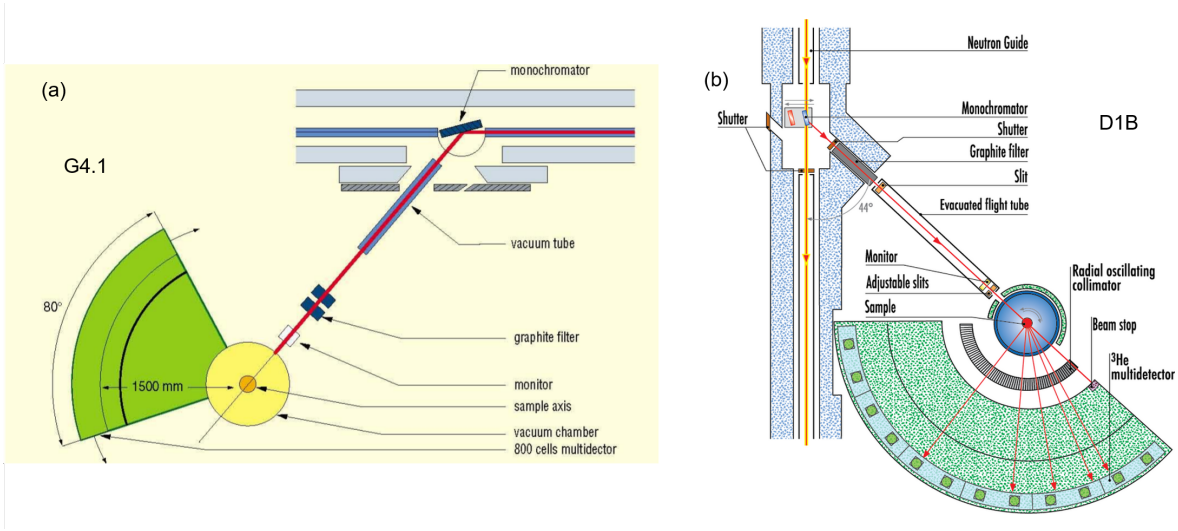

Figure 3.21: (a) Layout of the neutron two-axis diffractometer G4.1. (b) Layout of the neutron two-axis diffractometer D1B.

D1B[4]: Compared to G4.1, the Position Sensitive Detector (PSD) of D1B covers a larger angle (2° − 130°) with 1280 cells [Fig. 3.21(b)]. The wavelength is selected to be λ = 2.52 Å. We performed powder neutron diffraction experiments under pressure on D1B with a Paris-Edinburgh pressure cell. The schematic illustration of the pressure cell is shown in Figure 3.22. The mixture 4:1 methanol-ethanol was used as a transmitting medium and a maximum pressure of 11.7 GPa was reached. For the pressure determination, a small amount of Lead (Pb) was placed inside the anvil cell. The pressure can be obtained according to the lattice parameters of Pb by its equation of state (EOS) [183].

D23[5]: This two-axis diffractometer is equipped with a lifting-detector and uses thermal neutrons with a incident wavelength range of 1 Å < λ < 3 Å. Figure 3.23 shows its layout. A graphite (PG) or copper (Cu) monochromator is used for different wavelengths. The sample rotation is controlled by

[3] https://www-llb.cea.fr/fr-en/pdf/g41-llb.pdf
[4] https://www.ill.eu/users/instruments/instruments-list/d1b/description/instrument-layout
[5] www.ill.eu/users/instruments/instruments-list/d23/description/instrument-layout

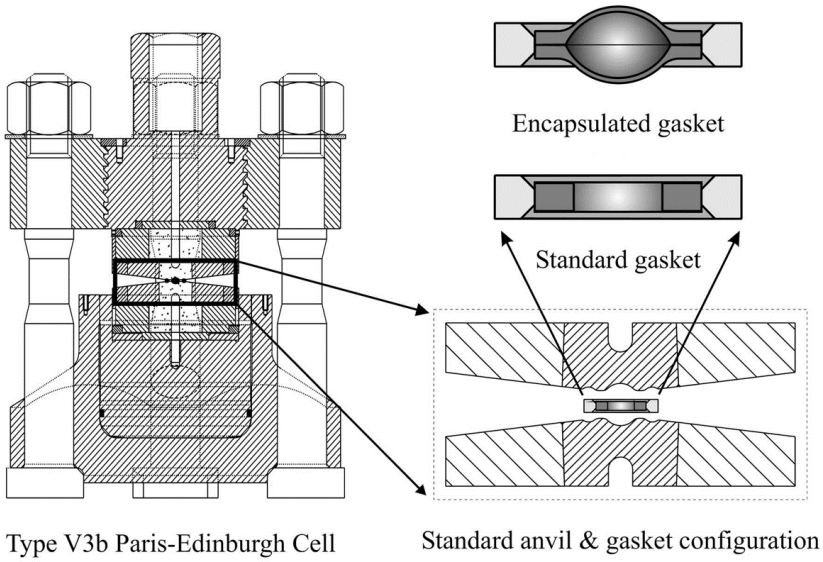

Figure 3.22: schematic illustration of Paris-Edinburgh pressure cell [184].

the angle ω. The 1D ^{3}He gas mono-detector is mounted in an arc, and thus can cover a symmetric angular range $\nu = \pm 30°$ above and below the horizontal plane. Besides, it can also be rotated by the angle γ ($\pm 130°$) in the horizontal plane. In this thesis, we preformed single-crystal neutron diffraction measurements at low temperature on D23.

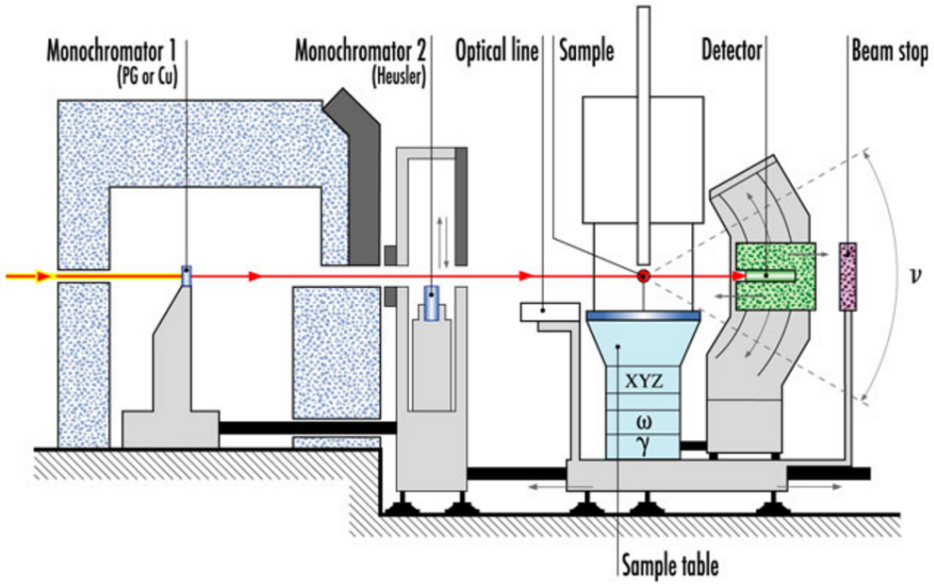

Figure 3.23: Layout of the single-crystal neutron diffractometer D23..

3.6 Data Analysis Tools

3.6.1 CrysAlis^{Pro}

The CrysAlis^{Pro}[6] is a collection and processing software for the single-crystal X-ray diffraction experiments developed by the Agilent Technologies (UK Ltd). It simplifies the interaction with the diffractometer hardware. Figure 3.24(top) shows its interface with a typical diffraction image of a single crystal. The reciprocal space can be reconstructed from the recorded images by CrysAlis^{Pro} [Fig. 3.24(bottom)]. The crystallographic quality of the samples is attested by the perfectly isolated and thin Bragg peaks. Therefore, the lattice parameters can be easily obtained.

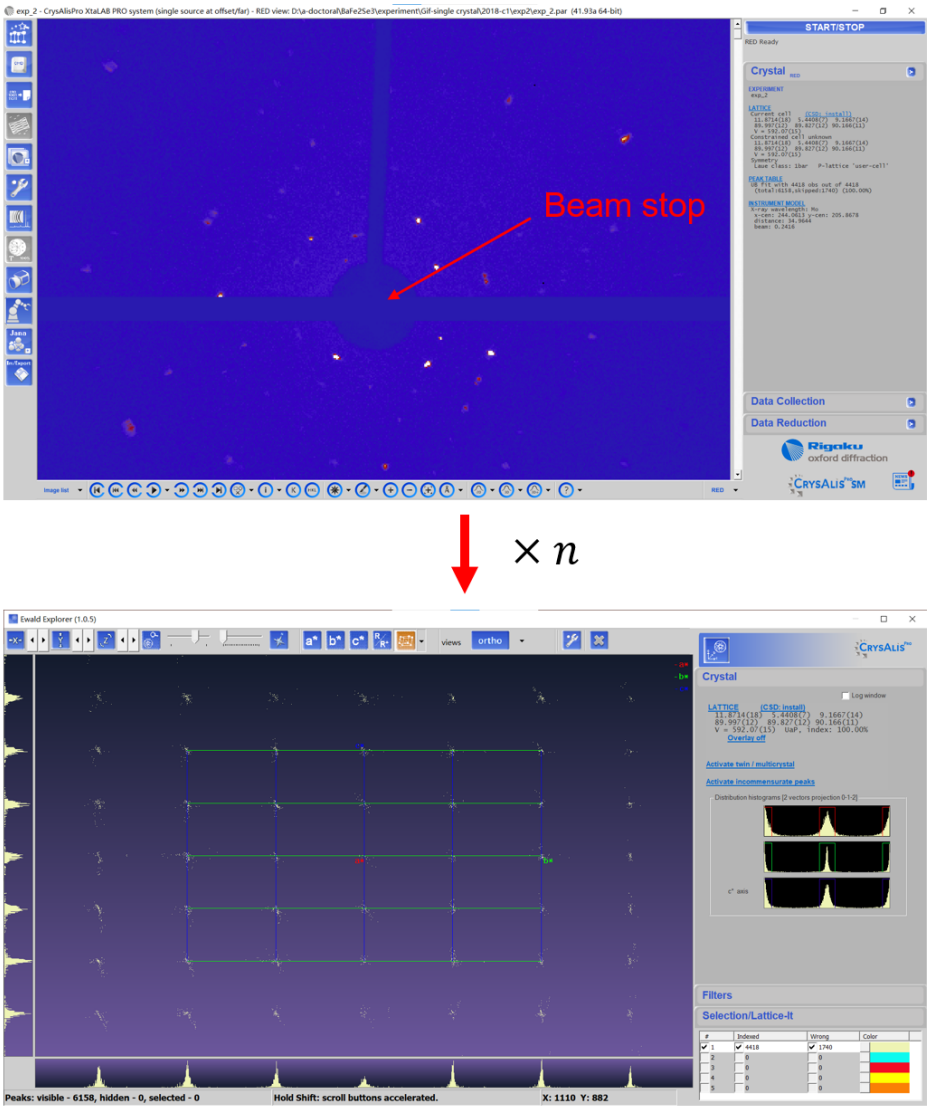

Figure 3.24: (Top) Interface of CrysAlis^{Pro} with a single-crystal diffraction image. (Bottom) Reciprocal space produced by CrysAlis^{Pro}.

[6] https://www.rigaku.com/products/crystallography/crysalis

3.6.2 Dioptas

The Dioptas[7] program is devoted to the fast integration and exploration of 2D X-ray diffraction images. It has three different modules (Calibration, Mask, Integration) as shown in Figure 3.25. The Calibration module allows the calibration of the detector geometry [Fig. 3.25(top)]. Besides, we can select the regions we want to exclude in the image integration in the Mask module [Fig. 3.25(middle)]. Finally, the integrated pattern is shown in the Integration module [Fig. 3.25(bottom)].

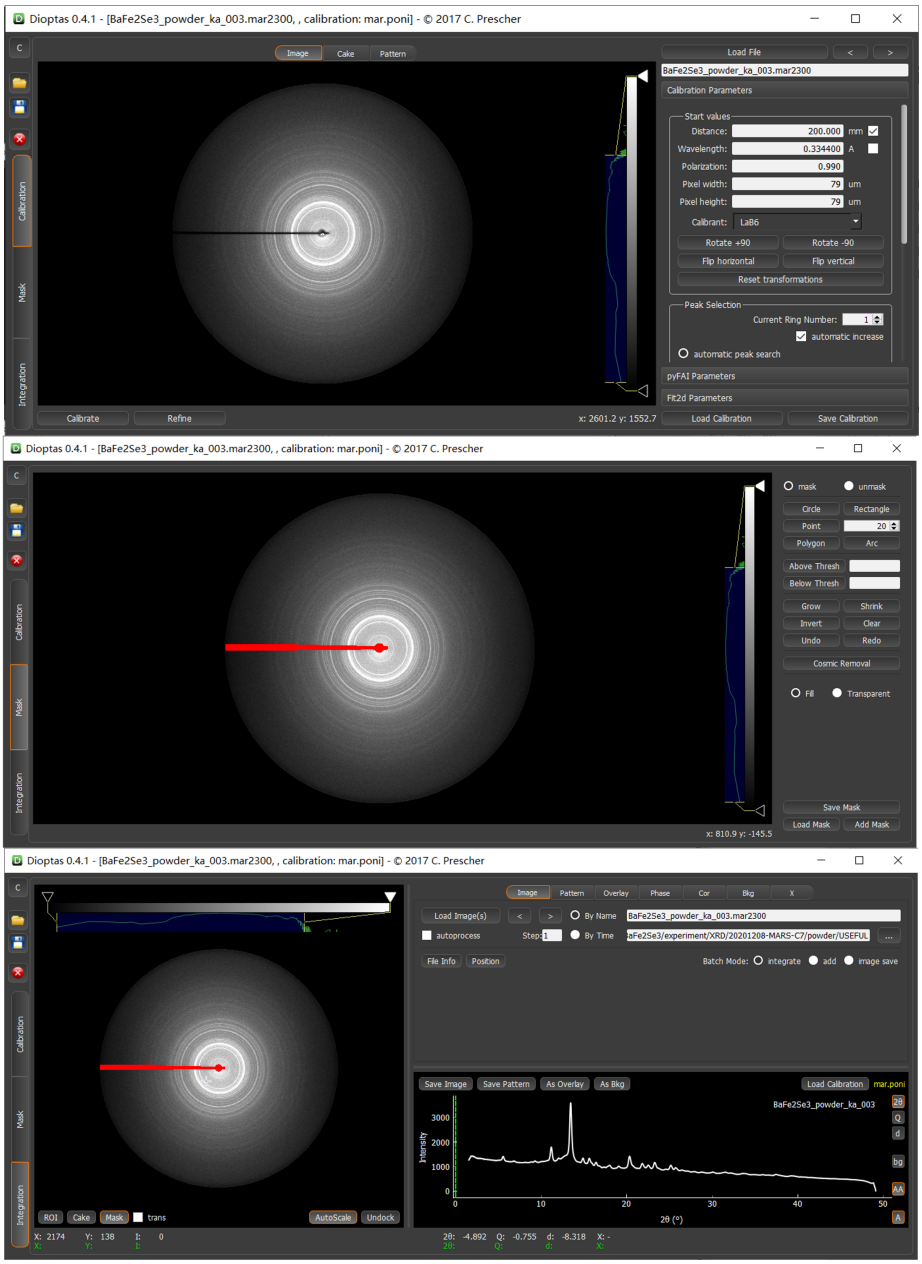

Figure 3.25: The Calibration (top), Mask (middle), Integration (bottom) modules of Dioptas. The integrated pattern is shown in the right of the bottom figure.

[7] https://dioptas.readthedocs.io/en/stable/index.html

3.6.3 FullProf Suite

The FullProf Suite[8] consists of a set of crystallographic programs (EdPCR, FullProf, WinPLOTR, FPStudio, etc.) mainly developed for Rietveld analysis of X-ray and neutron diffraction data. Figure 3.26 shows its toolbar, which displays all the programs. This Suite is capable of the structure refinements of both powder and single-crystal data. Moreover, both the nuclear and magnetic phases can be considered in the refinement. A PCR file including the structural information and refinement options and a data file including the experimental data are required for the refinement using FullProf. In this thesis, we mainly used it to refine the powder diffraction patterns, particularly the patterns under pressure in Chapter 5.

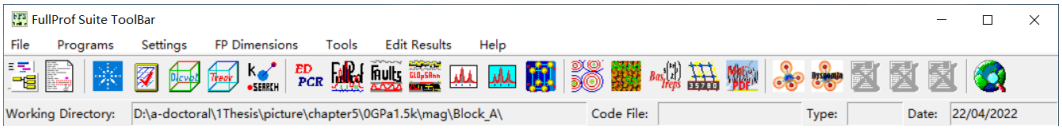

Figure 3.26: FullProf Suite ToolBar.

The quality of the agreement between observed and calculated profiles is measured by a set of factors. In this thesis, we always present the Bragg R-factor which is defined as following:

$$R_B = \frac{\sum_{\mathbf{h}} \left| I_{obs,\mathbf{h}} - I_{calc,\mathbf{h}} \right|}{\sum_{\mathbf{h}} \left| I_{obs,\mathbf{h}} \right|} \times 100, \tag{3.28}$$

where **h** represents the reflections. Besides, the magnetic R-factor (R_M) is also defined as the one above but is applied to magnetic intensities.

The temperature factor in FullProf is given by the atomic displacement parameter (ADP) B defined as:

$$B = 8\pi^2 \left\langle u^2 \right\rangle, \tag{3.29}$$

which is measured in units of Å^2. Therefore, the W (3.23) in the Debye-Waller factor can be written as

$$W = B \left(\frac{sin\theta}{\lambda} \right)^2. \tag{3.30}$$

3.6.4 Jana2006

Jana2006[9], similar to FullProf, is a crystallographic program devoted to the refinement and interpretation of crystal and magnetic structures. It is also capable of the analysis of the powder and single-crystal data measured by X-rays or neutrons. Besides, it allows a space group test based on the single-crystal data, which gives the possible space groups for an unknown structure. Figure 3.27 shows the result of the space group test from a single-crystal experiment. 'obs/all' column shows the number of reflections, which should be systematically extinct for each space group. For example, $Pnmm$ has 'obs/all'=4/83, which means that 83 reflections in the data file should be absent, and four of them have the intensity larger than 3σ, thus, violating the rules for systematic absences. '$ave(I/sig(i))$' column lists the average ratio of I/σ. For $Pnmm$, the 83 theoretically absent reflections and the four violating the rules have the average I/σ = 0.831 and 4.670, respectively. The proper space group should display a large number of unobserved systematically absent reflections and reasonable low I/σ for reflections violating the extinction rules. Therefore, in the case of Figure 3.27, $Pnmm$ and $Pnm2_1$ are both acceptable. This technique will be used in Chapter 4.

[8] https://www.ill.eu/sites/fullprof/index.html
[9] http://jana.fzu.cz/

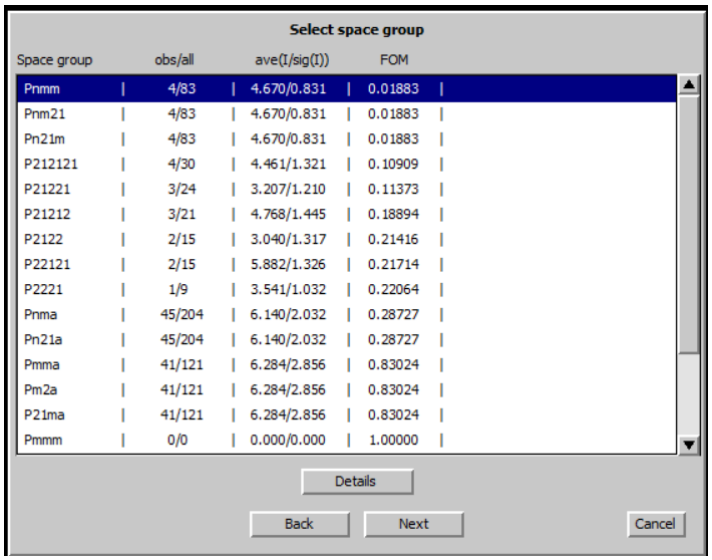

Figure 3.27: Results of a space group test, with the single-crystal diffraction data of $BaFe_2Se_3$ at 300 K, performed by JANA2006.

For the refinement using JANA2006, the reliability factors is given in the profile factor R and weighted profile factor wR. They are defined as:

$$R = \frac{\sum_{i=1}^{n} \left| y_i - y_{c,i} \right|}{\sum_{i=1}^{n} y_i} \times 100 \tag{3.31}$$

$$wR = \left[\frac{\sum_{i=1}^{n} w_i \left| y_i - y_{c,i} \right|^2}{\sum_{i=1}^{n} w_i y_i^2} \right]^{1/2} \times 100, \tag{3.32}$$

where n is the total number of points used in the refinement, and $w_i = 1/\sigma_i^2$, σ_1^2 being the variance of the observation y_i. Beside, the ADPs are given by U which can be easily converted from B by the relation of $U = B/8\pi^2 = \langle u^2 \rangle$. Moreover, it is quite common that anisotropic ADPs (U_{ij}) are applied. The relation between U and U_{ij} can be written as the following matrix:

$$U = \begin{pmatrix} U_{11} & U_{12} & U_{13} \\ U_{12} & U_{22} & U_{23} \\ U_{13} & U_{23} & U_{33} \end{pmatrix}. \tag{3.33}$$

The anisotropic ADPs will be used in Chapter 4

3.6.5 Bilbao Crystallographic Server

The Bilbao Crystallographic Server[10] is an open access website dedicated to solve the problems of structural and mathematical crystallography. It was initiated by the Materials Laboratory of the Department of Condensed Matter Physics at the University of the Basque Country (Bilbao, Spain). It offers various online crystallographic databases and programs which give general information related

[10] https://www.cryst.ehu.es/

to crystallographic symmetry groups. In this thesis, the SUBGROUPGRAPH program is used to plot the graph of the relationship between two given space groups in Chapter 4. Besides, the magnetic subgroup of a given space is obtained by the k-SUBGROUPSMAG program in Chapter 5.

3.7 Sample Synthesis and Characterization

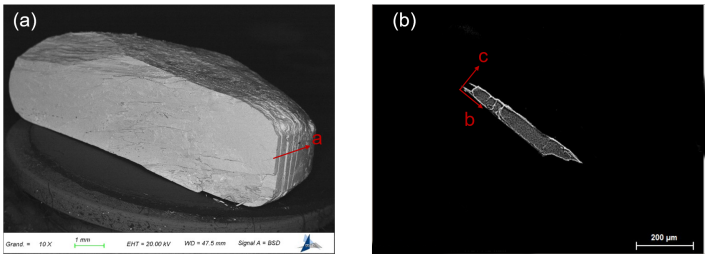

Figure 3.28: (a) SEM image of the $BaFe_2Se_3$ polycrystal. (a) SEM image of a single crystal of $BaFe_2Se_3$ after crashing.

The high purity $BaFe_2Se_3$ sample was synthesized by our collaborators Dorothée Dolson and Anne Forget from the Service de Physique de l'Etat Condensé (SPEC), using a melt-growth method from reference [134]. The typical growth procedure was as follows. The sample was heated at 1150 °C and melted for 24 h. The temperature was afterward lowered to 750 °C at a rate of 5 °C/h, then the furnace was cooled down to room temperature at 100 °C/h. A big polycrystal with a diameter of 10 mm was obtained. A plate geometry can be observed from the Scanning Electron Microscope (SEM) image [Fig. 3.28(a)]. The plate surface is normal to the a-axis [134]. We then crashed the polycrystal into smaller crystals in order to obtain single crystals. The small crystals have the shape of needles with a long edge along b-axis [Fig. 3.28(b)] [134]. In the polycrystal, the needles are roughly aligned. The samples from two batches (C1 and C5) were used in the present thesis.

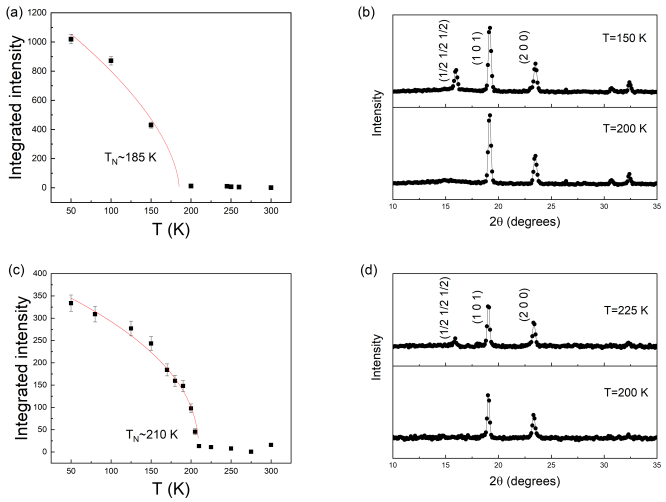

Figure 3.29: (a) and (c) Temperature dependence of the integrated intensity of the magnetic reflection $(\frac{1}{2}\frac{1}{2}\frac{1}{2})$ of C1 and C5. (b) and (d) Neutron powder diffractograms of C1 and C5 below and above T_N.

We performed the powder neutron diffraction at different temperatures for C1 and C5 on G4.1 LLB. The magnetic reflection $(\frac{1}{2}\frac{1}{2}\frac{1}{2})$ appears at low temperature [Figure 3.29 (b) and (d)]. Figure 3.29 (a) and (c) shows the temperature dependence of integrated intensity of $(\frac{1}{2}\frac{1}{2}\frac{1}{2})$ reflection for C1 and C5, respectively. The fitting curves (red lines) indicate that the Néel temperatures for C1 and C5 are 185 ± 10 K and 210 ± 10 K, respectively. These T_Ns are consistent with previous works showing a T_N

which spreads around 200 K [127, 144] and even in a larger domain from 140 K to 256 K [4, 128, 133, 134]. This large range of T_N is expected to be due to slight deviations from the ideal $BaFe_2Se_3$ stoichiometry [126].

The quality as well as the exact structure were checked by powder X-ray diffractions on the two-axis diffractometer of CRISTAL beamline. Figure 3.30 (a) shows the powder diffraction pattern of C5 at ambient condition refined with the structure of $BaFe_2Se_3$ from [3]. The R-factor is obtained as 1.39%. No additional phases were observed in our compound. By refining the occupancy parameters, we obtained for each element, occupancy rates close to the nominal ones within the uncertainties of 2-3%. Besides, the stoichiometries of our samples were checked by Energy Dispersive Spectroscopy (EDS). One of line scan spectra for C5 is shown in Figure 3.30(b). For the two batches used in this thesis, we obtained a maximum deviation 2% for the Fe and a maximum Se deficiency of 10% (depending on the position of the beam on the sample).

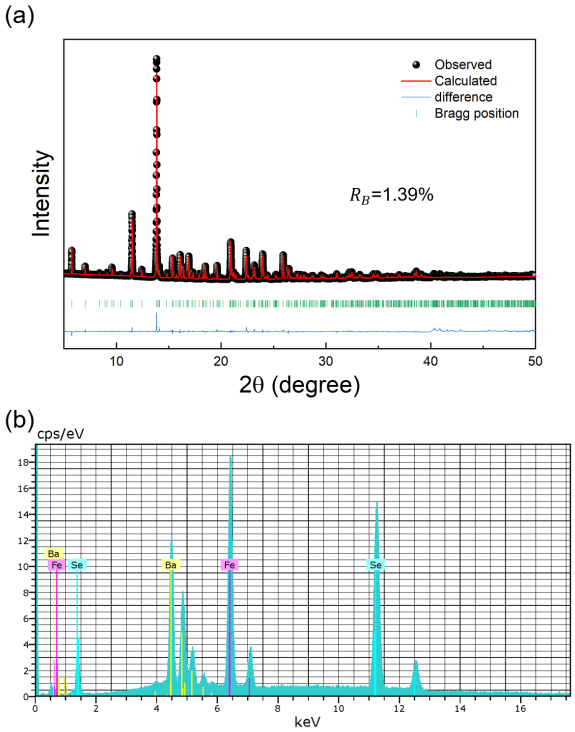

Figure 3.30: (a) Rietveld refinement of the powder diffraction pattern of $BaFe_2Se_3$ (C5) at ambient condition. (b) EDS line scan spectrum of $BaFe_2Se_3$.

In summary, all the physical properties of our compounds are similar to the published ones in various papers [4, 127, 128, 133, 134, 144]. We have indeed the same powder X-ray diffractogram and block-like magnetic order as previous references [4, 126, 133, 134]. So we are confident that the deviation from the exact Fe stoichiometry at the origin of the decrease of T_N in our samples does not strongly affect the crystal and magnetic structures, as well as other properties.

4

Room Temperature Polar Structure and Multiferroicity in $BaFe_2Se_3$

Contents

This chapter presents a single-crystal X-ray analysis on the crystal structure of $BaFe_2Se_3$. The non-polar *Pnma* space group, proposed in previous literature, is ruled out. We show that the system displays a polar structure already at 300 K and is thus ferroelectric. Furthermore, the crystal structure is modified below the Néel transition, which enhances the polarization. Besides, a magnetoelectric effect at 24 K is observed by the capacitance versus magnetic field measurement. These features unambiguously prove the multiferroic character of $BaFe_2Se_3$ as proposed theoretically [2]. The main results of this chapter have been published on Physical Review B: Rapid Communications [185].

4.1 Context and Motivation

An accurate description of atomic structure is essential to understand the properties of $BaFe_2Se_3$. However, the literature on this subject reports quite contradictory results. A powder neutron diffraction experiment shows that the magnetic transition does not break the high-temperature symmetry, and keeps the average space group *Pnma* below T_N [133]. Another study using powder neutron diffraction combined with neutron Pair Distribution Function (PDF) suggests that the *n* glide plane may be lost across the magnetic transition at a local scale, leading to a non-centrosymmetric space group $Pmc2_1$ below T_N [4]. Besides, an optical second harmonic generation (SHG) study evidences the absence of the inversion center and a preference of the space group $Pmn2_1$ below 400 K [130]. The lack of accurate atomic position and unambiguous space group determination above and below T_N prevents

further precise theoretical studies and experimental works. We thus used single-crystal X-ray diffraction experiments to reveal the actual polar structure. Our results unambiguously prove the multiferroic nature of this material below T_N.

4.2 Experimental Details and Data Analysis

We performed X-ray diffraction measurements at the Institut de Chimie des Substances Naturelles (ICSN) laboratory with Pascal Retailleau. We used a Rigaku XtaLabPro Kappa diffractometer with the Mo-K_α radiation emitted by a MM-003 microfocus sealed tube and equipped by a Dectris PILATUS3R-200K-A detector. The commercial software package CrysAlis^{Pro} was used to collect and analyse the diffraction data. The measurements were performed at 300 and 150 K. To exclude the possibility of sample dependence, two tiny single crystals from batch C1 and C5 with the size of $3 \times 2 \times 0.5$ mm^3 were tested. The quality of the batches have been characterized in Chapter 3, section 3.4. Hundreds of diffraction images were collected in step scans with a step of 1° during the rotation of the sample. Using CrysAlis^{Pro}, we can obtain the intensities of the collected reflections. 4280 and 2471 reflections were recorded at 150 and 300 K, respectively. With these reflection files, we can refine the structures at the two temperatures. The refinements were performed by the software package JANA2006 [186].

4.3 Space Group Analysis and Structure Refinements

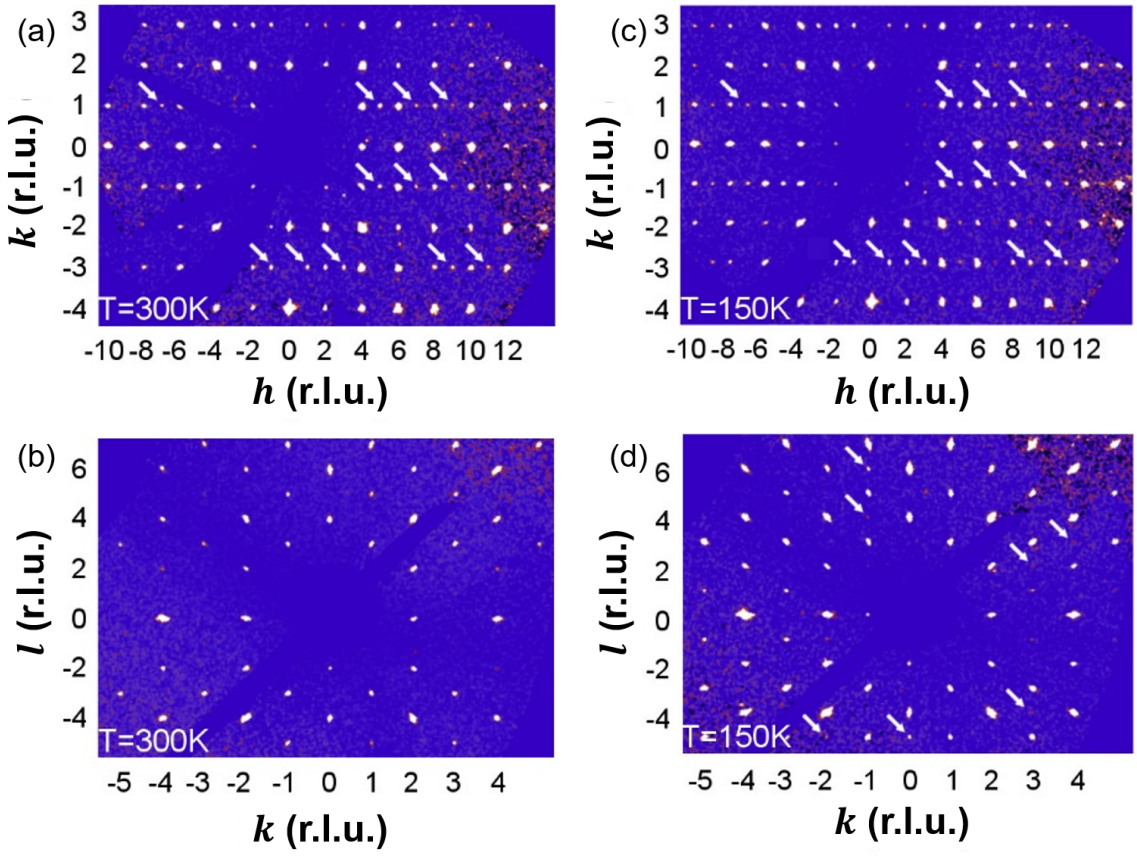

Figure 4.1: (a) and (b) Reconstructions of the lattice node planes $(hk0)$ and $(0kl)$ at 300 K, respectively. (c) and (d) Reconstructions of the lattice node planes $(hk0)$ and $(0kl)$ at 150 K, respectively. Arrows indicate the forbidden reflections associated with the a glide plane in (a) and (c), the n glide plane in (d).

As we mentioned in section 3.3.3, there are five reflection conditions for *Pnma*. The reflection conditions come from the symmetry operations of the space group. Their relationships are shown in Table 4.1. To check if the reflection conditions are well obeyed, we plotted the reconstructions of the reciprocal lattice node planes $(hk0)$ and $(0kl)$ at both 150 and 300 K, as shown in Figure 4.1.

Table 4.1: Relationships between reflection conditions and symmetry operations in *Pnma*.

Reflection conditions	$0kl$: $k+l=2n$	$hk0$: $h=2n$	$h00$: $h=2n$	$0k0$: $k=2n$	$00l$: $l=2n$
Symmetry operations	n glide plane $\perp a$	a glide plane $\perp c$	2_1 screw axis $\parallel a$	2_1 screw axis $\parallel b$	2_1 screw axis $\parallel c$

At 300 K, one can first observe that the reflections forbidden by the n glide plane are absent in Figure 4.1(b) as expected for the *Pnma* space group. However, the forbidden reflections associated with the a glide plane were systematically observed, indicated by the white arrows in Figure 4.1(a). We thus selected the forbidden reflections $(hk0 : h \neq 2n)$ over the 2471 recorded reflections. More than 40 forbidden reflections with $I > 3\sigma$ were detected (Table 4.2). The width of the forbidden reflections, measured in CrysAlis^{Pro}, is comparable to that of the allowed Bragg reflections. Therefore, we can exclude an origin related to an effect of the disorder. In addition, their average intensity was about 4% of the average intensity of the standard Bragg reflections. This corresponds to a strong symmetry breaking of the a plane. Furthermore, the forbidden reflections are observed both at low diffraction angles and at high angles, suggesting a displacive origin. In that case, the intensity of the forbidden reflections is expected to be proportional to the square of the atomic displacements, which here gives 0.2 Å. These displacements are much larger than the ones generally observed for structural transitions like the Peierls transitions in the blue bronze [187], or the Spin Peierls transition in $CuGeO_3$ [188].

Table 4.2: Reflections at 300 K which violate the reflection condition $hk0 : h = 2n$ induced by the a glide plane in *Pnma*.

Reflections			I	σ	Reflections			I	σ	Reflections			I	σ
-11	3	0	1532.74	162.06	-1	-2	0	274.85	82.439	5	2	0	418.07	148.96
-9	3	0	1959.36	302.61	-1	2	0	608.21	102.09	7	-1	0	1158.72	228.66
-7	-5	0	1407.87	301.48	-1	3	0	2314.95	219.22	7	1	0	1087.85	305.11
-7	-1	0	1370.46	296.77	-1	5	0	699.97	204.71	7	5	0	1370.02	378.04
-7	1	0	1186.76	323.89	1	-5	0	583.87	162.59	7	5	0	1431.78	141.50
-5	-5	0	4060.41	458.47	1	-3	0	2134.06	175.48	9	-3	0	2467.06	297.33
-5	-1	0	4411.24	311.38	1	-2	0	506.15	105.30	9	-1	0	798.25	260.57
-5	1	0	4194.60	436.92	1	3	0	2088.71	194.07	9	3	0	1860.88	453.18
-5	2	0	438.83	120.78	1	5	0	925.65	195.58	11	-3	0	1266.84	164.23
-5	5	0	3228.24	442.51	3	1	0	1418.6	319.35	11	-1	0	1299.90	183.741
-3	-3	0	2663.46	228.96	3	3	0	2852.54	320.70	11	1	0	1224.99	392.38
-3	7	0	1556.15	346.73	5	-2	0	436.55	123.24	11	3	0	1771.46	468.83
-1	-5	0	722.44	210.17	5	-1	0	5051.79	345.24	13	-1	0	1424.90	397.18
-1	-3	0	2007.71	216.56	5	1	0	4422.54	394.79	13	1	0	1381.627	134.18

Before going any further, we checked for possible experimental artifacts. We verified that neither a wavelength harmonic contamination $(\lambda/2)$ nor the twinning of the crystal could explain the presence of such forbidden reflections. The possibility of a multiple scattering effect was also ruled out since it could not affect only the reflections forbidden by the a glide plane. The observed forbidden reflections

thus cannot be associated with an experimental artifact. Moreover, since they are observed in two compounds from different batches, we can conclude that this superstructure is an intrinsic structural property of $BaFe_2Se_3$ at 300 K. It was not evidenced in previous structural works because these experiments were performed on powders [4, 133]. In our more accurate work, we used single-crystal X-ray measurements, which enabled us to detect very weak structural effects associated with the symmetry breaking observed.

At 150 K, below T_N, the forbidden reflections of the a glide plane are still present on the reconstructions and with the same average intensity [Fig. 4.1(c)]. Moreover, several reflections violating the condition $0kl : k + l = 2n$ emerged in Figure 4.1(d), indicating the absence of the n glide plane. Meanwhile, 15 additional forbidden reflections were recorded (Table 4.3). Their intensity is about 1% of the average intensity of the standard Bragg reflections. They also have the experimental resolution and behave as a displacive effect.

Table 4.3: Reflections at 150 K which violate the reflection condition $0kl : k + l = 2n$ induced by the n glide plane in $Pnma$.

Reflections			I	σ	Reflections			I	σ	Reflections			I	σ
0	1	2	24.79	4.62	0	-1	-6	65.93	11.11	0	5	6	44.69	8.48
0	1	-2	17.46	4.36	0	2	-3	26.64	7.035	0	-5	6	44.28	7.04
0	-1	2	17.95	5.49	0	2	-5	19.54	6.327	0	2	-3	53.16	4.51
0	1	-6	79.67	15.29	0	-2	9	47.81	8.375	0	-2	3	50.26	4.48
0	-1	6	59.47	10.6	0	5	-6	39.71	6.851	0	2	-5	41.11	3.96

We will first discuss the data at 300 K. In the light of our results, one can unambiguously assert that the space group cannot be $Pnma$ at 300 K. We thus made a space group test on the collected data by JANA2006. The results were already shown in Figure 3.27. As we can see, $Pnm2_1$ and $Pnmm$ are most compatible with the experimentally observed reflections. $Pnm2_1$ [$Pmn2_1$ (No.31) in the conventional setting] is the subgroup of $Pnma$ including the symmetry breaking of the a glide plane. On the other hand, $Pnmm$ [$Pmmn$ (No.59) in the standard setting] is the subgroup of $Cmcm$. Interestingly, $Cmcm$ is the space group expected above 600 K at ambient pressure or above a pressure of 6 GPa at ambient temperature [129, 131]. It is important to notice that in $Cmcm$, the two ladders of the unit cell are parallel and equivalent by translation. It is not the case in the $Pnma$ structure.

Table 4.4: Atomic structure of $BaFe_2Se_3$ at 300 K in the $Pmn2_1$ (No. 31) space group (R_{obs}=3.29%, wR_{obs}=6.41%). The lattice parameters are a_{o2} = 5.4435 Å, b_{o2} = 11.8717 Å, and c_{o2} = 9.1630 Å, $\alpha_{o2} = \beta_{o2} = \gamma_{o2} = 90°$. The number of reflections with $I > 3\sigma$ is 2471.

Atom	Site	x	y	z	U11	U22	U33	U12	U13	U23
Ba1_1	2a	0.5	0.43618(19)	-0.5209(3)	0.0196(8)	0.0331(13)	0.0317(19)	0	0	-0.0044(13)
Ba1_2	2a	0	0.06672(18)	0.5181(3)	0.0237(10)	0.0352(13)	0.037(2)	0	0	-0.0123(14)
Fe1_1	4b	0.2442(4)	0.7446(3)	-0.3496(7)	0.019(3)	0.018(2)	0.024(3)	-0.001(2)	0.0025(16)	0.0008(15)
Fe1_2	4b	0.2438(4)	-0.2436(3)	0.3528(7)	0.020(3)	0.020(2)	0.016(2)	0.0014(18)	-0.0014(16)	-0.0013(14)
Se1_1	2a	0.5	0.6111(3)	-0.2271(6)	0.0141(17)	0.027(2)	0.021(3)	0	0	0.0108(19)
Se1_2	2a	0	-0.1061(3)	0.2291(6)	0.0265(19)	0.023(2)	0.025(3)	0	0	0.008(2)
Se2_1	2a	0.5	0.8716(3)	-0.4902(6)	0.0194(13)	0.0116(13)	0.014(2)	0	0	0.0001(19)
Se2_2	2a	0	-0.3806(3)	0.4925(6)	0.0159(12)	0.0221(16)	0.024(3)	0	0	0.001(2)
Se3_1	2a	0.5	0.6515(3)	-0.8135(5)	0.0239(18)	0.029(2)	0.030(3)	0	0	-0.014(2)
Se3_2	2a	0	-0.1457(3)	0.8149(5)	0.0206(17)	0.031(2)	0.022(3)	0	0	-0.013(2)

We then refined the 300 K data obtained from the specimen of batch C5 in both space groups. The initial structures were transformed from the structures from references [4, 129] by the transformation

tool of JANA2006. For instance, the initial $Pmn2_1$ structure was transformed from the *Pnma* of reference [4] [Fig. 4.2]. Then, the atomic positions and anisotropic Debye-Waller temperature factors (U_{ij}) were refined. Finally, we obtained a R-factor of $R_{obs} \approx 3\%$ for $Pmn2_1$. The results are shown in Table 4.4. On the other hand, the refinement in the *Pmmn* space group leads to a poor reliability factor ($R_{obs} \approx 55\%$). The calculated structure factors are plotted against those observed for both space groups and shown in Figure 4.3. It is clear that the $Pmn2_1$ is the correct space group for $BaFe_2Se_3$, which is compatible with the SHG results [130].

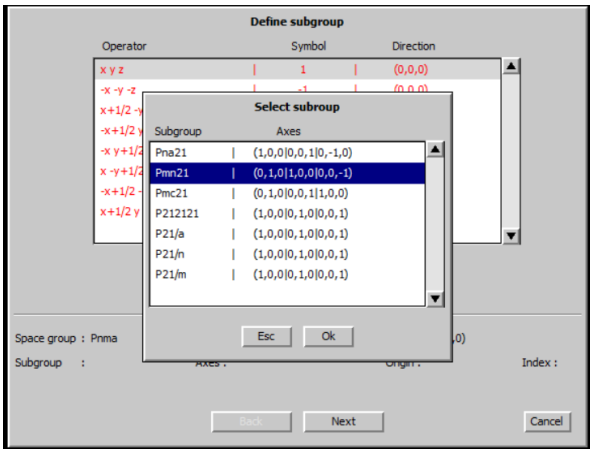

Figure 4.2: Transformation tool to subgroup of JANA2006. Here shows the maximal non-isomorphic subgroups of *Pnma*.

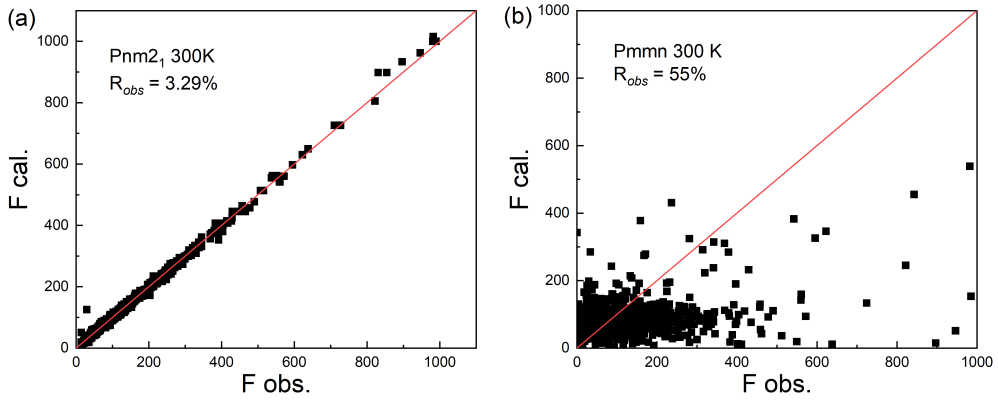

Figure 4.3: Structure factors of nuclear reflections collected at 300 K plotted versus the calculated values in $Pmn2_1$ (a) and *Pmmn* (b).

Then, we considered the 150 K structure, which describes the structure below the Néel transition and thus in the k=(0.5 0.5 0.5) magnetic phase. The apparition of reflections breaking the *n* glide plane implies that the $Pmn2_1$ space group is no more acceptable. The low-temperature structure seems to be affected by the magnetic ordering. The magnetic transition being second order, we expect a structure subgroup of $Pmn2_1$. The unique space group, compatible with all the experimentally observed reflections, is $Pm11$ [$P1m1$ (No. 6) in the standard setting, labeled *Pm* in the following]. *Pm* is monoclinic with unit cell parameters close to orthorhombic ones ($\beta \approx 90.05 \pm 0.05°$). We have refined the 150 K data, and the obtained structure is given in Table 4.5.

Figure 4.4 shows the possible inter-relations between *Pnma* and *Pm* obtained by the SUBGROUP-GRAPH of the Bilbao Crystallographic Server [189]. As we can see, the shortest group-subgroup chain between them is of index 4 and can be realized via the subgroup $Pmn2_1$. The unit cells of the three space group and the transformation matrices between them are shown in Figure 4.5. The *Pnma*

Table 4.5: Atomic structure of $BaFe_2Se_3$ at 150 K in the *Pm* (No. 6) space group (R_{obs}=3.00%, wR_{obs}=3.48%). The lattice parameters are a_{m1} = 9.1496 Å b_{m1} = 5.4289 Å and c_{m1} = 11.8673 Å β_{m1} = 90.03, $\alpha_{m1} = \gamma_{m1} = 90°$. The number of reflections with $I > 3\sigma$ is 4280.

Atom	Site	x	y	z	U11	U22	U33	U12	U13	U23
Ba1_1_1	1b	-0.5234(3)	0.5	0.4377(2)	0.0057(11)	0.0075(10)	0.0115(15)	0	-0.0048(15)	0
Ba1_1_2	1a	-0.0219(3)	0	-0.4356(2)	0.0181(15)	0.0094(10)	0.0100(14)	0	0.0033(17)	0
Ba1_2_1	1a	0.5235(3)	0	0.0639(2)	0.0173(14)	0.0128(11)	0.0069(15)	0	0.0013(15)	0
Ba1_2_2	1b	1.0211(3)	0.5	-0.0688(2)	0.0254(18)	0.0049(10)	0.026(2)	0	0.0181(18)	0
Fe1_1_1	2c	-0.3512(6)	0.2447(6)	0.7437(4)	0.011(3)	0.018(2)	-0.006(2)	0.0019(19)	-0.001(2)	0.000(2)
Fe1_1_2	2c	0.1464(6)	0.7404(5)	-0.7446(5)	0.011(2)	0.0068(16)	0.015(2)	0.0023(17)	0.002(2)	0.003(2)
Fe1_2_1	2c	0.3506(5)	0.2484(5)	-0.2402(4)	0.005(2)	-0.0007(15)	0.007(2)	0.0005(15)	0.005(2)	0.0023(15)
Fe1_2_2	2c	0.8523(6)	0.7359(5)	0.2467(4)	0.006(2)	0.0083(15)	0.006(2)	-0.0052(17)	0.0015(19)	0.0048(17)
Se1_1_1	1b	-0.2291(5)	0.5	0.6093(4)	0.004(2)	0.0034(18)	0.014(3)	0	0.004(3)	0
Se1_1_2	1a	0.2688(5)	0	-0.6092(4)	0.0017(18)	0.010(2)	0.011(3)	0	-0.009(2)	0
Se1_2_1	1a	0.2296(5)	0	-0.1024(3)	0.010(2)	0.012(2)	-0.003(2)	0	0.0089(19)	0
Se1_2_2	1b	0.7322(5)	0.5	0.1048(4)	0.018(2)	0.004(2)	0.007(2)	0	0.006(2)	0
Se2_1_1	1b	-0.4906(5)	0.5	0.8717(4)	0.006(2)	0.0054(18)	0.010(3)	0	0.007(2)	0
Se2_1_2	1a	0.0068(6)	0	-0.8720(4)	0.015(2)	0.0073(18)	-0.005(2)	0	0.005(2)	0
Se2_2_1	1a	0.4893(6)	0	-0.3796(4)	0.001(2)	0.0046(18)	0.015(3)	0	-0.010(3)	0
Se2_2_2	1b	0.9890(5)	0.5	0.3825(4)	0.0038(19)	0.0078(18)	0.004(2)	0	-0.007(2)	0
Se3_1_1	1b	-0.8143(4)	0.5	0.6525(4)	0.002(2)	0.0038(16)	0.009(2)	0	-0.007(2)	0
Se3_1_2	1a	-0.3149(5)	0	-0.6528(4)	0.015(3)	0.016(2)	0.016(3)	0	0.006(2)	0
Se3_2_1	1a	0.8167(4)	0	-0.1489(4)	0.015(2)	0.0046(16)	0.003(2)	0	-0.004(2)	0
Se3_2_2	1b	1.3192(5)	0.5	0.1483(5)	0.009(2)	0.0107(16)	0.014(2)	0	0.010(2)	0

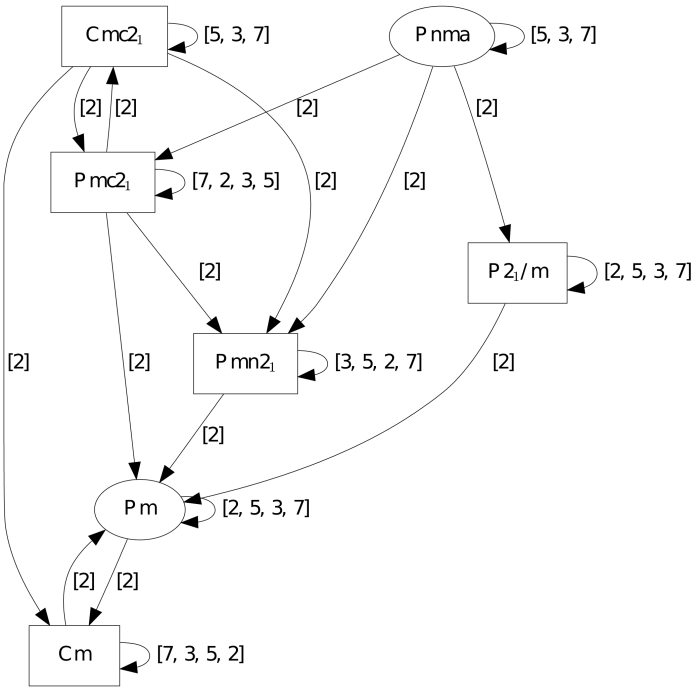

Figure 4.4: Group-Subgroup graph from *Pnma* to *Pm*.

structure is from reference [4] and the other two are from our results.

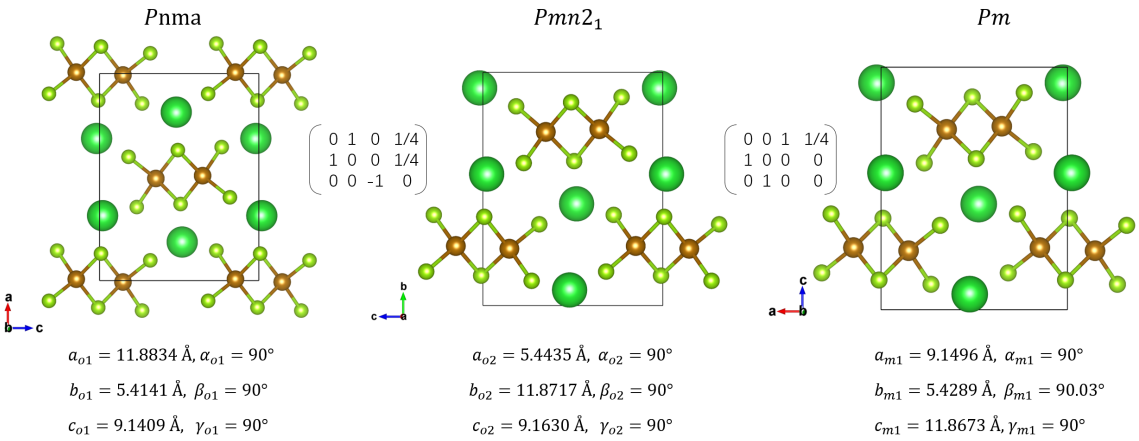

Figure 4.5: The unit cells of $BaFe_2Se_3$ in *Pnma*, $Pmn2_1$, and *Pm* and transformation matrices between them. The subscript *o* indicates the orthorhombic cell and *m* for the monoclinic cell.

As mentioned in Chapter 2, Dong et al. proposed that a net polarization in $BaFe_2Se_3$ occurs due to the tetramerization of the Fe ladders along the *b*-axis [2]. However, in *Pnma*, the blocks of the ladders are identical as shown in Figure 4.6(top). This is not compatible with the tetramerization of Fe blocks in [2] and prevents the emergence of a net electric polarization. On the contrary, in the $Pmn2_1$ space group, a displacement of Fe atoms is allowed by the absence of the inversion centers [indicated by the red arrows in Figure 4.6(middle)]. Besides, the two ladders of the unit cell are symmetry equivalent by the *n* glide plane and the 2_1 screw axis. Consequently, there are four different Fe-Fe distances (2.785 Å, 2.659 Å, 2.789 Å, and 2.655 Å) in our structure while two very close Fe-Fe distances (2.72 ±0.01 Å) were observed in previous works [3, 133]. Hence, the tetramerization of the ladders in $Pmn2_1$ is much stronger than that for the structures previously published. The difference of Fe-Fe distances along the chains reaches 0.13 ±0.05 Å in our refinement while it is ten times smaller (0.007 Å and 0.014 Å respectively) in the structures of [3] and [133]. Moreover, a recent neutron experiment using a PDF analysis also evidenced a strong difference in Fe-Fe distances (0.2 Å) [156].

As for the *Pm* space group, eight different Fe-Fe distances were observed since the ladders are no more equivalent by symmetry [Fig. 4.6(bottom)]. The tetramerization now strongly differs between the two ladders of the unit cell (a mean tetramerization of 0.25 ±0.03 Å for one ladder and 0.07 ±0.04 Å for the other). This is compatible with a recent STEM measurement in which different distortions for the two ladders were also observed [154]. Besides, this STEM measurement proposed that the *Pm* structure persists up to 610 K. Meanwhile, a structural dynamics study also confirmed that the space group of $BaFe_2Se_3$ is *Pm* both in the magnetic and paramagnetic phases [190]. The short-short-long-long rectangular configuration of the ladders is proved to be originated from the block spin order by the *ab initio*-experiment phonon study [190].

4.4 Polarization in $BaFe_2Se_3$

Based on the $Pmn2_1$ and *Pm* experimental structures we roughly evaluated the associated polarization using a simple ionic summation of Ba^{2+}, Fe^{2+} and Se^{2-} ions. Of course, a correct calculation should be done using a Berry phase approach within a DFT calculation. However, such an easy procedure provides an order of magnitude. For the $Pmn2_1$ group, we used the closest *Pnma* non-polar structure as a reference. Under these conditions, we found an expected electric polarization of 0.08 $\mu C/cm^2$ along the rung direction for the $Pmn2_1$ structure at 300 K. This value is comparable to the electric polarization of improper multiferroics such as RMn_2O_5 [191]. It is also close to the amplitude of

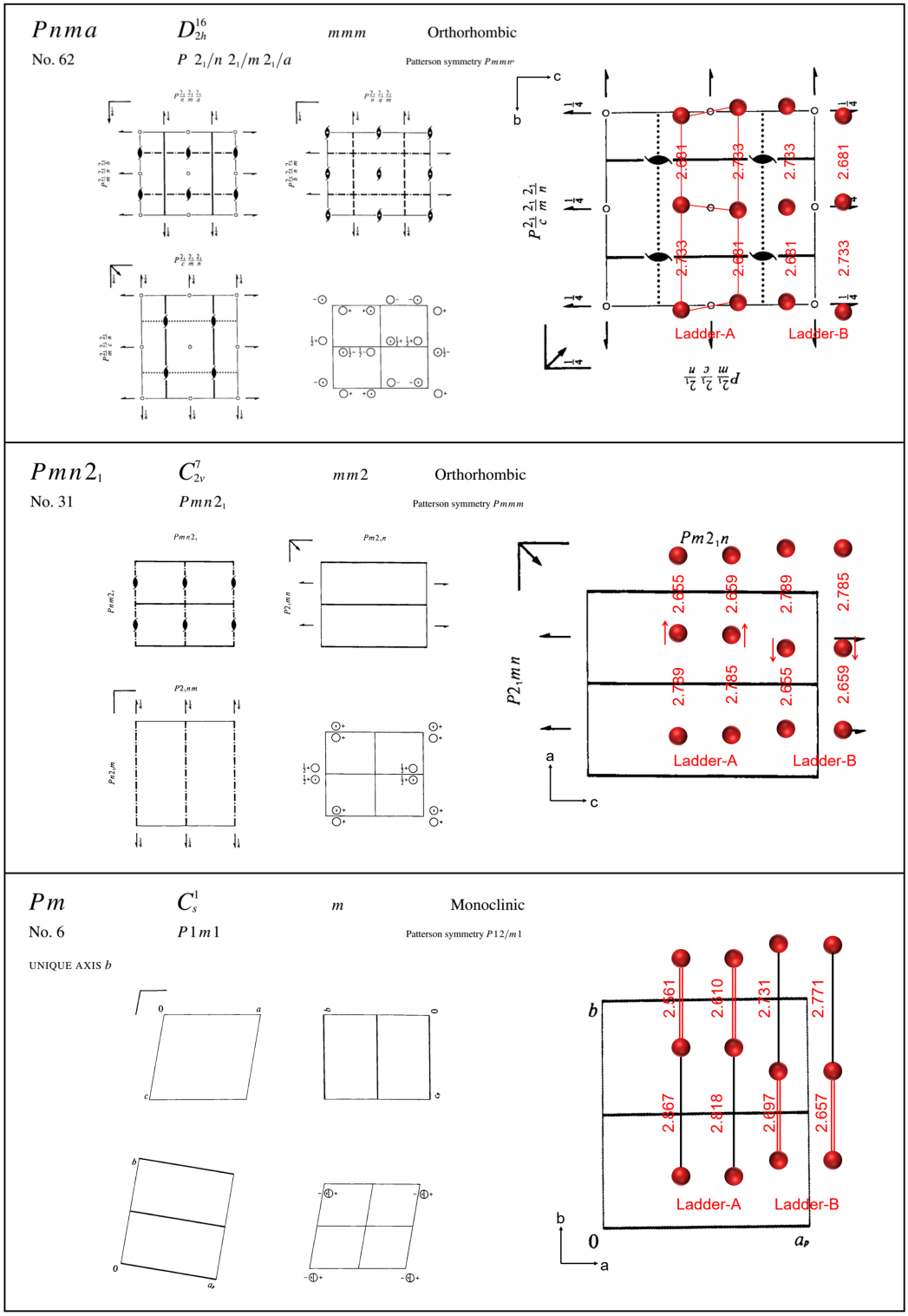

Figure 4.6: Diagrams for the symmetry elements and the general position of *Pnma* (top), $Pmn2_1$ (middle), and *Pm* (bottom) [173]. The two ladders in one unit cell are shown with the corresponding diagram for the three space groups. The *Pnma* structure is extracted from reference [4] while $Pmn2_1$ and *Pm* are based on our results. In *Pnma*, the two Fe-blocks (indicated by the solid red lines) of the ladder have the same Fe-Fe distances due to the inversion centers. In $Pmn2_1$, the absence of inversion centers allows a Fe displacement towards one direction (indicated by the red arrows). Therefore, a large difference in Fe-Fe distance between the two Fe-blocks along the chain is induced. In *Pm*, since the 2_1 screw axis is absent, eight different Fe-Fe distances are observed. The red double-lines indicate the short Fe-Fe bonds while the black lines indicate the long ones.

polarization along the rung direction in the magnetic phase proposed by reference (0.19 μC/cm^2) [2]. However, in this work, the authors predict the electric polarization to be due to magnetostrictive effects. We show here that the electric polarization is already present at ambient temperature in the paramagnetic phase and cannot be ascribed to a magneto-electric mechanism.

The same calculation of the electric polarization performed in the magnetic phase at 150 K corresponding to the Pm structure. The $P2_1/m$ non-polar structure was used as a reference. One should notice that the symmetry of Pm imposes the polarization to be in the (a, c) plane (in the Pm setting). We obtained $P_a = 0.36$ μC/cm^2 and $P_c = 0.18$ μC/cm^2, where a is the rung direction and c is the ladder direction. Therefore, the total polarization is 0.40 μC/cm^2 which is compatible with the calculation value (0.42 μC/cm^2) based on STEM images in reference [154].

4.5 Magnetoelectric Coupling Study

To study the magnetoelectric coupling, we first tried to measure the hysteresis cycle of the polarization curve as a function of the electric field, at 300 K and 150 K. However, the system is only weakly localized, the electronic gap has been measured to be about 148 meV above 120 K [Fig. 4.7]. The low energy gap is also observed in several previous researches [126, 127, 133, 134]. We, therefore, encountered electronic charge leakage even at low temperatures, i.e., the sample is too conductive to detect a dielectric effect. This prevented the detection of the electric polarization.

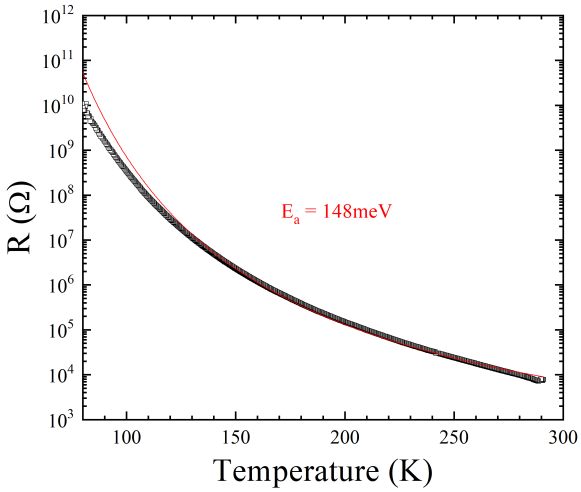

Figure 4.7: Temperature dependence of the resistance of the $BaFe_2Se_3$ crystal. The voltage was put along the a-axis ($Pnma$ setting). The red line is the fitting with the thermal activation model $R = R_0 exp(E_a/k_B T)$, where R_0 is a prefactor, E_a is the thermal activated energy, and k_B is the Boltzmann's constant. We obtained $E_0 = 148$ meV above 120 K.

Then, we tried another technique. We measured the capacitance as a function of the magnetic field at low temperatures. The electric capacitance along different directions was measured separately when the magnetic field varied along with the three directions. None of these measurements showed any anomaly except when the voltage and field were along the a-axis. As shown in Figure 4.8, the capacitance decreases above 4 T, indicating a magnetoelectric effect. To avoid the possible sample defect and artificial error, the field was decreased to -9 T. As we can see, the same decrease appeared below -4 T, confirming our finding.

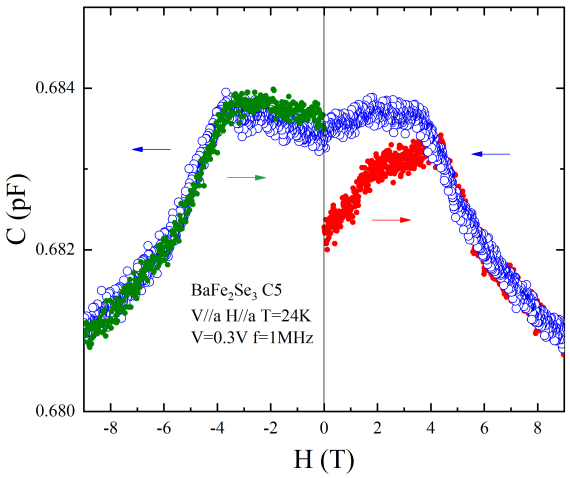

Figure 4.8: Magnetic field dependence of the capacitance of the $BaFe_2Se_3$ crystal at 24 K. The voltage and field are both along the *a*-axis (*Pnma* setting). The field is increased from zero to 9 T (red circles), and then decreased to -9 T (blue circles), finally back to 0 (green circles).

4.6 Summary

In this chapter, we ruled out the non-polar structure of $BaFe_2Se_3$, characterized by the average *Pnma* space group, proposed until now. The $Pmn2_1$ structure we proposed is polar with an electric polarization along the rung of the Fe ladders was. In the magnetic phase, the structure is modified to the *Pm* space group, and the electric polarization is strongly enhanced. Besides, the change of capacitance at 4 T suggests a strong magnetoelectric coupling. $BaFe_2Se_3$ thus presents an ideal multiferroic behaviour. As for the superconducting state, which competes with the multiferroic ground state under pressure, its stabilization remains an issue of tremendous importance. The presence of eight different Fe-Fe distances in the *Pm* structure at low temperature has now to be considered in the theoretical models involving the (*t*-*J*) competition [192].

5

Study of Magnetic Structure of $BaFe_2Se_3$

Contents

The present chapter is concerned with determining the magnetic structures of $BaFe_2Se_3$ at different pressures. In Section 5.2, an umbrella-like magnetic structure was revealed at ambient pressure by the single-crystal neutron diffraction study and symmetry analysis. We determined the C_am magnetic group, which corresponds to a Block-A magnetic order. A tilt of the moment in the ac and bc planes was revealed. In addition, the tilted moments were confirmed by a polarized neutron scattering measurement. In Section 5.3, we investigated the frontier between the magnetic and superconducting (SC) phases by performing a challenging powder neutron diffraction (PND) and Fe K_β X-ray emission spectroscopy (XES) under high pressure. We showed that the ambient-pressure ground state with a block-like magnetic order is destabilized and replaced by a new stripe-like order under pressure. Besides, we evidenced that the local magnetic moment persisted even in the SC phase.

5.1 Context and Motivation

Unconventional superconductivity and magnetism seem to be mutually exclusive in most cases. However, magnetic order is a necessary foe of unconventional superconductivity since it is systematically present in the vicinity of the superconducting phase. Furthermore, it is generally accepted that the presence of fluctuations associated with this magnetic phase contribute to the pairing of Cooper pairs in many superconductors, such as the large families of heavy fermions [193, 194], organic compounds [195], iron-based pnictides [196, 197], or high critical temperature cuprates [198]. Thus the description of the magnetic structure of $BaFe_2Se_3$ is considered to be an essential step to understanding its pairing mechanism.

Until now, the accurate magnetic structure of $BaFe_2Se_3$ is still not solved. The authors of reference [5] proposed a Block-A magnetic order [Fig. 5.1(a)] while those of references [4] and [133] preferred a Block-B structure [Fig. 5.1(b)]. The difference relies on the fact that the ferromagnetic 2×2 superblocks between ladder-A and ladder-B are antiferromagnetically ordered in the Block-A model, while there is a phase shift of one Fe-Fe distance between them in the Block-B model. Besides, a first-principles study found that the energy per Fe for Block-B structure is the lowest among various magnetic models, while the energy of Block-A is just 7.9 meV/Fe higher which is close to the error bars of DFT calculations [Fig. 2.12(d)] [8]. The lack of reliable magnetic structure avoids further progress in the understanding of the remarkable physical properties of $BaFe_2Se_3$. We thus studied the accurate magnetic order by single-crystal neutron diffraction and polarized neutron scattering in section 5.2.

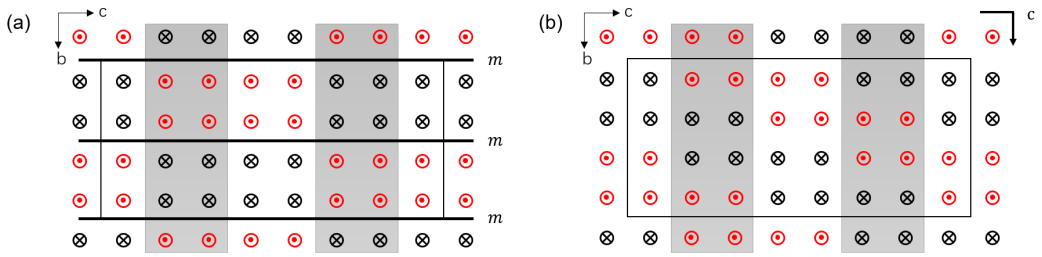

Figure 5.1: (a) and (b) Projections of the Fe atoms on the bc-plane of Block-A and Block-B magnetic orders, respectively. The m mirror planes of C_am and c glide plane of C_ac are shown. The spins are perpendicular to the bc plane. Notice that the shown axes are in $Pnma$ setting. The black rectangles indicate the magnetic unit cell. The Fe ladders-A (B) are represented by white (grey) backgrounds.

On the other hand, a clear description of the magnetic state under pressure close to the SC phase is also missing for $BaFe_2Se_3$. A previous first-principles study shows that the CX stripe-like and 2×2 block-like AFM states are both the alternative ground states for a purely electronic Hubbard model [135]. Besides, a stripe magnetic order was observed in the parent compound $BaFe_2S_3$ [9]. Therefore, the competition between the block magnetic state and the stripe-like one should be considered. To investigate this issue, we performed the powder neutron diffraction and Fe K_β XES measurements under high pressure, particularly in the SC dome, in section 5.3.

5.2 Magnetic Structure at Ambient Pressure

5.2.1 Experimental Details and Data Analysis

Temperature dependence of powder neutron diffraction experiments at ambient pressure was carried out on a powder sample of 1 g on the G4.1 diffractometer (Orphée-LLB, CEA-Saclay, France). The neutron

wavelength was 2.426 Å. The diffraction data were collected from 5° to 82°. Then, the diffraction patterns were refined by the FULLPROF suite [199].

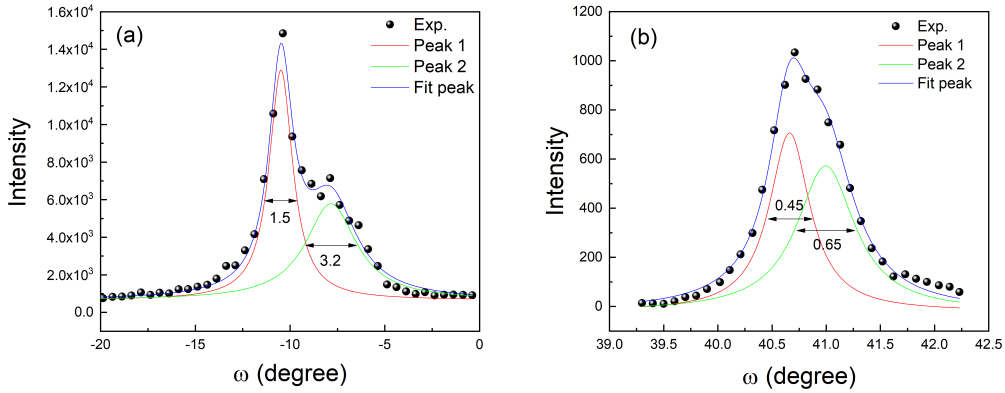

Figure 5.2: The Omega scan of the (200) and (404) nuclear reflections of the big (a) and small (b) specimens at 10 K, respectively. The black circles are experimental data, the colorful lines are the fitting results with a Lorentzian distribution.

The single-crystal neutron diffraction measurements were performed on the thermal neutron two-axis diffractometer D23 at the ILL (Grenoble, France). A standard aluminum holder in a He exchange gas cryostat was used to mount the sample and cool it down. The reflections data were collected on two specimens from batch C5 with the size of $12 \times 3 \times 1$ and $5 \times 2 \times 1$ mm^3, respectively. The most intense reflections of both specimens are shown in Figure 5.2. As we can see, the big specimen presents a much larger full width at half maximum (FWHM) than the small one, which indicates a worse mosaicity. Therefore, we chose the small specimen to study the magnetic structure of $BaFe_2Se_3$. The two peaks indicate the presence of at least two grains in the specimen. This is intrinsic to the morphology of the crystal related to the quasi-1D character of the system. As we know, the single crystals are constituted of multiple needles roughly aligned along the b-axis [127, 134]. Although the specimen is not a perfect single crystal, it is enough to determine the magnetic structure by neutron diffraction measurement. We made a collection at 10 K and then the data were refined by the JANA2006 program.

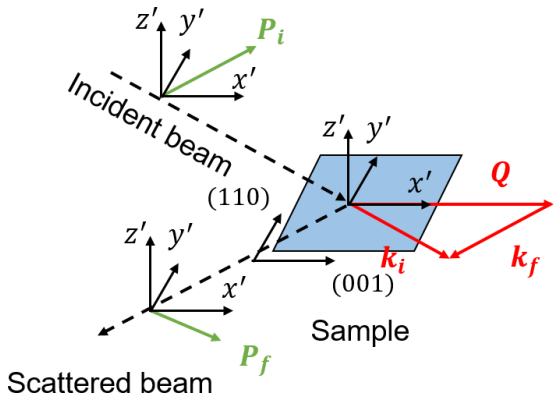

Figure 5.3: Scattering plane in the polarized neutron diffraction and the coordinate.

The single-crystal polarized neutron diffraction experiments were performed on the 4F1[1] triple-axis spectrometer at LLB, Saclay. The scattering plane, defined by the plane including the incident beam ($\mathbf{k}_i$) and scattered beam ($\mathbf{k}_f$), was (110) and (001) as shown in Figure 5.3. The sample can be rotated

[1] https://www-llb.cea.fr/fr-en/pdf/4f1-llb.pdf

perpendicular to this plane. x' is defined as the axis along $\mathbf{Q}$, y' is perpendicular to $\mathbf{Q}$ and in the scattering plane, and thus z' is perpendicular to the scattering plane [Fig. 5.3]. With this scattering plane, we can obtain the reflections with the Miller index (hhl). In our experiments, the polarization of the incident beams $\mathbf{P}_i$ is parallel or antiparallel to one of the three axes. And the intensities of the final beams with the polarization $\mathbf{P}_j$ along all six directions are measured for each experiment. The ratio between the final and incident beams is calculated as $\sigma = I_{\mathbf{P}_f}/I_{\mathbf{P}_i}$. Therefore, a total number of 36 components can be obtained from the measurements as shown in Table 5.1.

Table 5.1: The components obtained from the single-crystal polarized neutron diffraction.

Final \ Incident	$\mathbf{P}_{x'}$	$\mathbf{P}_{y'}$	$\mathbf{P}_{z'}$	$-\mathbf{P}_{x'}$	$-\mathbf{P}_{y'}$	$-\mathbf{P}_{z'}$
$\mathbf{P}_{x'}$	$\sigma^{++}_{x',x'}$	$\sigma^{++}_{y',x'}$	$\sigma^{++}_{z',x'}$	$\sigma^{-+}_{x',x'}$	$\sigma^{-+}_{y',x'}$	$\sigma^{-+}_{z',x'}$
$\mathbf{P}_{y'}$	$\sigma^{++}_{x',y'}$	$\sigma^{++}_{y',y'}$	$\sigma^{++}_{z',y'}$	$\sigma^{-+}_{x',y'}$	$\sigma^{-+}_{y',y'}$	$\sigma^{-+}_{z',y'}$
$\mathbf{P}_{z'}$	$\sigma^{++}_{x',z'}$	$\sigma^{++}_{y',z'}$	$\sigma^{++}_{z',z'}$	$\sigma^{-+}_{x',z'}$	$\sigma^{-+}_{y',z'}$	$\sigma^{-+}_{z',z'}$
$-\mathbf{P}_{x'}$	$\sigma^{+-}_{x',x'}$	$\sigma^{+-}_{y',x'}$	$\sigma^{+-}_{z',x'}$	$\sigma^{--}_{x',x'}$	$\sigma^{--}_{y',x'}$	$\sigma^{--}_{z',x'}$
$-\mathbf{P}_{y'}$	$\sigma^{+-}_{x',y'}$	$\sigma^{+-}_{y',y'}$	$\sigma^{+-}_{z',y'}$	$\sigma^{--}_{x',y'}$	$\sigma^{--}_{y',y'}$	$\sigma^{--}_{z',y'}$
$-\mathbf{P}_{z'}$	$\sigma^{+-}_{x',z'}$	$\sigma^{+-}_{y',z'}$	$\sigma^{+-}_{z',z'}$	$\sigma^{--}_{x',z'}$	$\sigma^{--}_{y',z'}$	$\sigma^{--}_{z',z'}$

5.2.2 Powder Neutron Diffraction

To investigate the magnetic structure of $BaFe_2Se_3$ at ambient pressure, we first performed the PND measurements as a function of temperature by G4.1 at LLB. The $(\frac{1}{2}\frac{1}{2}\frac{1}{2})$ magnetic reflection at $Q \sim 0.73$ Å^{-1} was observed at low temperature, compatible with the block magnetic order proposed in previous studies [4, 5, 133]. Figure 5.4 (a) and (b) show the refinements of the PND patterns at 1.5 K with the Block-A and Block-B models, respectively. We used the *Pnma* space group for the refinements since the slight difference between *Pnma* and *Pm* (discovered in Chapter 4) is negligible in the powder diffraction experiment. As can be seen, the difference between the two models is negligible. The resulting crystallographic parameters from the Rietveld refinement of the PND data at 1.5 K are given in Table 5.2. A moment of 2.5 (±0.1) μ_B per Fe was obtained for both models.

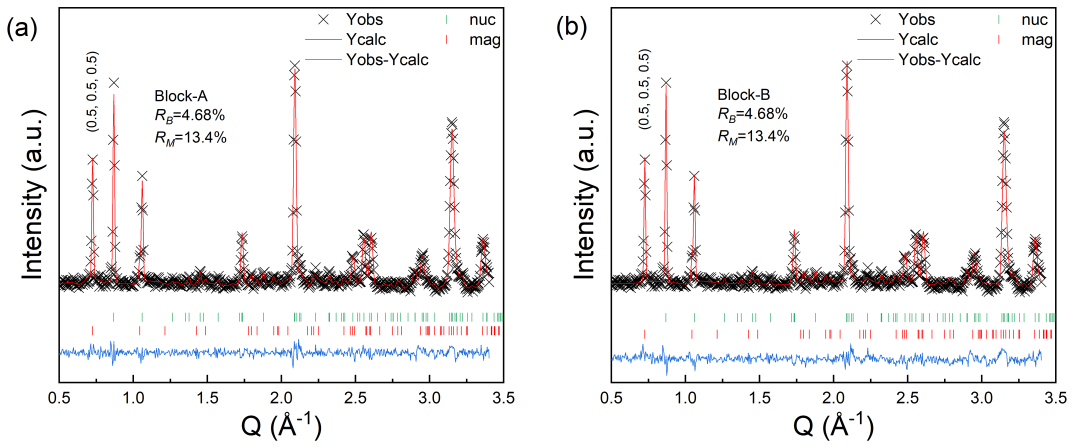

Figure 5.4: PND patterns of $BaFe_2Se_3$ at 1.5 K and the refinement results with Block-A(a) and Block-B(b) models.

Furthermore, we extracted the magnetic moment for each temperature [Fig. 5.5]. As we can see, the moment saturates below 50 K at 2.5 μ_B. The thermal evolution is characteristic of a second-order phase transition. We then fitted the curve with an order parameter power law:

$$M = M_0 \left(1 - \frac{T}{T_N}\right)^{\beta}, \qquad (T < T_N), \tag{5.1}$$

where M_0 is the critical amplitude. We obtained a critical exponent of $\beta \approx 0.23$, which is closer to a 3D-Ising model ($\beta = 0.33$) than to the mean-field one ($\beta = 0.5$). Besides, the T_N was estimated to be 210 (±10) K. One should notice that the moments obtained from the two different models are identical. Since the PND experiment cannot distinguish the two block-like magnetic orders, the single-crystal neutron diffraction measurement is necessary. Besides, it is also worth noticing that the PND experiment is also not accurate enough to investigate a possible canting of the spins from the a_{o1}-axis.

Table 5.2: Atomic positions of $BaFe_2Se_3$ at 1.5 K under ambient pressure in the *Pnma* space group (Bragg R-factor R_B=4.68%, Magnetic R-factor R_M=13.4%). The lattice parameters are a_{o1} = 11.8451 Å, b_{o1} = 5.4015 Å, and c_{o1} = 9.1271 Å, $\alpha_{o1} = \beta_{o1} = \gamma_{o1} = 90°$.

Atom	Site	x	y	z	B
Ba1	4c	0.1812(7)	0.25	0.5211(6)	0.4270(6)
Fe1	8d	0.4935(6)	0.0019(4)	0.3531(9)	0.1328(8)
Se1	4c	0.3560(1)	0.25	0.2358(6)	0.3818(7)
Se2	4c	0.6321(4)	0.25	0.4874(8)	0.3160(1)
Se3	4c	0.3966(7)	0.25	0.817(4)	0.2485(5)

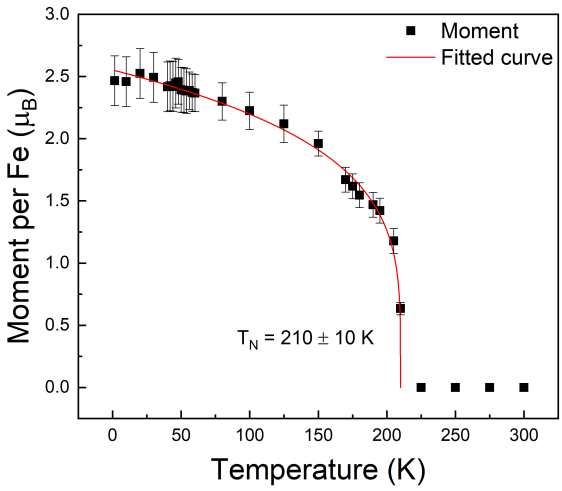

Figure 5.5: The temperature dependence of the moment per Fe extracted from Rietveld refinements of PND data. The red line represents the fit of the order parameter power law.

5.2.3 Magnetic Space Group Analysis

The magnetic space groups are the symmetry groups that classify the symmetries of not only the nuclear structure but also the magnetic structure [200]. The determination of the correct magnetic space group is an essential starting point for studying the magnetic structure. The k-Subgroupsmag program of the Bilbao Crystallographic Server can provide the possible magnetic subgroups of a paramagnetic space group with a known propagation vector k [201]. In our case, starting from the $Pmn2_1$ space group

below T_N determined in Chapter 4 with the magnetic propagation vector $k = (\frac{1}{2}, \frac{1}{2}, \frac{1}{2})$, three magnetic subgroups are proposed : C_ac, C_am and P_S1 [Fig. 5.6(top)]. Since the last space group is of low symmetry, we focused on the other two. As shown in Figure 5.1, from a symmetry point of view, the m mirror of C_am is responsible for the Block-A magnetic order while the c glide plane of C_ac corresponds to the Block-B. Therefore, the determination of the magnetic space group automatically fixes the nature of the block-like order. Furthermore, from previous results of X-ray diffraction (Chapter 4), TEM microscopy [154], and lattice dynamics [190] studies, the nuclear space group in the magnetic phase is Pm. With $k = (\frac{1}{2}, \frac{1}{2}, \frac{1}{2})$, the only possible subgroup of high symmetry is C_am [Fig. 5.6(bottom). Obviously, this symmetry analysis thus excludes the Block-B magnetic order at low temperatures.

Subgroups of the paramagnetic space group : $Pmn2_11'$ (N. 31)
Lowest magnetic space group to consider: $P1$ (N. 1.1)
Magnetic propagation wave-vectors (0.5,0.5,0.5)

List of subgroups that fulfill the given conditions

Get the subgroup-graph

N	Group Symbol	Transformation matrix	Group-Subgroup index	Other members of the Conjugacy Class	irreps	Magnetic structure models (MAGMODELIZE)
1	C_ac (No. 9.41)	$\begin{pmatrix} 0 & 0 & 1 & 0 \\ 0 & 2 & 0 & 1/2 \\ -2 & 0 & 1 & 0 \end{pmatrix}$	4=2x2	Conjugacy Class	Get irreps	☐
2	C_am (No. 8.36)	$\begin{pmatrix} 0 & -2 & 0 & 1/2 \\ 2 & 0 & -1 & 0 \\ 0 & 0 & 1 & 0 \end{pmatrix}$	4=2x2	Conjugacy Class	Get irreps	☐
3	P_S1 (No. 1.3)	$\begin{pmatrix} 1 & -1 & -2 & 0 \\ 0 & 1 & 2 & 0 \\ 1 & 0 & 2 & 0 \end{pmatrix}$	8=2x4	Conjugacy Class	Get irreps	☐

Subgroups of the paramagnetic space group : $Pm1'$ (N. 6)
Lowest magnetic space group to consider: $P1$ (N. 1.1)
Magnetic propagation wave-vectors (0.5,0.5,0.5)

List of subgroups that fulfill the given conditions

Get the subgroup-graph

N	Group Symbol	Transformation matrix	Group-Subgroup index	Other members of the Conjugacy Class	irreps	Magnetic structure models (MAGMODELIZE)
1	C_am (No. 8.36)	$\begin{pmatrix} 0 & 0 & 1 & 0 \\ 0 & 2 & 0 & 1/2 \\ -2 & 0 & 1 & 0 \end{pmatrix}$	2=2x1	Conjugacy Class	Get irreps	☐
2	C_am (No. 8.36)	$\begin{pmatrix} 0 & 0 & 1 & 0 \\ 0 & 2 & 0 & 0 \\ -2 & 0 & 1 & 0 \end{pmatrix}$	2=2x1	Conjugacy Class	Get irreps	☐
3	P_S1 (No. 1.3)	$\begin{pmatrix} 1 & -1 & -2 & 0 \\ 0 & 1 & 2 & 0 \\ 1 & 0 & 2 & 0 \end{pmatrix}$	4=2x2	Conjugacy Class	Get irreps	☐

Figure 5.6: Magnetic subgroups of $Pmn2_1$ (top) and Pm (bottom) with $k = (\frac{1}{2}, \frac{1}{2}, \frac{1}{2})$.

5.2.4 Single-Crystal Neutron Diffraction

In the single-crystal neutron diffraction measurement, 376 reflections, including 128 nuclear and 248 magnetic reflections, were recorded at 10 K. We then refined the crystal structure with an initial nuclear structure ($a_{m1} = 9.1499$ Å, $b_{m1} = 5.4488$ Å, $c_{m1} = 11.8672$ Å, $\beta_{m1} = 90.03°$, and $\alpha_{m1} = \gamma_{m1} = 90°$) in the Pm space group from Chapter 4. One should notice that, the lattice parameters cannot be extracted from this experiment, since we used a 1D detector. Therefore, they were fixed as the initial values. The resulting structure is shown in the Table 5.3. A reliability factor $R(obs) = 2.08\%$ was obtained.

Furthermore, to refine the magnetic structure, the propagation vector $k = (\frac{1}{2}, \frac{1}{2}, \frac{1}{2})$ was introduced. As mentioned above, the Pm space group with $k = (\frac{1}{2}, \frac{1}{2}, \frac{1}{2})$ is only compatible with the magnetic space group C_am. In Jana2006, we can directly convert the parent Pm structure to the C_am magnetic subgroup. Moreover, to facilitate the comparison with the average $Pnma$ setting, we converted the C_am cell to a double-$Pnma$-cell with $a_d = 23.7346$ Å, $b_d = 10.8978$ Å, $c_d = 18.2992$ Å, $\beta_d = 90.03°$, and $\alpha_d = \gamma_d = 90°$. One should notice that the double setting is a monoclinic setting in stead of orthorhombic. The transformation matrices between the three crystal cells are shown in Figure 5.7. The following discussions are all based an the double-$Pnma$-setting. Besides, one should notice that

Table 5.3: Atomic positions of $BaFe_2Se_3$ at 10 K in the Pm space group. The refinement gives R_{obs} = 2.08%. The lattice parameters are a_{m1} = 9.1496 Å, b_{m1} = 5.4489 Å, c_{m1} = 11.8673 Å, β_{m1} = 90.03°, and $\alpha_{m1} = \gamma_{m1}$ = 90°. The isotropic ADPs (Uiso) are also shown.

Atom	Site	x	y	z	Uiso	Atom	Site	x	y	z	Uiso
Ba1_1_1	1b	0.524042	0.500000	-0.435370	0.018(14)	Se1_2_1	1a	-0.231846	0.000000	0.103896	0.001(7)
Ba1_1_2	1a	0.024098	0.000000	0.435576	0.034(13)	Se1_2_2	1b	-0.731854	0.500000	-0.103896	0.004(10)
Ba1_2_1	1a	-0.524042	0.000000	-0.064416	-0.009(14)	Se2_1_1	1b	0.489388	0.500000	-0.877594	-0.003(9)
Ba1_2_2	1b	-0.024088	0.500000	0.064620	-0.025(13)	Se2_1_2	1a	-0.010618	0.000000	0.877586	-0.009(6)
Fe1_1_1	2c	0.352566	0.263324	-0.742794	-0.006(5)	Se2_2_1	1a	-0.489394	0.000000	0.377578	0.014(9)
Fe1_1_2	2c	-0.147374	0.729532	0.743106	0.011(7)	Se2_2_2	1b	-0.989380	0.500000	-0.377598	0.020(13)
Fe1_2_1	2c	-0.352574	0.255482	0.242764	0.016(7)	Se3_1_1	1b	0.817830	0.500000	-0.652242	0.002(11)
Fe1_2_2	2c	-0.852622	0.741114	-0.243146	-0.004(7)	Se3_1_2	1a	0.317832	0.000000	0.652240	0.022(12)
Se1_1_1	1b	0.231846	0.500000	-0.603912	0.001(11)	Se3_2_1	1a	-0.817832	0.000000	0.152230	0.004(8)
Se1_1_2	1a	-0.268148	0.000000	0.603882	0.001(13)	Se3_2_2	1b	-0.317832	0.500000	-0.152230	-0.006(7)

the atomic positions were fixed during the refinements of magnetic structures.

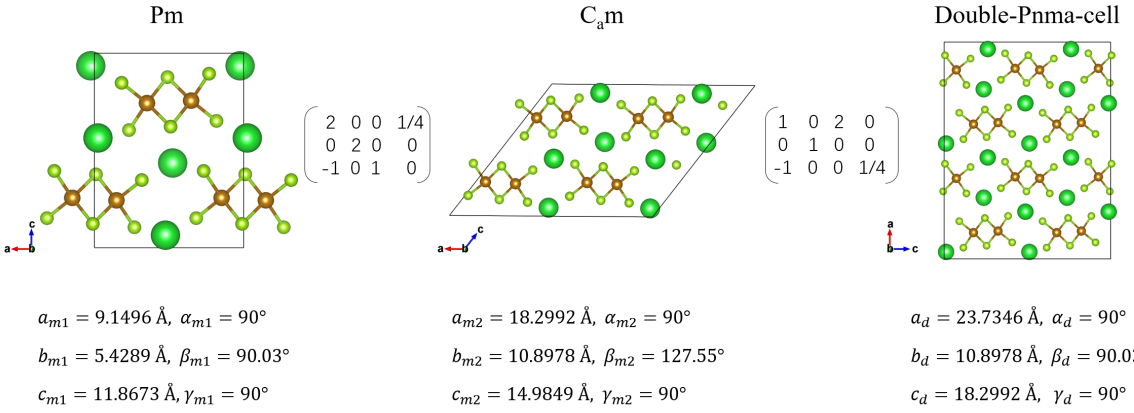

Figure 5.7: The crystal structures of Pm, C_am and double-$Pnma$-cell and the transformation matrices between them. The subscript m indicates the monoclinic cell and d for the double-setting cell.

We first refined the magnetic structure with all Fe magnetic moments identical in magnitude and along the a_d-axis, i.e., with Block-A model. This is not required by the symmetry constraints of C_am but corresponds to the magnetic orders proposed in previous works [4, 5]. We first obtained a magnetic R-factor of R_{obs}(mag) = 56.03%, which is far from a good fit. As we know, the transition from the $Pmn2_1$ paramagnetic phase to the Pm antiferromagnetic phase will lose a two-fold axis along c_{o2}, which is c_d in the double-$Pnma$-cell, and automatically produce twins. We thus added a twin corresponding to the two-fold axis along c_d in the doubled cell. The twinning matrix is

$$\begin{pmatrix} -1 & 0 & 0 \\ 0 & -1 & 0 \\ 0 & 0 & 1 \end{pmatrix}. \tag{5.2}$$

One should notice that the two-fold axes along a_d and b_d will give the same domains as the existed two above since the neutron data cannot distinguish between domains related by the inversion center. Finally, we obtained a magnetic R-factor of R_{obs}(mag) = 16.83% and M_x = 2.33 μ_B per Fe with the twin fraction $twvol2$ = 0.5001. The resulting magnetic structure is shown in Figure 5.8

We then authorized the rotation of the moments around the a_d-axis. To obtain more reasonable results, the absolute values of the tilting angles were restricted to be identical for all the Fe. The

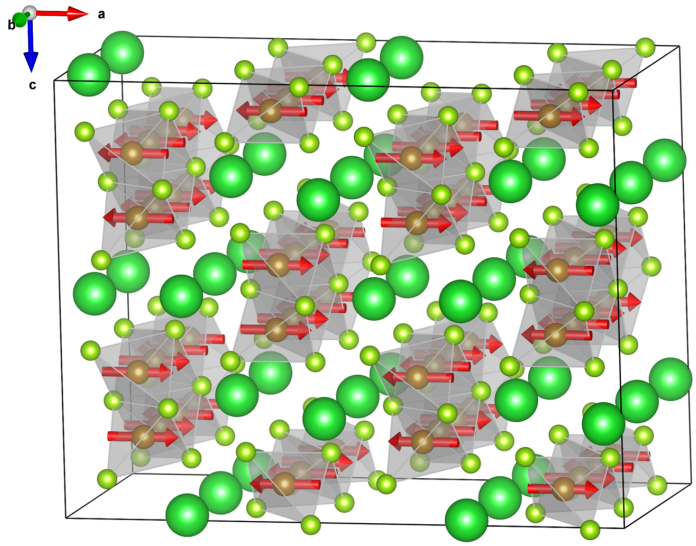

Figure 5.8: The magnetic structure of $BaFe_2Se_3$ in the double-*Pnma*-cell with the moments along a_d.

best magnetic R-factor we got was R_{obs}(mag) = 9.16%. The observed structure factors versus the calculated ones are plotted in Figure 5.9(a). The results of the refinement are listed in Table 5.4. The moments are tilted from the a_d-axis by 18° in the $a_d b_d$ plane and by 30° in the $a_d c_d$ plane. Figure 5.9(b) shows the projections of the Fe atoms and their spins on the $b_d c_d$-plane. As we can see, the spins of each block form an umbrella-type structure. The net moment of each block is only along the a_d-axis and antiferromagnetically arranged along the b_d-axis. It is important to notice that the angles between the Fe-Se bonds and the moments are 20 ± 1°. Thus, the moments are roughly aligned along the apical direction of the tetrahedra, which must be the easy axis of the moment in its local environment [Fig. 5.9(c)].

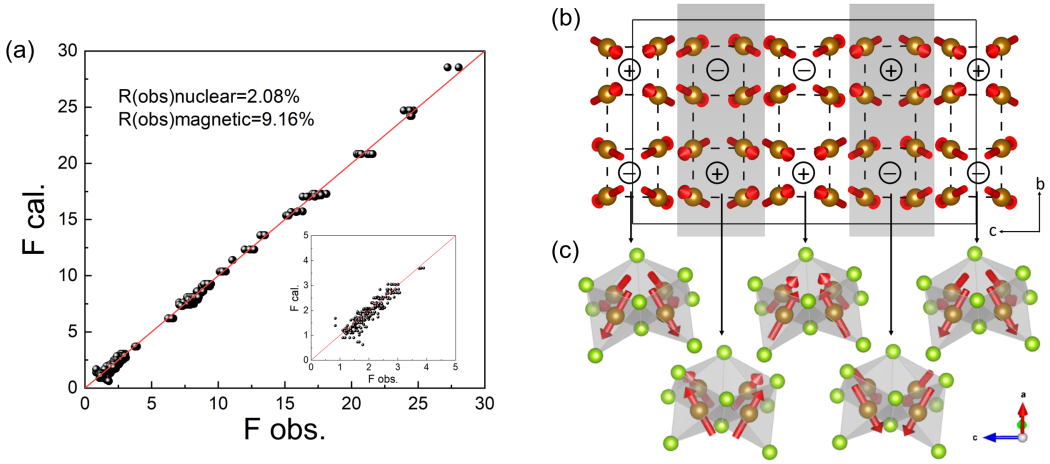

Figure 5.9: (a) Result of the refinement for the C_am magnetic structure. Structure factors of nuclear and magnetic Bragg reflections collected at 10 K are plotted against the calculated values. The inset shows the range of low F values, which mainly represents the magnetic reflections. (b) Projections of the Fe atoms on the $b_d c_d$-plane with the tilting spins in Block-A magnetic order. The yellow balls indicate the Fe atoms. The red arrows are the spins of Fe. The + and − indicate the net moments of the blocks. The Fe ladders-A (B) are represented by white (grey) backgrounds. (c) The $FeSe_4$ tetrahedra of the blocks in (b) (indicated by the black arrows).

Table 5.4: Parameters of the magnetic structure of $BaFe_2Se_3$ at 10 K in the double-Pnma-setting. The number of reflections with I>3$_\sigma$ is 376 including nuclear and magnetic reflections.

		$BaFe_2Se_3$ (Double-Pnma-setting)
1	Parent space group	Pm (N. 6)
2	Propagation vector	(1/2 1/2 1/2)
3	Magnetic space group	C_am (N. 8.36)
3	Transformation from parent setting to the one used	(2c,2b,-2a;1/4,0,1/4)
5	unit cell parameters	a_d=23.7346 Å, α_d = 90° b_d=10.8978 Å, β_d = 90.03° c_d=18.2992 Å, γ_d = 90°
6	Positions of magnetic atoms	Fe1_1_1 -0.3714 0.1321 -0.1763 Fe1_1_2 0.3716 0.3651 0.0737 Fe1_2_1 0.1214 0.1281 0.1763 Fe1_2_2 -0.1216 0.3701 0.4263
7	Positions of non-magnetic atoms	Ba1_1_1 -0.2177 0.25 -0.2620 Ba1_1_2 0.2178 0.5 -0.0121 Ba1_2_1 -0.0322 0 0.2620 Ba1_2_2 0.0323 0.25 0.5120 Se1_1_1 -0.3020 0.25 -0.1159 Se1_1_2 0.3019 0.5 0.1341 Se1_2_1 0.0520 0 0.1159 Se1_2_2 -0.0520 0.25 0.3659 Se2_1_1 -0.4388 0.25 -0.2447 Se2_1_2 0.4388 0.5 0.0053 Se2_2_1 0.1888 0 0.2447 Se2_2_2 -0.1888 0.25 0.4947 Se3_1_1 -0.3261 0.25 -0.4089 Se3_1_2 0.3261 0.5 -0.1589 Se3_2_1 0.0761 0 0.4089 Se3_2_2 -0.0761 0.25 0.6589
8	Magnetic moments of mangetic atoms and their symmetry constraints	Fe1_1_1 2.13 0.68 1.26 (mx,my,mz) Fe1_1_2 2.13 -0.68 -1.26 (mx,my,mz) Fe1_2_1 2.13 0.68 -1.26 (mx,my,mz) Fe1_2_2 2.13 -0.68 1.26 (mx,my,mz)
9	Number of reflections (Nuclear) R_{obs}, wR_{obs}	128 2.08%, 2.62%
10	Number of reflections (Magnetic) R_{obs}, wR_{obs}	248 9.16%, 8.37%
11	twin factor	$twvol2$ = 0.5014

5.2.5 Polarized Neutron Diffraction

We also performed single-crystal polarized neutron diffraction to confirm our results. We performed a full polarization analysis on the (111) Bragg reflection at 150 K and ($\frac{1}{2}\frac{1}{2}\frac{1}{2}$) magnetic reflection at both 60 K and 5 K. Six terms are extracted from the experiments: the nuclear term (N), the moment along y′ and z′ ($M_{y'}$ and $M_{z'}$), the chiral term (M_{ch}), the nuclear-magnetic interference terms ($R_{y'}$ and $R_{z'}$). They are calculated as:

$$N = \sigma^{++}_{x',x'} = \sigma^{--}_{x',x'}, \tag{5.3}$$

$$M_{y'} = \frac{\sigma^{++}_{y',y'} + \sigma^{--}_{y',y'}}{2} - \frac{\sigma^{++}_{x',x'} + \sigma^{--}_{x',x'}}{2} = \frac{\sigma^{+-}_{x',x'} + \sigma^{-+}_{x',x'}}{2} - \frac{\sigma^{+-}_{y',y'} + \sigma^{-+}_{y',y'}}{2}, \tag{5.4}$$

$$M_{z'} = \frac{\sigma^{++}_{z',z'} + \sigma^{--}_{z',z'}}{2} - \frac{\sigma^{++}_{x',x'} + \sigma^{--}_{x',x'}}{2} = \frac{\sigma^{+-}_{x',x'} + \sigma^{-+}_{x',x'}}{2} - \frac{\sigma^{+-}_{z',z'} + \sigma^{-+}_{z',z'}}{2}, \tag{5.5}$$

$$M_{ch} = \frac{\sigma^{-+}_{x',x'} - \sigma^{+-}_{x',x'}}{2P_0}, \tag{5.6}$$

$$R_y = \frac{\sigma^{++}_{y',y'} - \sigma^{--}_{y',y'}}{2P_0}, \tag{5.7}$$

$$R_z = \frac{\sigma^{++}_{z',z'} - \sigma^{--}_{z',z'}}{2P_0}, \tag{5.8}$$

where $P_0 = 1$ when the incident beam is along x', y', or z', and $P_0 = -1$ when it is along $-x'$, $-y'$, or $-z'$. Meanwhile, all the six terms of $(\frac{1}{2}\frac{1}{2}\frac{1}{2})$ are calculated with the magnetic model proposed above. The results are presented in Table 5.5. As can be seen, only the nuclear term is non-zero on the (111) reflection at 150 K as expected. At low temperature, the ratios between the $M_{z'}$ and $M_{y'}$ amplitudes of the magnetic reflection $(\frac{1}{2}\frac{1}{2}\frac{1}{2})$ are around 4 (4.3 for 60 K and 3.8 for 5 K), which confirms that the moment is tilted away from the a_d-axis since a moment along a_d would give a ratio above 20. Besides, the different ratios between 60 K and 5 K may indicate a temperature dependence of the tilt. Beside, the calculation at 10 K gives a value of 7.7 for $M_{z'}/M_{y'}$ close to the experimental value. Therefore, the result of the single-crystal polarized neutron diffraction is compatible with the magnetic structure proposed above with a canting of the moments.

Table 5.5: Relative intensity of the terms extracted from the full polarization analysis on the (1,1,1) nuclear Bragg at 150 K, and (0.5,0.5,0.5) Bragg at 60 K and 5 K, and calculated values of these terms from the refined magnetic structure at 10 K. One should notice that the values are dimensionless quantities, i.e., only the ratio between them are meaningful.

(hkl)	(111)	$(\frac{1}{2}\frac{1}{2}\frac{1}{2})$	$(\frac{1}{2}\frac{1}{2}\frac{1}{2})$	$(\frac{1}{2}\frac{1}{2}\frac{1}{2})$
Temperature	150 K	60 K	5 K	10 K(calc)
N	0.26(1)	0.012(1)	0.020(4)	0
$M_{y'}$	0.001(1)	0.085(3)	0.109(4)	0.07
$M_{z'}$	-0.004(3)	0.363(2)	0.42(3)	0.54
M_{ch}	0.002(1)	0.008(2)	-0.049(3)	0.32
$R_{y'}$	0.005(2)	0.002(1)	-0.011(1)	0
$R_{z'}$	0.001(1)	0.010(1)	-0.044(2)	0

Another noticeable result from polarized neutron diffraction is the presence of a very small value of N, $R_{y'}$, and $R_{z'}$ for $(\frac{1}{2}\frac{1}{2}\frac{1}{2})$ at 5 K. However, these terms N could not be calculated with our experimental model since only the magnetic structure was considered. After warming up to 60 K, these terms strongly decrease but remain finite. Furthermore, the chiral term M_{ch} is non-zero at 5 K. One should notice that the structure determined by single-crystal neutron diffraction is also chiral. In the case of a single chiral domain, we calculated that M_{ch} would have nearly half the value of $M_{z'}$ for the $(\frac{1}{2}\frac{1}{2}\frac{1}{2})$ Bragg reflection. The much smaller value measured for chirality in our experiment is likely due to the presence of several twins inherent to the $Pmn2_1$ to P_m magnetic transition as mentioned above. Interestingly, we can see that the chiral term vanishes at 60 K. This effect cannot be ascribed to the decrease of the ordered moment since the $M_{z'}$ and $M_{y'}$ amplitudes only drop by nearly 20% while the chiral amplitudes drop by more than 90%. This disappearance is thus a fingerprint of an evolution of the magnetic structure at the higher temperature due to numerous frustrating exchange interactions responsible for this block-like magnetic ordering.

5.2.6 Summary

In this section, we determined the accurate magnetic order of the challenging spin ladder compound $BaFe_2Se_3$. We showed that the exact structure is the AFM Block-A type, which is also of great interest regarding the multiferroic properties. According to reference [2], the Block-A (labeled Block-MF by Dong et al.) should lead to a strong net polarization ($2.01\mu C/cm^2$) along a_d while the Block-B (labeled Block-Ex by Dong et al.) will induce a small polarization ($0.19\mu C/cm^2$) along c_d. Therefore, our results confirmed the potential strong electric polarization in $BaFe_2Se_3$, which is difficult to evidence experimentally as discussed in Chapter 4.

We also evidenced a canting of the spins with respect to the a_d-axis of about 30° and 18° in the a_dc_d and a_db_d planes, respectively. This canting does not produce any ferromagnetic component along b_d or c_d, and the net moment is only aligned along a_d. Interestingly, the spin orientation is roughly along one apical direction of the tetrahedra, a spontaneous easy axis for the ion in a tetrahedron. This could indicate that the anisotropy factor is strong compared to the exchange couplings involved in this system.

5.3 Evolution of the Magnetic Structure with Pressure

In most FeSCs, superconductivity emerges from suppressing the magnetic order. Thus, magnetism and superconductivity seem to be intimately related. The magnetic fluctuations in FeSCs presumably hold the clue to understanding the pairing mechanism. Therefore, we studied the magnetic structure of $BaFe_2Se_3$ under pressure, particularly near and in the superconducting phase, by powder neutron diffraction experiments in this section.

5.3.1 Experimental Details and Data Analysis

The experiments were performed on batch C5 since it displays higher T_N than C1, indicating a smaller deviation from the ideal stoichiometry. The X-ray diffraction patterns under pressure were collected at room temperature using the high pressure diffraction setup developed at LPS. The X-ray source was a Rigaku Mo rotating anode (λ=0.71Å) combined with a 2D MAR345 detector. The Diamond Anvil Cell (DAC) with diamonds of 1 mm diameter was equipped with a CuBe gasket of 70 μm thick. The sample chamber is 500 μm in diameter. The powder was loaded together with a ruby chip and Si oil transmitting medium. The pressure was then measured using the standard ruby fluorescence technique. For each measurement, a 2D MAR diffraction image was collected. Then, the Dioptas software [202] was used to treat the image and obtain the integrated powder diffraction pattern.

The neutron diffraction measurements under pressure were performed on D1B at ILL. Rietveld refinements of collected data were performed by FULLFROF [199]. The calibration of the experimental parameters (zero, wavelength, u, v, w) was performed at ambient conditions with $Al_2Ca_3F_{14}Na_2$ powder. The collected pattern and its refinement are shown in Figure 5.10.

For the PND measurements under pressure, a small lead, as a pressure indicator, was mixed with the powder and then sealed in a Paris-Edinburgh pressure cell. The pressure in the cell was determined by the equation of state (EOS) of lead. For a fixed temperature T, the pressure can be calculated by the Rydberg-Vinet universal EOS [203]. It can be predicted from three equilibrium quantities, the equilibrium volume V_0, the isothermal bulk modulus at ambient pressure B_0, and its pressure derivative at ambient pressure B_0', as below:

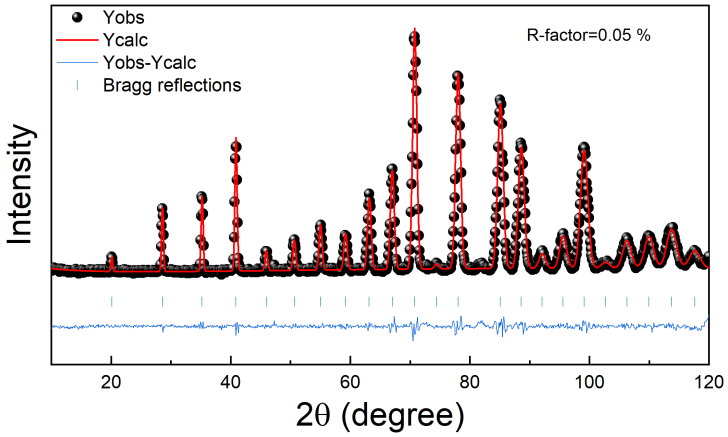

Figure 5.10: Rietveld refinement of PND pattern of $Al_2Ca_3F_{14}Na_2$ collected on D1B.

$$P(X) = \frac{3B_0}{X^2}(1-X)exp\left[\frac{3}{2(B_0'-1)}(1-X)\right], \tag{5.9}$$

where

$$X = \left(\frac{V}{V_0}\right)^{1/3},$$

$$B_0 = -\left(\frac{\partial P}{\partial lnV}\right)_0$$

$$B_0' = \left(\frac{\partial B_0}{\partial P}\right)_0.$$

$B_0(T)$ and $B_0'(T)$ at different temperatures are given in Table 5.6. With the lattice parameter of lead $a_i(Pb)$, which gives V, we can obtain the pressure in the cell. $a_i(Pb)$ can be determined by the positions of the Lead Bragg reflections under different pressures. To check the $a_0(Pb)$, we first made a collection at ambient conditions. By the refinement of the pattern, we obtained $a_0(Pb)$=4.9398 Å, which is in agreement with the calibration curve in the reference [183]. Then, the pressure was increased, followed by a cooling down to 3K. For each pressure point, one needs to heat the system above at least 200 K to keep the hydrostatic conditions and prevent any mechanical difficulties since the Helium is no more liquid at high pressure and low temperature. Generally, the heating procedure will cost eight hours, while the cooling also takes four hours. With the collection, for each pressure, we needed 3 shifts (24 h) at ILL. All the collections were performed at 3 K.

The evolution of the local magnetic moment on the Fe site was studied by the X-ray Emission Spectroscopy (XES) on the GALAXIES beamline [204] at Synchrotron SOLEIL. The GALAXIES beamline is dedicated to Inelastic X-ray Scattering (IXS) and X-ray Emission Spectroscopy (XES) experiments. When a core electron is excited by an incident X-ray photon, this excited state will decay by emitting an X-ray photon to fill the core hole. The spectra of the emitted X-rays are so-called XES. The resolution of XES is sufficient to analyze the impact of the chemical environment. In this work, the pressure was applied using a membrane-driven DAC equipped with 1.7-mm-thick diamonds with 900 μm culets. $BaFe_2Se_3$ powder was loaded in a 300-μm hole of an Inox gasket, along with a ruby chip for *in situ* pressure measurement and silicone oil as a pressure transmitting medium. We recorded the XES spectra as a function of pressure up to 14.7 GPa at room temperature, knowing that the local moment of $BaFe_2Se_3$ does not change with temperature [1]. An integrated absolute difference analysis

Table 5.6: $B_0(T)$, $B_0'(T)$ values used in the Rydberg-Vinet EOS [183].

T(K)	$B_0(T)$	$B_0'(T)$	T(K)	$B_0(T)$	$B_0'(T)$
0	48.33	5.45	160	44.94	5.57
20	48.24	5.45	180	44.41	5.59
40	47.95	5.46	200	43.87	5.62
60	47.5	5.48	220	43.34	5.64
80	47.00	5.50	240	42.80	5.66
100	46.49	5.52	260	42.27	5.68
120	45.97	5.54	280	41.73	5.70
140	45.46	5.55	300	41.20	5.72

was used to obtain the total local moment (S) on the Fe site by taking the FeS_2 spectrum as a reference of non-magnetic Fe (S = 0). This analysis is similar to the one used in parent Fe-based superconductors [205, 206].

5.3.2 Powder X-ray Diffraction under Pressure

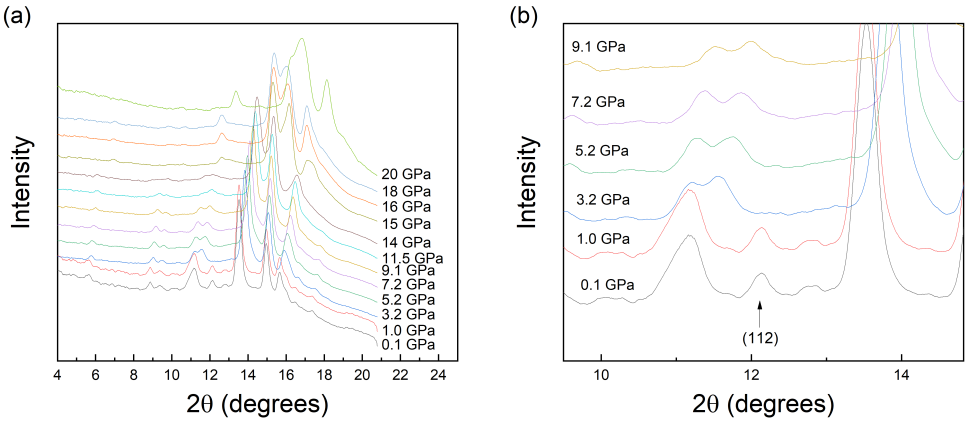

Figure 5.11: (a) Powder X-ray diffraction patterns of $BaFe_2Se_3$ under various pressures at 300 K. (b) Zoom in at low angle of (a) which shows the transition.

A nuclear transition from *Pnma* to *Cmcm* for $BaFe_2Se_3$ was observed around 4 GPa at ambient temperature in the reference [131]. To check the transition pressure of our sample, we first performed the powder X-ray diffraction measurements under multiple pressures at 300 K. Although we discovered that the real space group is $Pmn2_1$ at room temperature as presented in Chapter 4, the average *Pnma* space group was used since a powder diffraction experiment is not sensitive to the difference between them. Figure 5.11 shows the diffraction patterns under different pressures. As we can see, due to the small size of the sample chamber and the limitation of the DAC, we can only get the pattern at low angles [Fig. 5.11(a)]. However, the disappearance of the (112) reflection [(121) reflection in the *Cmcm* setting] was observed already at 3.2 GPa [Fig. 5.11(b)], indicating a transition from *Pnma* to *Cmcm* [131]. Because, the (121) reflection is forbidden in the *Cmcm* space group. Therefore, our sample displays a structure transition around 3 GPa, which is not compatible with previous reference [131]. This deviation could arise from the different hydrostatic properties of the employed pressure transmitting medium.

5.3.3 Powder Neutron Diffraction under Pressure

Figure 5.12 shows the powder neutron diffraction patterns and their refinements under different pressures. As we can see, the background strongly increases at high pressure due to the gasket crushing and the closure of its hole.

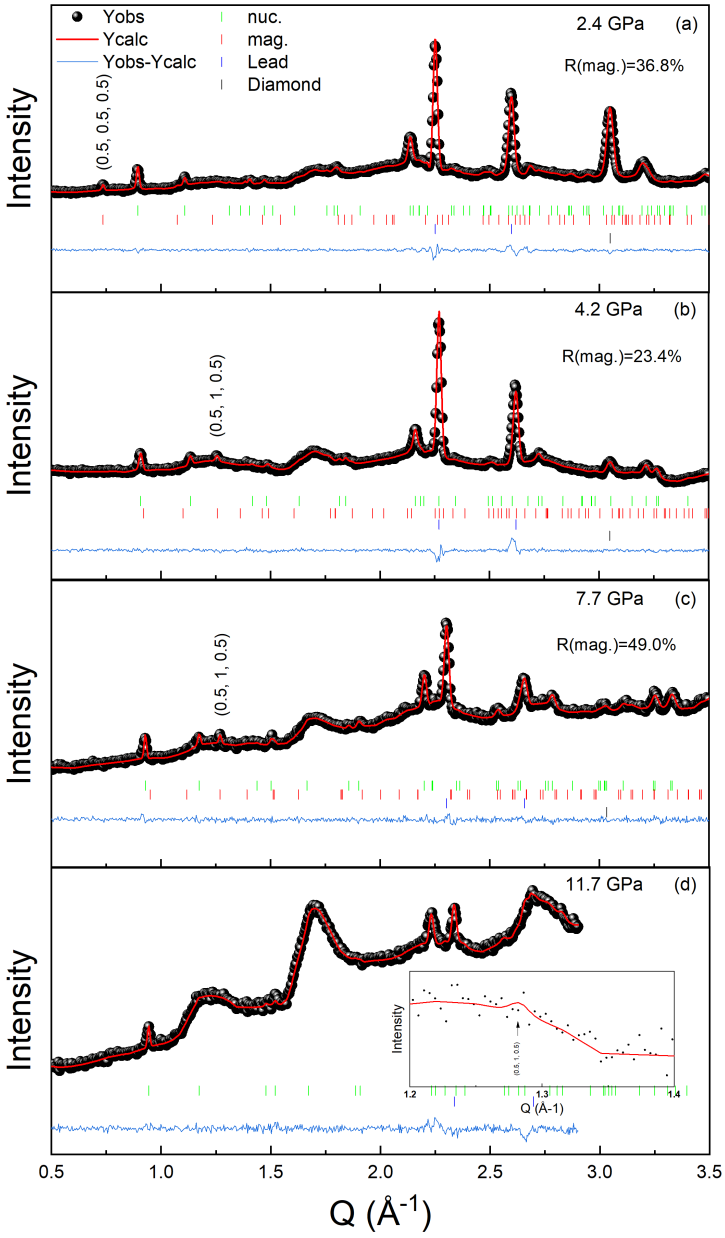

Figure 5.12: Powder neutron diffraction patterns and refinement results under 2.4(a), 4.2(b), 7.7(c), and 11.7(d) GPa. The $(\frac{1}{2}\frac{1}{2}\frac{1}{2})$ magentic peak is observed at $Q \sim 0.73$ Å^{-1} in (a), while the $(\frac{1}{2}1\frac{1}{2})$ peak appears at $Q \sim 1.26$ Å^{-1} in (b) and (c). The inset of (d) shows the fitting pattern with the moment of 1 μ_B at 11.7 GPa.

For the first collection, we recorded a diffractogram for 10 h [Fig. 5.12(a)]. The pressure of 2.4 (±0.4) GPa is determined according to the lattice parameter of lead $a(Pb) = 4.8387(5)$ Å obtained from the refinement. The $(\frac{1}{2}\frac{1}{2}\frac{1}{2})$ magnetic reflection was observed, indicating the appearance of the same Block-A magnetic order as at ambient pressure [Fig. 5.13(a)]. The refinement using the Block-A

model leads to an ordered moment of 1.4 (±0.2) μ_B. Since we have fewer magnetic reflections emerging from the background due to noise coming from the pressure cell, the error bar for the moment's amplitude is larger than the one at ambient pressure.

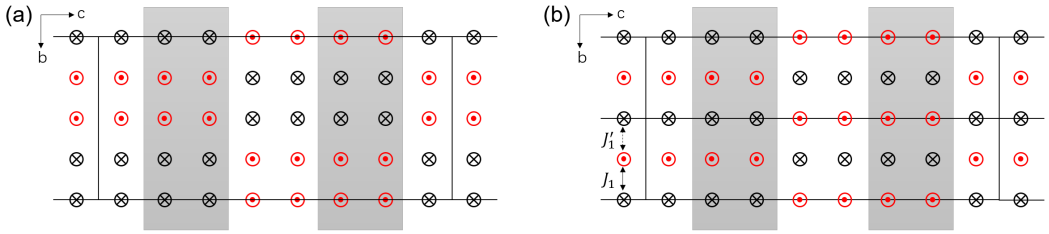

Figure 5.13: (a) and (b) Projections of Fe spins on the bc-planes of the Block-A and CX magnetic orders. The moments are perpendicular to the bc plane. The black lines indicate the edges of the magnetic unit cell. The two Fe ladders are separated by different background colors, white for Ladder-A and grey for Ladder-B.

Neutron diffraction measurements at high pressure are really time-consuming. Moreover, the experimental time in a neutron facility like ILL is limited. Therefore, we were not able to study the temperature evolution at each pressure by accurately collecting a pattern for each temperature. To determine the Néel temperature at each pressure, we repeatedly measured the diffractogram with an interval of 10 min during the heating and cooling processes. Several collections were summed to reduce the background. Indeed, the signal from the sample is proportional to the collection time (t), and the signal from the background is proportional to $\sqrt{t}$. The sums of the scans obtained at 90-110 K and 110-130 K under 2.4 GPa are plotted in Figure 5.14(a). There is no obvious magnetic peak in the latter pattern, while a clear $(\frac{1}{2}\frac{1}{2}\frac{1}{2})$ peak appears in the former one. Therefore, the Néel temperature at 2.4 GPa was estimated to be 110 (±20) K. The decrease of both T_N and the ordered Fe moment at low temperature indicates that the block-like magnetic order is destabilized by the applied pressure. This is not in agreement with the measurements of reference [149], which claimed that the ambient pressure magnetic structure is robust under intermediate pressures.

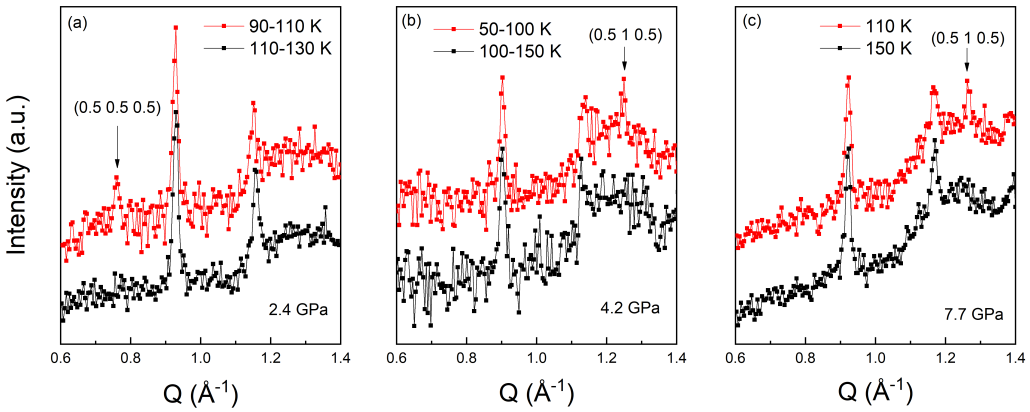

Figure 5.14: The patterns collected below and above the Néel temperatures at 2.4(a), 4.2(b), and 7.7(c) GPa.

At 4.2 (±0.4) GPa, we observed a total loss of intensity on the $(\frac{1}{2}\frac{1}{2}\frac{1}{2})$ magnetic reflection accompanied by the appearance of a new magnetic reflection, indexed by $(\frac{1}{2}1\frac{1}{2})$, as presented in Figure 5.12(b). This observation is the indication of a pressure-induced magnetic transition. Besides, one should notice that the magnetic transition occurs at a pressure very close to the *Pnma* to *Cmcm* structural transition. To determine T_N, the collection time was increased due to the decrease of intensity with pressure, i.e., a larger temperature range of collection was required. We needed to sum the patterns recorded in the temperature range of 50 K to see a clear magnetic peak [Fig. 5.14(b)]. This introduced a higher error bar. Therefore, T_N at 4.2 GPa was determined to be 100 (±50) K. Interestingly,

this pressure-induced magnetic transition was not observed by the authors of [149]. However, their measurement was performed at 6 GPa and 120 K, which is above the critical pressure of 4.2 GPa but still above T_N.

Concerning the magnetic order at 4.2 GPa, it is obvious that the magnetic structure is incompatible with the Block-A magnetic structure. To proceed with the analyse, we first tested various stripe-like models from reference [8]. Except for the CX stripe-like magnetic model, none of them led to a correct fit of the data. The refinement of the pattern with the CX model is shown in Figure 5.12(b). In this CX magnetic structure, each rung of the ladder is constituted of two FM coupled Fe spins directed along a resulting a propagation wave vector of $(0.5, 0, 0.5)$. The rungs are then AFM ordered along the b-axis [Fig. 5.13(b)]. This magnetic order is similar to the ones stabilized in the analogue systems $BaFe_2S_3$[9] and KFe_2S_3[156], except concerning the direction of the moments. In $BaFe_2Se_3$, at least at ambient pressure, a strong spin anisotropy aligns the moments along a as seen in the magnetic susceptibility [127, 134]. However, a reorientation of the spins under pressure is possible as the other compounds of the series present different axial anisotropies. We thus tried different CX stripe models with spins along a, b, and c to adjust our data. The model with moments along a gave the best adjustment (R_{mag}=23.4%, R_{mag}=71.61%, R_{mag}=38.55% for the spins along a, b, and c, respectively) with an ordered magnetic moment on the Fe site of 2.1 (±0.2) μ_B.

Under 7.7 (±0.4) GPa, the results are found to be similar to those at 4.2 GPa. The $(\frac{1}{2}1\frac{1}{2})$ reflection is still observed and confirms the new pressure-induced magnetic phase. The refinement of the experimental data with the same CX model gives an ordered magnetic moment on the Fe of 1.9 (±0.3) μ_B [Fig. 5.12(c)]. For the T_N, we were able to record two patterns at 110 K and 150 K for three hours at each temperature since we had remaining time at the end of the experiment. The $(\frac{1}{2}1\frac{1}{2})$ magnetic reflection is observed at 110 K but not at 150 K [Fig. 5.14(c)], indicating 110 K < T_N < 150 K. Interestingly, T_N at 7.7 GPa seems to be higher than that at 4.2 GPa. Moreover, at 7.7 GPa, the amplitude of the ordered moment at low temperature is comparable to the one at 4.2 GPa. Thus, the CX magnetic order is robust under pressure. However, the ordered moment is considerably smaller than the one expected for a high spin configuration of the Fe^{2+} ions ($4\mu_B$). This result can be explained either by the orbital selective Mott phase scenario or by the modification of the crystal field under pressure leading to $S = 1$, where S is the local moment of the Fe ion [207].

The last pattern was obtained under 11.7 (±0.5) GPa [Fig. 5.12(d)]. At this pressure, no obvious magnetic reflection was detected. However, even if the magnetic phase still exists at this pressure, the magnetic peak will be difficult to detect from the strong background. The inset of Figure 5.12(d) shows the calculated pattern at $(\frac{1}{2}1\frac{1}{2})$ reflection with a Fe moment of 1 μ_B. The peak does not really emerge from the background. Given the accuracy of the measurement, if there is an ordered moment, its maximum amplitude should be 1 μ_B on the Fe ion at this pressure. Therefore, our measurement cannot exclude a magnetic order in the SC phase of $BaFe_2Se_3$.

Table 5.7: The lattice parameters, magnetic moment, $a_i(Pb)$ and magnetic R-factor for each measurement. The pressure values are obtained from $a(Pb)$ by the EOS of Pb.

Pressure (GPa)	a	b	c	m (μ_B)	$a(Pb)$	R_M
2.4(±0.4)	11.3760(6)	5.3863(7)	8.9535(3)	1.4 (±0.2)	4.8387(5)	36.8%
4.2(±0.4)	11.0685(1)	5.3666(7)	8.8618(2)	2.1 (±0.2)	4.7956(5)	23.4%
7.7(±0.4)	10.7005(1)	5.3157(8)	8.7315(3)	1.9 (±0.3)	4.7250(8)	49.0%
11.7(±0.5)	10.7138(7)	5.2691(9)	8.5033(6)	<1	4.6593(3)	-

The refinement results of the patterns at different pressures are summarized in Table 5.7. The lattice parameters are compatible with the results of reference [131]. The pressure dependence of the ordered moment extracted from the neutron patterns is summarized in Figure 5.15(left axis). As we can see, the ordered moment at ambient pressure is below the theoretical 4 μ_B value and decreases

upon the pressure in the *Pnma* and block-type phase. In the *Cmcm* phase, the ordered moment is stable, indicating that the CX magnetic order is robust between 4.2 and 7.7 GPa. Most interestingly, the CX magnetic structure reaches the border of the SC dome, which means that the superconductivity emerges from the CX phase. This is further supported by the fact that our experiment at 11.7 GPa cannot totally exclude the coexistence of a weak CX phase with the superconducting state.

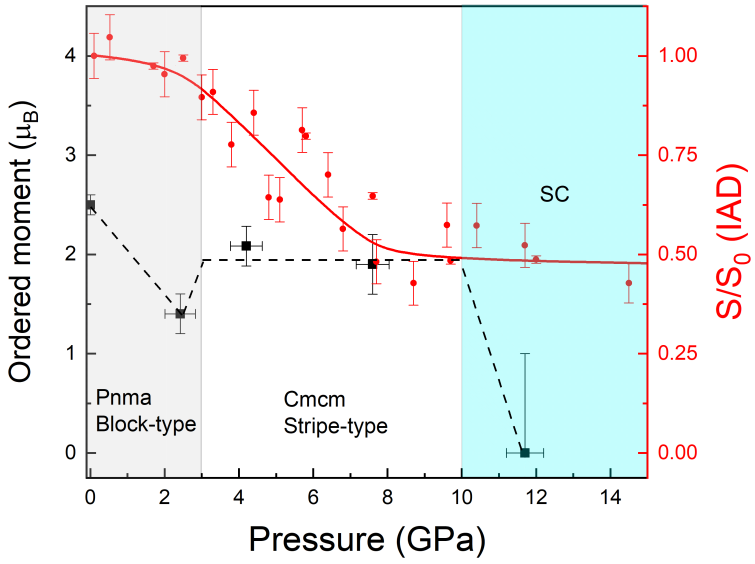

Figure 5.15: Pressure dependence of the ordered moment per Fe from our PND experiments at 3K and the local moments deduced from XES measurements at 300 K. The curve has been built by considering that the S/S$_0$ value of the local moment at ambient pressure should correspond to the theoretical moment value (4 μ_B). The red solid and black dashed lines are guides for the eyes. The large error bar at 11.7 GPa indicates that the possible ordered moment can reach 1 μ_B.

5.3.4 Local Magnetic Moment on the Fe Site

In various systems, the magnetic atoms can carry local moments which do not order or only partly order at low temperatures. It is the case in frustrated magnets [208] and in orbital selective Mott phases [145]. Interestingly, in orbital selective Mott systems, the coexistence of a SC and a magnetic phase is not excluded. So local and ordered magnetic moments are two different parameters that are important to measure both. To probe the local magnetic moment on the Fe site, we performed XES at the Fe K$_\beta$ emission line. The normalized XES spectra at different pressures are shown in Figure 5.16. By the integrated absolute difference analysis, the local moment S was obtained for each pressure. The pressure dependence of S/S$_0$ is shown in Figure 5.15 (right axis), where S$_0$ is the local moment at ambient pressure. We can see that in the *Pnma* phase (between 0 and 3 GPa), the local magnetic moment is roughly constant within the error bars. Above 3 GPa, it undergoes a monotonous decrease up to 8 GPa. This evidenced the influence of the magnetic and structural transition on the local magnetic moment. Besides, around 8 GPa, the amplitude of the ordered moment is closer to the local moment, suggesting that most of the moment participates in the magnetic ordering. Above 8 GPa, close to the SC border, the local moment roughly stabilizes at a non-zero value. The presence of a finite local moment in the SC dome has also been observed in reference [1] in which the local moment only disappears above 30 GPa. This residual local magnetic moment remains available to produce magnetic fluctuations associated with the neighbouring CX magnetic phase which is a potential precursor of the SC phase.

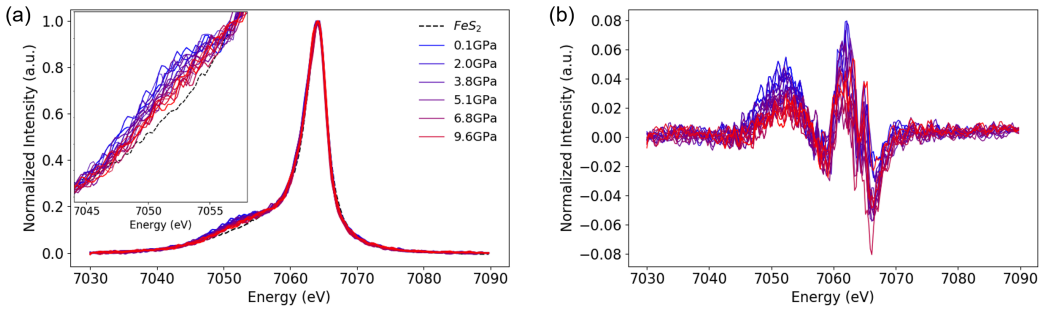

Figure 5.16: (a) Normalized Fe K_β X-ray emission spectroscopy of $BaFe_2Se_3$ at different pressures, together with FeS_2 zero-spin reference from reference [209]. The inset is a zoom around 7050 eV at which the spectra changed. (b) Difference between the XES spectra of $BaFe_2Se_3$ and FeS_2 in (a).

5.3.5 Summary

In this section, we evidenced a transition of the magnetic structure in $BaFe_2Se_3$ as a function of pressure. This transition is likely to be connected to the crystalline transition toward the *Cmcm* structure as it occurs at the same critical pressure of 3 GPa. $BaFe_2Se_3$ adopts then the magnetic order of the parent $BaFe_2S_3$ compound: a magnetic structure characterized by a CX AFM phase with a k=($\frac{1}{2}$, 0, $\frac{1}{2}$) propagation wave vector and a FM order along the ladder rung. The regular AFM order between successive Fe-Fe pairs along the ladder's legs indicates that the J_1 and $J_1^{'}$ exchange couplings become similar (J_1 and $J_1^{'}$ are the two exchange interactions between the nearest-neighbor Fe atoms along the legs) [Fig. 5.13(b)]. This is not surprising because the *Cmcm* symmetry above 3 GPa imposes identical Fe-Fe bonds and Se-Fe-Se angles along the legs of the ladder, and thus strictly identical J_1 and $J_1^{'}$. On the contrary, the $Pmn2_1$ symmetry proposed in Chapter 4 at ambient pressure leads to different bond lengths and Se-Fe-Se angles and a variety of exchange couplings at the origin of the complex block-like magnetic order.

On the other hand, our results are supported by DFT calculations [8]. Despite a disagreement between measured and predicted critical pressure, this theoretical result proved that, from the energy point of view, the CX magnetic phase is close to the ground state with sufficient pressure. Most interestingly, for the parent compound $BaFe_2S_3$, a very similar stripe magnetic order is the ground state at ambient pressure and persists until 10 GPa, at which the superconductivity emerges [9, 10]. $BaFe_2X_3$ (X=Se,S) compounds are expected to present a very similar superconducting mechanism as their crystallographic and magnetic structures are quasi-identical close to the SC phase. In addition, an iso-electronic substitution at the Se site acts as a chemical pressure and should not strongly affect the mechanisms of stabilization of the various ground states within the phase diagram. The stabilization of the universal stripe magnetic phase in pressurised Fe spin ladders is of great interest due to its closeness to the SC dome. Taking into account the state of the art from cuprates and in the current context of the discovery of superconductivity in U-based ferromagnetic materials such as UGe_2 [11] and UCoGe [12], one can foresee the importance of the magnetic fluctuations in the SC mechanism of Fe spin ladders.

Conclusion and Perspective

The main goal of this thesis was to determine the accurate crystallographic and magnetic structures of the quasi-1D antiferromagnet $BaFe_2Se_3$. It consists of Fe ladders in which the Fe blocks are antiferromagnetically coupled along the chain. Superconductivity and multiferroicity have been found to coexist in this compound. This quasi-1D structure makes $BaFe_2Se_3$ a potential candidate in the theoretical study of superconductivity since the solution of the many-body Hamiltonians in two or three dimensions is not precise.

We first studied the crystal structure of $BaFe_2Se_3$ by single-crystal X-ray diffraction. At ambient temperature, the absence of the a glide plane was observed on the reconstruction of the $(hk0)$ plane, indicating that the $Pnma$ space group is no more suitable. Besides, more than 40 forbidden reflections related to the a glide plane were recorded over the 2471 reflections. Although the space group analysis with JANA2006 proposed two space groups ($Pnmm$ and $Pmn2_1$) based on our experimental data, the refinement results confirmed that the $Pmn2_1$ is the correct one. On the other hand, the n glide plane is also absent below the Néel transition (150 K), indicating a transition from $Pmn2_1$ to Pm. The rectangle patterns of the Fe blocks in the $Pmn2_1$ and Pm structures are crucial to understand the polar state and to figure out the block AFM order. Besides, the multiferroic character is indeed attested by the presence of an anomaly at 4 T in the curve of the capacitance as a function of the applied magnetic field, indicating a strong magnetoelectric coupling. Therefore, $BaFe_2Se_3$ can be considered a potential candidate for multiferroic materials.

We then studied the magnetic structure of $BaFe_2Se_3$ at different pressures. At ambient pressure, the C_am magnetic space group has been determined and it derives from the crystal space group Pm. Besides, the Block-A AFM order with a deviation of the magnetic moments from the easy axis a was evidenced at 10 K. The spins were found to tilt towards the apical directions of the Fe-Se tetrahedra and form an umbrella-like shape. Furthermore, the magnetic structure at high pressure was also studied. The block magnetic order persists until 3 GPa and then changes to a stripe-like CX magnetic order. This CX magnetic order is the ground state in a large pressure range from 3 GPa to at least 7.7 GPa. While no evidence of such a phase in the SC phase (11.7 GPa) could be detected, it is difficult to exclude it completely because of the reduced sensitivity inherent to high-pressure experiments. In the vicinity of the SC phase, the presence of magnetic fluctuations is supported by the sudden drop of magnetic order combined with a non-zero local moment in the SC dome.

Based on our studies, the temperature-pressure (P-T) phase diagram of $BaFe_2Se_3$ can be extracted [Fig. 5.17(a)]. As we can see, the block magnetic order is destabilized quickly with the increasing pressure. On the contrary, the stripe CX magnetic order is robust, resembling the stripe AFM order in the parent compound $BaFe_2S_3$ [Fig. 5.17(b)]. Therefore, the magnetic fluctuations which could be involved in the SC mechanism of $BaFe_2X_3$ (X=S,Se) spin ladders, being associated with this universal CX phase, are necessarily located around k=$(\frac{1}{2}, 0, \frac{1}{2})$.

This thesis has highlighted several properties and opened a very large field of exciting investigations on the spin-ladder compound $BaFe_2Se_3$. The first issue concerns the exact crystallographic structure under pressure. This can be done via a new cryostat developed by our team, installed on the CRISTAL beamline of the SOLEIL synchrotron. This cryostat is able to rotate the pressure cells along two

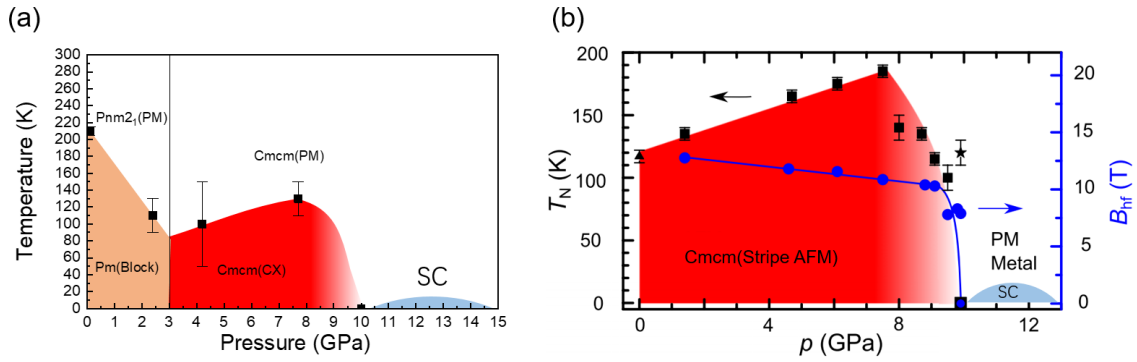

Figure 5.17: (a) Phase diagram of $BaFe_2Se_3$ obtained from our results. (b) Phase diagram of $BaFe_2S_3$ obtained by synchrotron Mössbauer spectroscopy from reference [10]. The left axis represents the Néel temperature while the right axis is the low-temperature magnetic hyperfine field.

axes and thus allows the record of a large number of Bragg reflections, necessary for fine structure refinement.

Another perspective concerns all the doped compounds of the $BaFe_{1-x}M_xB_3$ series, where M can be any metallic ion and B is a chalcogenide. We started this work by doping with M = Ni, Co. The results are still partial but can open a huge field of investigation, which could lead to very interesting properties in terms of superconductivity or in terms of room temperature multiferroicity.

Finally, all the aspect concerning the inelastic properties has not been investigated in the present work. Very original properties are expected. In particular, it would be interesting to study the electromagnon, a hybrid excitation that is still not well understood and specific to magneto-electric systems. It is an electro-active magnetic excitation. Another thesis on this subject is starting in the MATRIX group.

List of Figures

List of Tables

Bibliography

[1] J. Ying, H. Lei, C. Petrovic, et al. "Interplay of Magnetism and Superconductivity in the Compressed Fe-Ladder Compound $BaFe_2S_3$." In: *Phys. Rev. B* 95 (2017), p. 241109. DOI: 10.1103/PhysRevB.95.241109 (cit. on pp. viii, x, xi, 15, 16, 22, 23, 27, 78, 83).

[2] S. Dong, J.-M. Liu, and E. Dagotto. "$BaFe_2Se_3$: A High T_C Magnetic Multiferroic with Large Ferrielectric Polarization." In: *Phys. Rev. Lett.* 113.18 (2014), p. 187204. DOI: 10.1103/PhysRevLett.113.187204 (cit. on pp. viii, x, xi, 6, 15, 16, 24, 25, 57, 63, 65, 77).

[3] H. Hong and H Steinfink. "The crystal chemistry of phases in the Ba-Fe-S and Se systems." In: *J Solid State Chem* 5.1 (1972), pp. 93–104. DOI: 10.1016/0022-4596(72)90015-1 (cit. on pp. viii, x, 16, 17, 26, 56, 63).

[4] J. M. Caron, J. R. Neilson, D. C. Miller, et al. "Iron Displacements and Magnetoelastic Coupling in the Antiferromagnetic Spin-Ladder Compound $BaFe_2Se_3$." In: *Phys. Rev. B* 84 (2011), p. 180409. DOI: 10.1103/PhysRevB.84.180409 (cit. on pp. viii, x, 17, 19, 20, 25, 56, 57, 60, 61, 63, 64, 68, 70, 73).

[5] A Krzton-Maziopa, E Pomjakushina, V Pomjakushin, et al. "The synthesis, and crystal and magnetic structure of the iron selenide $BaFe_2Se_3$ with possible superconductivity at T_C = 11 K." In: *J. Phys. Condens. Matter* 23.40 (2011), p. 402201. DOI: 10.1088/0953-8984/24/5/059502 (cit. on pp. viii, x, 16, 17, 19, 20, 68, 70, 73).

[6] E. Dagotto and T. Rice. "Surprises on the way from one-to two-dimensional quantum magnets: the ladder materials." In: *Science* 271.5249 (1996), pp. 618–623. DOI: 10.1126/science.271.5249.618 (cit. on pp. viii, x).

[7] N. A. Spaldin and M. Fiebig. "The renaissance of magnetoelectric multiferroics." In: *Science* 309.5733 (2005), pp. 391–392. DOI: 10.1126/science.1113357 (cit. on pp. ix, 4).

[8] Y. Zhang, L.-F. Lin, J.-J. Zhang, et al. "Sequential structural and antiferromagnetic transitions in $BaFe_2Se_3$ under pressure." In: *Phys. Rev. B* 97.4 (2018), p. 045119. DOI: 10.1103/PhysRevB.97.045119 (cit. on pp. xii, 18, 21, 22, 68, 82, 84).

[9] H. Takahashi, A. Sugimoto, Y. Nambu, et al. "Pressure-Induced Superconductivity in the Iron-Based Ladder Material $BaFe_2S_3$." In: *Nat. Mater.* 14 (2015), p. 1008. DOI: 10.1038/nmat4351 (cit. on pp. xii, 16, 21, 25, 68, 82, 84).

[10] P. Materne, W. Bi, J. Zhao, et al. "Bandwidth controlled insulator-metal transition in $BaFe_2S_3$: A Mössbauer study under pressure." In: *Phys. Rev. B* 99.2 (2019), p. 020505. DOI: 10.1103/PhysRevB.99.020505 (cit. on pp. xii, xiii, 84, 86).

[11] S. S. Saxena, P. Agarwal, K. Ahilan, et al. "Superconductivity on the border of itinerant-electron ferromagnetism in UGe_2." In: *Nature* 406.6796 (2000), p. 592. DOI: 10.1038/35020500 (cit. on pp. xii, 84).

[12] D. Aoki, K. Ishida, and J. Flouquet. "Review of U-based Ferromagnetic Superconductors: Comparison between UGe_2, URhGe, and UCoGe." In: *J. Phys. Soc. Japan* 88.2 (2019), p. 022001. DOI: 10.7566/JPSJ.88.022001 (cit. on pp. xii, 84).

[13] H. Schmid. "Multi-ferroic magnetoelectrics." In: *Ferroelectrics* 162 (1994), pp. 317–338. DOI: 10.1080/00150199408245120 (cit. on p. 1).

[14] H. Schmid. "On ferrotoroidics and electrotoroidic, magnetotoroidic and piezotoroidic effects." In: *Ferroelectrics* 252 (2001), pp. 41–50. DOI: 10.1080/00150190108016239 (cit. on p. 1).

[15] D. Khomskii. "Classifying Multiferroics: Mechanisms and Effects." In: *Physics* 2 (2009), p. 20. DOI: 10.1103/physics.2.20 (cit. on pp. 2, 3).

[16] M. Fiebig, T. Lottermoser, D. Meier, et al. "The Evolution of Multiferroics." In: *Nat. Rev. Mater.* 1.8 (2016), p. 16046. DOI: 10.1038/natrevmats.2016.46 (cit. on pp. 2, 6).

[17] N. A. Spaldin and R. Ramesh. "Advances in Magnetoelectric Multiferroics." In: *Nat. Mater.* 18.3 (2019), pp. 203–212. DOI: 10.1038/s41563-018-0275-2 (cit. on pp. 2, 4).

[18] T. Lottermoser and D. Meier. "A short history of multiferroics." In: *Physical Sciences Reviews* 6.2 (2021), p. 20200032. DOI: doi:10.1515/psr-2020-0032 (cit. on pp. 2, 3).

[19] G. Lawes and G. Srinivasan. "Introduction to Magnetoelectric Coupling and Multiferroic Films." In: *J. Phys. D: Appl. Phys.* 44.24 (2011-05), p. 243001. DOI: 10.1088/0022-3727/44/24/243001 (cit. on pp. 2, 3).

[20] P. CHANDRA, M. DAWBER, P. B. LITTLEWOOD, et al. "Scaling of the Coercive Field with Thickness in Thin-Film Ferroelectrics." In: *Ferroelectrics* 313.1 (2004), pp. 7–13. DOI: 10.1080/00150190490891157 (cit. on p. 2).

[21] S. Manipatruni, D. E. Nikonov, and I. A. Young. "Beyond CMOS Computing with Spin and Polarization." In: *Nature Phys.* 14.4 (2018), pp. 338–343. DOI: 10.1038/s41567-018-0101-4 (cit. on p. 2).

[22] N. X. Sun and G. Srinivasan. "Voltage control of magnetism in multiferroic heterostructures and devices." In: 2.03 (2012), p. 1240004. DOI: 10.1142/s2010324712400048 (cit. on p. 2).

[23] H. Lin, Y. Gao, X. Wang, et al. "Integrated Magnetics and Multiferroics for Compact and Power-Efficient Sensing, Memory, Power, RF, and Microwave Electronics." In: *IEEE Trans. Magn.* 52.7 (2016), pp. 1–8. DOI: 10.1109/tmag.2016.2514982 (cit. on p. 2).

[24] S. Manipatruni, D. E. Nikonov, C.-C. Lin, et al. "Scalable Energy-Efficient Magnetoelectric Spin–Orbit Logic." In: *Nature* 565.7737 (2019), pp. 35–42. DOI: 10.1038/s41586-018-0770-2 (cit. on p. 2).

[25] H. Schmid. "The Dice - Stone Der Würfelstein: Some Personal Souvenirs Around the Discovery of the First Ferromagnetic Ferroelectric." In: *Ferroelectrics* 427.1 (2012), pp. 1–33. DOI: 10.1080/00150193.2012.673896 (cit. on pp. 2, 3).

[26] G. Smolenskii and V. Ioffe. "Communications de Colloque International de Magnetism de Grenoble (France), 2-6 Jullet." In: *Communications* 71 (1958) (cit. on p. 2).

[27] V. J. Folen, G. T. Rado, and E. W. Stalder. "Anisotropy of the Magnetoelectric Effect in Cr_2O_3." In: *Phys. Rev. Lett.* 6 (11 1961), pp. 607–608. DOI: 10.1016/0038-1098(66)90206-7 (cit. on p. 3).

[28] E. Ascher, H. Rieder, H. Schmid, et al. "Some Properties of Ferromagnetoelectric Nickel-Iodine Boracite, $Ni_3B_7O_{13}I$." In: *J. Appl. Phys.* 37.3 (1966), pp. 1404–1405. DOI: 10.1063/1.1708493 (cit. on p. 3).

[29] G. A. Smolenskiĭ and I. E. Chupis. "Ferroelectromagnets." In: *Soviet Physics Uspekhi* 25.7 (1982), pp. 475–493. DOI: 10.1070/pu1982v025n07abeh004570 (cit. on p. 3).

[30] H. Schmid. "Introduction to the proceedings of the 2nd international conference on magnetoelectric interaction phenomena in crystals, MEIPIC-2." In: *Ferroelectrics* 161.1 (1994), pp. 1–28. DOI: 10.1080/00150199408213348 (cit. on p. 3).

[31] J. Wang, J. B. Neaton, H. Zheng, et al. "Epitaxial $BiFeO_3$ Multiferroic Thin Film Heterostructures." In: *Science* 299.5613 (2003), pp. 1719–1722. DOI: 10.1126/science.1080615 (cit. on p. 3).

[32] T. Kimura, T. Goto, H. Shintani, et al. "Magnetic Control of Ferroelectric Polarization." In: *Nature* 426.6962 (2003), pp. 55–58. DOI: 10.1038/nature02018 (cit. on pp. 3, 6).

[33] W. Eerenstein, N. Mathur, and J. F. Scott. "Multiferroic and magnetoelectric materials." In: *nature* 442.7104 (2006), pp. 759–765. DOI: 10.1038/nature05023 (cit. on p. 4).

[34] M. Fiebig. "Revival of the magnetoelectric effect." In: *J PHYS D APPL PHYS* 38.8 (2005), R123. DOI: 10.1088/0022-3727/38/8/R01 (cit. on p. 4).

[35] J Van den Boomgaard, D. Terrell, R. Born, et al. "An in situ grown eutectic magnetoelectric composite material." In: *J. Mater. Sci.* 9.10 (1974), pp. 1705–1709. DOI: 10.1007/BF00540770 (cit. on p. 4).

[36] J Van Suchtelen. "Product properties: a new application of composite materials." In: *Phillips Research Reports* 27 (1972), pp. 28–37 (cit. on p. 4).

[37] M. Bichurin, V. Petrov, and G Srinivasan. "Theory of low-frequency magnetoelectric coupling in magnetostrictive-piezoelectric bilayers." In: *Phys. Rev. B* 68.5 (2003), p. 054402. DOI: 10.1103/PhysRevB.68.054402 (cit. on p. 4).

[38] J. A. Mundy, C. M. Brooks, M. E. Holtz, et al. "Atomically engineered ferroic layers yield a room-temperature magnetoelectric multiferroic." In: *Nature* 537.7621 (2016), pp. 523–527. DOI: 10.1038/nature19343 (cit. on p. 4).

[39] R. E. Cohen and H. Krakauer. "Electronic structure studies of the differences in ferroelectric behavior of $BaTiO_3$ and $PbTiO_3$." In: *Ferroelectrics* 136.1 (1992), pp. 65–83. DOI: 10.1080/00150199208016067 (cit. on p. 4).

[40] N. A. Hill. "Why Are There so Few Magnetic Ferroelectrics?" In: *J. Phys. Chem. B* 104.29 (2000), pp. 6694–6709. DOI: 10.1021/jp000114x (cit. on p. 4).

[41] S.-W. Cheong and M. Mostovoy. "Multiferroics: A Magnetic Twist for Ferroelectricity." In: *Nature Mater* 6.1 (2007), pp. 13–20. DOI: 10.1038/nmat1804 (cit. on pp. 5, 6).

[42] T. Katsufuji, S Mori, M Masaki, et al. "Dielectric and magnetic anomalies and spin frustration in hexagonal $RMnO_3$ (R= Y, Yb, and Lu)." In: *Phys. Rev. B* 64.10 (2001), p. 104419. DOI: 10.1103/PhysRevB.64.104419 (cit. on p. 5).

[43] B. B. Van Aken, T. T. Palstra, A. Filippetti, et al. "The origin of ferroelectricity in magnetoelectric $YMnO_3$." In: *Nat. Mater.* 3.3 (2004), pp. 164–170. DOI: 10.1038/nmat1080 (cit. on p. 5).

[44] C. J. Fennie and K. M. Rabe. "Ferroelectric transition in $YMnO_3$ from first principles." In: *Phys. Rev. B* 72.10 (2005), p. 100103. DOI: 10.1103/PhysRevB.72.100103 (cit. on p. 5).

[45] E. Bousquet, M. Dawber, N. Stucki, et al. "Improper ferroelectricity in perovskite oxide artificial superlattices." In: *Nature* 452.7188 (2008), pp. 732–736. DOI: 10.1038/nature06817 (cit. on p. 5).

[46] N. A. Benedek and C. J. Fennie. "Hybrid improper ferroelectricity: a mechanism for controllable polarization-magnetization coupling." In: *Phys. Rev. Lett.* 106.10 (2011), p. 107204. DOI: 10.1103/physrevlett.106.107204 (cit. on p. 5).

[47] N. A. Benedek, J. M. Rondinelli, H. Djani, et al. "Understanding ferroelectricity in layered perovskites: new ideas and insights from theory and experiments." In: *Dalton Transactions* 44.23 (2015), pp. 10543–10558. DOI: 10.1039/c5dt00010f (cit. on p. 5).

[48] N. Ikeda, H. Ohsumi, K. Ohwada, et al. "Ferroelectricity from iron valence ordering in the charge-frustrated system $LuFe_2O_4$." In: *Nature* 436.7054 (2005), pp. 1136–1138. DOI: 10.1038/nature04039 (cit. on p. 5).

[49] J. d. de Groot, T Mueller, R. Rosenberg, et al. "Charge order in $LuFe_2O_4$: an unlikely route to ferroelectricity." In: *Phys. Rev. Lett.* 108.18 (2012), p. 187601. DOI: 10.1103/physrevlett.108.187601 (cit. on p. 5).

[50] M. S. Senn, J. P. Wright, and J. P. Attfield. "Charge order and three-site distortions in the Verwey structure of magnetite." In: *Nature* 481.7380 (2012), pp. 173–176. DOI: 10.1038/nature10704 (cit. on p. 5).

[51] S. Ren and M. Wuttig. "Organic exciton multiferroics." In: *Adv. Mater.* 24.6 (2012), pp. 724–727. DOI: 10.1002/adma.201104250 (cit. on p. 5).

[52] A. Stroppa, P. Barone, P. Jain, et al. "Hybrid Improper Ferroelectricity in a Multiferroic and Magnetoelectric Metal-Organic Framework." In: *Adv. Mater.* 25.16 (2013), pp. 2284–2290. DOI: 10.1002/adma.201204738 (cit. on p. 5).

[53] W. Qin, B. Xu, and S. Ren. "An organic approach for nanostructured multiferroics." In: *Nanoscale* 7.20 (2015), pp. 9122–9132. DOI: 10.1039/c5nr01435b (cit. on p. 5).

[54] K. Z. Rushchanskii, S. Kamba, V. Goian, et al. "A Multiferroic Material to Search for the Permanent Electric Dipole Moment of the Electron." In: *Nat. Mater.* 9.8 (2010-08), pp. 649–654. DOI: 10.1038/nmat2799 (cit. on p. 5).

[55] J. H. Lee, L. Fang, E. Vlahos, et al. "A Strong Ferroelectric Ferromagnet Created by Means of Spin–Lattice Coupling." In: *Nature* 466.7309 (2010), pp. 954–958. DOI: 10.1038/nature09331 (cit. on p. 5).

[56] J. H. Lee and K. M. Rabe. "Epitaxial-strain-induced multiferroicity in $SrMnO_3$ from first principles." In: *Phys. Rev. Lett.* 104.20 (2010), p. 207204. DOI: 10.1103/physrevlett.104.207204 (cit. on p. 5).

[57] J. M. Rondinelli, A. S. Eidelson, and N. A. Spaldin. "Non-d^0 Mn-driven ferroelectricity in antiferromagnetic $BaMnO_3$." In: *Phys. Rev. B* 79.20 (2009), p. 205119. DOI: 10.1103/physrevb.79.205119 (cit. on p. 5).

[58] H Sakai, J Fujioka, T Fukuda, et al. "Displacement-type ferroelectricity with off-center magnetic ions in perovskite $Sr_{1-x}Ba_xMnO_3$." In: *Phys. Rev. Lett.* 107.13 (2011), p. 137601. DOI: 10.1103/physrevlett.107.137601 (cit. on p. 5).

[59] R. E. Newnham, J. Kramer, W. Schulze, et al. "Magnetoferroelectricity in Cr_2BeO_4." In: *J. Appl. Phys.* 49.12 (1978), pp. 6088–6091. DOI: 10.1063/1.324527 (cit. on p. 6).

[60] H. Katsura, N. Nagaosa, and A. V. Balatsky. "Spin current and magnetoelectric effect in noncollinear magnets." In: *Phys. Rev. Lett.* 95.5 (2005), p. 057205. DOI: 10.1103/PhysRevLett.95.057205 (cit. on p. 6).

[61] M. Mostovoy. "Ferroelectricity in spiral magnets." In: *Phys. Rev. Lett.* 96.6 (2006), p. 067601. DOI: 10.1103/PhysRevLett.96.067601 (cit. on pp. 6, 24).

[62] Y. Choi, H. Yi, S Lee, et al. "Ferroelectricity in an Ising chain magnet." In: *Phys. Rev. Lett.* 100.4 (2008), p. 047601. DOI: 10.1103/PhysRevLett.100.047601 (cit. on p. 6).

[63] N. Hur, S. Park, P. A. Sharma, et al. "Electric Polarization Reversal and Memory in a Multiferroic Material Induced by Magnetic Fields." In: *Nature* 429.6990 (2004), pp. 392–395. DOI: 10.1038/nature02572 (cit. on p. 6).

[64] T.-h. Arima. "Ferroelectricity induced by proper-screw type magnetic order." In: *J. Phys. Soc. Japan* 76.7 (2007), pp. 073702–073702. DOI: 10.1143/JPSJ.76.073702 (cit. on p. 6).

[65] D. K. Pradhan, V. S. Puli, S. Kumari, et al. "Studies of phase transitions and magnetoelectric coupling in PFN-CZFO multiferroic composites." In: *J. Phys. Chem. C* 120.3 (2016), pp. 1936–1944. DOI: 10.1021/acs.jpcc.5b10422 (cit. on p. 6).

[66] J.-M. Hu, C.-G. Duan, C.-W. Nan, et al. "Understanding and designing magnetoelectric heterostructures guided by computation: progresses, remaining questions, and perspectives." In: *NPJ Comput. Mater.* 3.1 (2017), pp. 1–21. DOI: 10.1038/s41524-017-0020-4 (cit. on p. 6).

[67] D. K. Pradhan, S. Kumari, and P. D. Rack. "Magnetoelectric composites: applications, coupling mechanisms, and future directions." In: *Nanomaterials* 10.10 (2020), p. 2072. DOI: 10.3390/nano10102072 (cit. on p. 6).

[68] C. A. F. Vaz and U. Staub. "Artificial multiferroic heterostructures." In: *J. Mater. Chem. C* 1.41 (2013), pp. 6731–6742. DOI: 10.1039/c3tc31428f (cit. on p. 7).

[69] R. Johnson, L. Chapon, D. Khalyavin, et al. "Giant improper ferroelectricity in the ferroaxial magnet $CaMn_7O_{12}$." In: *Phys. Rev. Lett.* 108.6 (2012), p. 067201. DOI: 10.1103/PhysRevLett.108.067201 (cit. on p. 7).

[70] T Aoyama, K Yamauchi, A Iyama, et al. "Giant spin-driven ferroelectric polarization in $TbMnO_3$ under high pressure." In: *Nat. Commun.* 5.1 (2014), pp. 1–7. DOI: 10.1038/ncomms5927 (cit. on p. 7).

[71] X. Rocquefelte, K. Schwarz, P. Blaha, et al. "Room-temperature spin-spiral multiferroicity in high-pressure cupric oxide." In: *Nat. Commun.* 4.1 (2013), pp. 1–7. DOI: 10.1038/ncomms3511 (cit. on p. 7).

[72] D. Van Delft and P. Kes. "The discovery of superconductivity." In: *Phys. Today* 63.9 (2010), pp. 38–43. DOI: 10.1063/1.3490499 (cit. on pp. 7, 8).

[73] R. de Bruyn Ouboter. "Heike Kamerlingh Onnes's discovery of superconductivity." In: *Sci. Am.* 276.3 (1997), pp. 98–103. DOI: 10.1038/scientificamerican0397-98 (cit. on p. 8).

[74] C. Buzea and K. Robbie. "Assembling the puzzle of superconducting elements: a review." In: *Supercond Sci Technol* 18.1 (2004), R1. DOI: 10.1088/0953-2048/18/1/R01 (cit. on p. 8).

[75] J. Schmalian. "Failed theories of superconductivity." In: *Mod Phys Lett B* 24.27 (2010), pp. 2679–2691. DOI: 10.1142/S0217984910025280 (cit. on p. 8).

[76] W. Meissner and R. Ochsenfeld. "Ein neuer Effekt bei Eintritt der Supraleitfähigkeit." In: *Naturwissenschaften* 21.44 (1933), pp. 787–788. DOI: 10.1007/BF01504252 (cit. on p. 9).

[77] F. London and H. London. "The electromagnetic equations of the supraconductor." In: *Proceedings of the Royal Society of London. Series A-Mathematical and Physical Sciences* 149.866 (1935), pp. 71–88. DOI: 10.1098/rspa.1935.0048 (cit. on p. 9).

[78] S. J. Blundell. *Superconductivity: a very short introduction*. OUP Oxford, 2009 (cit. on p. 9).

[79] F. London. *Superfluids: Macroscopic Theory of Superconductivity*. Structure of Matter Series. Wiley, 1950. DOI: 10.1126/science.113.2938.447 (cit. on p. 9).

[80] H. Fröhlich. "Isotope effect in superconductivity." In: *Proceedings of the Physical Society. Section A* 63.7 (1950), p. 778. DOI: 10.1103/PhysRevLett.11.114 (cit. on p. 9).

[81] H. Fröhlich. "Theory of the superconducting state. I. The ground state at the absolute zero of temperature." In: *Phys. Rev.* 79.5 (1950), p. 845. DOI: 10.1103/PhysRev.79.845 (cit. on p. 9).

[82] E. Maxwell. "Isotope effect in the superconductivity of mercury." In: *Phys. Rev.* 78.4 (1950), p. 477. DOI: 10.1103/PhysRev.78.477 (cit. on p. 9).

[83] C. Reynolds, B Serin, W. Wright, et al. "Superconductivity of isotopes of mercury." In: *Phys. Rev.* 78.4 (1950), p. 487. DOI: 10.1103/PhysRev.78.487 (cit. on p. 9).

[84] C. A. Reynolds, B. Serin, and L. B. Nesbitt. "The Isotope Effect in Superconductivity. I. Mercury." In: *Phys. Rev.* 84 (4 1951), pp. 691–694. DOI: 10.1103/PhysRev.84.691 (cit. on p. 9).

[85] J. Bardeen, L. N. Cooper, and J. R. Schrieffer. "Microscopic Theory of Superconductivity." In: *Phys. Rev.* 106.1 (1957), pp. 162–164. DOI: 10.1103/PhysRev.106.162 (cit. on p. 9).

[86] L. N. Cooper. "Bound electron pairs in a degenerate Fermi gas." In: *Phys. Rev.* 104.4 (1956), p. 1189. DOI: 10.1103/PhysRev.104.1189 (cit. on p. 10).

[87] N. W. Ashcroft, N. D. Mermin, et al. *Solid state physics*. 1976 (cit. on p. 10).

[88] J. G. Bednorz and K. A. Müller. "Possible high T_c superconductivity in the Ba-La-Cu-O system." In: *Zeitschrift fur Physik B Condensed Matter* 64 (1986), pp. 189–193. DOI: 10.1007/BF01303701 (cit. on pp. 10, 11).

[89] M. K. Wu, J. R. Ashburn, C. J. Torng, et al. "Superconductivity at 93 K in a new mixed-phase Y-Ba-Cu-O compound system at ambient pressure." In: *Phys. Rev. Lett.* 58 (9 1987), pp. 908–910. DOI: 10.1103/PhysRevLett.58.908 (cit. on p. 10).

[90] J. G. Bednorz and K. A. Müller. "Perovskite-type oxides—The new approach to high-T_C superconductivity." In: *Rev. Mod. Phys.* 60.3 (1988), p. 585. DOI: 10.1103/RevModPhys.60.585 (cit. on p. 10).

[91] P. J. Ray. "Structural investigation of $La_{2-x}Sr_xCuO_{4+y}$." PhD thesis. Master's thesis (University of Copenhagen, 2015), 2015 (cit. on pp. 10, 11, 39, 47).

[92] G. Saito and Y. Yoshida. "Organic superconductors." In: *The Chemical Record* 11.3 (2011), pp. 124–145. DOI: 10.1002/tcr.201000039 (cit. on p. 10).

[93] B. White, J. Thompson, and M. Maple. "Unconventional superconductivity in heavy-fermion compounds." In: *Physica C: superconductivity and its applications* 514 (2015), pp. 246–278. DOI: 10.1016/j.physc.2015.02.044 (cit. on p. 11).

[94] G. R. Stewart. "Superconductivity in Iron Compounds." In: *Rev. Mod. Phys.* 83 (2011), pp. 1589–1652. DOI: 10.1103/RevModPhys.83.1589 (cit. on pp. 11, 12).

[95] A. J. Leggett. "What DO we know about high T_C?" In: *Nature Physics* 2.3 (2006), pp. 134–136. DOI: 10.1038/nphys254 (cit. on p. 11).

[96] A. Drozdov, M. Eremets, I. Troyan, et al. "Conventional superconductivity at 203 kelvin at high pressures in the sulfur hydride system." In: *Nature* 525.7567 (2015), pp. 73–76. DOI: 10.1038/nature14964 (cit. on p. 11).

[97] C. Chu, P. Hor, R. Meng, et al. "Evidence for superconductivity above 40 K in the La-Ba-Cu-O compound system." In: *Phys. Rev. Lett.* 58.4 (1987), p. 405. DOI: 10.1103/PhysRevLett.58.405 (cit. on p. 11).

[98] N. Plakida. *High-temperature cuprate superconductors: Experiment, theory, and applications*. Vol. 166. Springer Science & Business Media, 2010 (cit. on pp. 11, 12).

[99] M. Presland, J. Tallon, R. Buckley, et al. "General trends in oxygen stoichiometry effects on T_C in Bi and Tl superconductors." In: *Physica C: Superconductivity* 176.1-3 (1991), pp. 95–105. DOI: 10.1016/0921-4534(91)90700-9 (cit. on p. 11).

[100] G.-m. Zhao, H Keller, and K Conder. "Unconventional isotope effects in the high-temperature cuprate superconductors." In: *J. Phys. Condens. Matter* 13.29 (2001), R569. DOI: 10.1088/0953-8984/13/29/202 (cit. on p. 12).

[101] M Cyrot. "A possible origin for heavy fermion superconductivity." In: *Solid state communications* 60.3 (1986), pp. 253–256. DOI: 10.1016/0038-1098(86)90458-8 (cit. on p. 12).

[102] K Miyake, S Schmitt-Rink, and C. Varma. "Spin-fluctuation-mediated even-parity pairing in heavy-fermion superconductors." In: *Phys. Rev. B* 34.9 (1986), p. 6554. DOI: 10.1103/PhysRevB.34.6554 (cit. on p. 12).

[103] C. Tsuei, J. R. Kirtley, C. Chi, et al. "Pairing Symmetry and Flux Quantization in a Tricrystal Superconducting Ring of $YBa_2Cu_3O_{7-\delta}$." In: *Phys. Rev. Lett.* 73.4 (1994), p. 593. DOI: 10.1103/PhysRevLett.73.593 (cit. on p. 12).

[104] D. J. Scalapino. "The case for $d_{x^2-y^2}$ pairing in the cuprate superconductors." In: *Phys. Rep.* 250.6 (1995), pp. 329–365. DOI: 10.1016/0370-1573(94)00086-I (cit. on p. 12).

[105] N Bulut. "$d_{x^2-y^2}$ superconductivity and the hubbard model." In: *Advances in Physics* 51.7 (2002), pp. 1587–1667. DOI: 10.1080/00018730210155142 (cit. on p. 12).

[106] M. Rice and Y. Wang. "Spin-charge separation and superconductivity from the t-J model." In: *Phys. Rev. B* 48.17 (1993), p. 12921. DOI: 10.1103/PhysRevB.48.12921 (cit. on p. 12).

[107] J. Tranquada, B. Sternlieb, J. Axe, et al. "Evidence for stripe correlations of spins and holes in copper oxide superconductors." In: *nature* 375.6532 (1995), pp. 561–563. DOI: 10.1038/375561a0 (cit. on p. 12).

[108] T Jarlborg. "Theoretical aspects of simple and nested Fermi surfaces for superconductivity in doped semiconductors and high-T_C cuprates." In: *Solid state communications* 181 (2014), pp. 15–19. DOI: 10.1016/j.ssc.2013.11.030 (cit. on p. 12).

[109] B. Chandrasekhar and J. Hulm. "The electrical resistivity and super-conductivity of some uranium alloys and compounds." In: *J Phys Chem Solids* 7.2-3 (1958), pp. 259–267. DOI: 10.1016/0022-3697(58)90271-3 (cit. on p. 12).

[110] B. Matthias, V. Compton, and E Corenzwit. "Some new superconducting compounds." In: *J Phys Chem Solids* 19.1-2 (1961), pp. 130–133. DOI: 10.1016/0022-3697(61)90066-X (cit. on p. 12).

[111] H. F. Braun. "Superconductivity of rare earth-iron silicides." In: *Physics Letters A* 75.5 (1980), pp. 386–388. DOI: Superconductivityofrareearth-ironsilicides (cit. on p. 12).

[112] A. W. Graham, M. Kurmoo, and P. Day. "β''-(bedt-ttf)$_4$ [$(H_2O)Fe(C_2O_4)_3$]· PhCN: the first molecular superconductor containing paramagnetic metal ions." In: *J. Chem. Soc., Chem. commun.* 20 (1995), pp. 2061–2062. DOI: 10.1039/c39950002061 (cit. on p. 12).

[113] Y. Kamihara, H. Hiramatsu, M. Hirano, et al. "Iron-based layered superconductor: LaOFeP." In: *J. Am. Chem. Soc.* 128.31 (2006), pp. 10012–10013. DOI: 10.1021/ja063355c (cit. on p. 12).

[114] Y. Kamihara, T. Watanabe, M. Hirano, et al. "Iron-Based Layered Superconductor La[$O_{1-x}F_x$]FeAs ($x = 0.05 - 0.12$) with $T_c = 26$ K." In: *J. Am. Chem. Soc.* 130 (2008), pp. 3296–3297. DOI: 10.1021/ja800073m (cit. on pp. 12, 16).

[115] J. Paglione and R. L. Greene. "High-Temperature Superconductivity in Iron-Based Materials." In: *Nat. Phys.* 6 (2010), pp. 645–658. DOI: 10.1038/nphys1759 (cit. on pp. 12, 13).

[116] M. Rotter, M. Tegel, and D. Johrendt. "Superconductivity at 38 K in the Iron Arsenide ($Ba_{1-x}K_x$)Fe_2As_2." In: *Phys. Rev. Lett.* 101.10 (2008), p. 107006. DOI: 10.1103/PhysRevLett.101.107006 (cit. on p. 12).

[117] X. Wang, Q. Liu, Y. Lv, et al. "The Superconductivity at 18 K in LiFeAs System." In: *Solid State Commun.* 148.11-12 (2008), pp. 538–540. DOI: 10.1016/j.ssc.2008.09.057 (cit. on p. 12).

[118] F.-C. Hsu, J.-Y. Luo, K.-W. Yeh, et al. "Superconductivity in the PbO-Type Structure α-FeSe." In: *PNAS* 105 (2008), p. 14262. DOI: 10.1073/pnas.0807325105 (cit. on p. 12).

[119] H. Ogino, Y. Matsumura, Y. Katsura, et al. "Superconductivity at 17 K in (Fe_2P_2)($Sr_4Sc_2O_6$): A New Superconducting Layered Pnictide Oxide with a Thick Perovskite Oxide Layer." In: *Supercond. Sci. Technol.* 22 (2009), p. 075008. DOI: 10.1088/0953-2048/22/7/075008 (cit. on p. 12).

[120] A. L. Ivanovskii. "New superconductors based on five-component transition metal oxypnictides." In: *Russ. Chem. Rev.* 79.1 (2010), p. 1. DOI: 10.1070/rc2010v079n01abeh004088 (cit. on p. 12).

[121] W. Bao, Q.-Z. Huang, G.-F. Chen, et al. "A Novel Large Moment Antiferromagnetic Order in $K_{0.8}Fe_{1.6}Se_2$ Superconductor." In: *Chinese Phys. Lett.* 28.8 (2011), p. 086104. DOI: 10.1088/0256-307X/28/8/086104 (cit. on pp. 12, 21).

[122] I. Mazin, D. J. Singh, s. M. Johannes, et al. "Unconventional superconductivity with a sign reversal in the order parameter of $LaFeAsO_{1-x}F_x$." In: *Phys. Rev. Lett.* 101.5 (2008), p. 057003. DOI: 10.1103/PhysRevLett.101.057003 (cit. on p. 14).

[123] I. Mazin. "Iron Superconductivity Weathers Another Storm." In: *Physics* 4 (2011), p. 26. DOI: 10.1103/Physics.4.26 (cit. on p. 14).

[124] T. Nagata, M. Uehara, J. Goto, et al. "Pressure-Induced Dimensional Crossover and Superconductivity in the Hole-Doped Two-Leg Ladder Compound $Sr_{14-x}Ca_xCu_{24}O_{41}$." In: *Phys. Rev. Lett.* 81.5 (1998), p. 1090. DOI: 10.1103/PhysRevLett.81.1090 (cit. on p. 16).

[125] T Vuletić, B Korin-Hamzić, T Ivek, et al. "The spin-ladder and spin-chain system (La, Y, Sr, Ca)$_{14}Cu_{24}O_{41}$: Electronic phases, charge and spin dynamics." In: *Phys. Rep.* 428.4 (2006), pp. 169–258. DOI: 10.1016/j.physrep.2006.01.005 (cit. on p. 16).

[126] B. Saparov, S. Calder, B. Sipos, et al. "Spin glass and semiconducting behavior in one-dimensional $BaFe_{2-\delta}Se_3(\delta \approx 0.2)$ crystals." In: *Phys. Rev. B* 84.24 (2011), p. 245132. DOI: 10.1103/PhysRevB.84.245132 (cit. on pp. 17, 23, 28, 29, 56, 65).

[127] X. Liu, C. Ma, C. Hou, et al. "Structural, magnetic and dielectric properties of $BaFe_2Se_3$ crystals." In: *EPL (Europhysics Letters)* 126.2 (2019), p. 27005. DOI: 10.1209/0295-5075/126/27005 (cit. on pp. 17, 19, 23, 24, 56, 65, 69, 82).

[128] J. Gao, Y. Teng, W. Liu, et al. "The synthesis and magnetic properties of $BaFe_2Se_3$ single crystals." In: *RSC Advances* 7.48 (2017), pp. 30433–30438. DOI: 10.1039/c7ra03031b (cit. on pp. 17, 29, 56).

[129] V Svitlyk, D Chernyshov, E Pomjakushina, et al. "Crystal structure of $BaFe_2Se_3$ as a function of temperature and pressure: phase transition phenomena and high-order expansion of Landau potential." In: *J. Phys. Condens. Matter* 25.31 (2013), p. 315403. DOI: 10.1088/0953-8984/25/31/315403 (cit. on pp. 17, 18, 60).

[130] T. Aoyama, S. Imaizumi, T. Togashi, et al. "Polar state induced by block-type lattice distortions in $BaFe_2Se_3$ with quasi-one-dimensional ladder structure." In: *Phys. Rev. B* 99.24 (2019), p. 241109. DOI: 10.1103/PhysRevB.99.241109 (cit. on pp. 17, 25, 57, 61).

[131] V Svitlyk, G Garbarino, A. Rosa, et al. "High-pressure polymorphism of $BaFe_2Se_3$." In: *J. Phys. Condens. Matter* 31.8 (2019), p. 085401. DOI: 10.1088/1361-648X/aaf777 (cit. on pp. 18, 60, 79, 82).

[132] C. Kittel. *Introduction to Solid State Physics, sec. ed.* 1956 (cit. on p. 19).

[133] Y. Nambu, K. Ohgushi, S. Suzuki, et al. "Block magnetism coupled with local distortion in the iron-based spin-ladder compound $BaFe_2Se_3$." In: *Phys. Rev. B* 85.6 (2012), p. 064413. DOI: 10.1103/PhysRevB.85.064413 (cit. on pp. 19, 20, 23, 28, 56, 57, 60, 63, 65, 68, 70).

[134] H. Lei, H. Ryu, A. I. Frenkel, et al. "Anisotropy in $BaFe_2Se_3$ single crystals with double chains of FeSe tetrahedra." In: *Phys. Rev. B* 84.21 (2011), p. 214511. DOI: 10.1103/PhysRevB.84.214511 (cit. on pp. 19, 23, 55, 56, 65, 69, 82).

[135] Q. Luo, A. Nicholson, J. Rincón, et al. "Magnetic states of the two-leg-ladder alkali metal iron selenides AFe_2Se_3." In: *Phys. Rev. B* 87.2 (2013), p. 024404. DOI: 10.1103/PhysRevB.87.024404 (cit. on pp. 20, 68).

[136] A Krzton-Maziopa, E Pomjakushina, V Pomjakushin, et al. "The synthesis, and crystal and magnetic structure of the iron selenide BaFe2Se3with possible superconductivity atTc= 11 K." In: *J. Phys. Condens. Matter* 24.5 (2012), p. 059502. DOI: 10.1088/0953-8984/24/5/059502 (cit. on p. 20).

[137] M. Wang, C. Fang, D.-X. Yao, et al. "Spin waves and magnetic exchange interactions in insulating $Rb_{0.89}Fe_{1.58}Se_2$." In: *Nat. Commun.* 2.1 (2011), pp. 1–6. DOI: 10.1038/ncomms1573 (cit. on p. 21).

[138] Y.-Z. You, H. Yao, and D.-H. Lee. "Spin excitations of the block-antiferromagnetic state in $K_{0.8}Fe_{1.6}Se_2$." In: *Phys. Rev. B* 84.2 (2011), p. 020406. DOI: 10.1103/PhysRevB.84.020406 (cit. on p. 21).

[139] R. Yu and Q. Si. "Orbital-selective Mott phase in multiorbital models for alkaline iron selenides $K_{1-x}Fe_{2-y}Se_2$." In: *Phys. Rev. Lett.* 110.14 (2013), p. 146402. DOI: 10.1103/PhysRevLett.110.146402 (cit. on p. 21).

[140] J. Rincón, A. Moreo, G. Alvarez, et al. "Exotic Magnetic Order in the Orbital-Selective Mott Regime of Multiorbital Systems." In: *Phys. Rev. Lett.* 112 (10 2014), p. 106405. DOI: 10.1103/PhysRevLett.112.106405 (cit. on p. 21).

[141] A Liebsch. "Single Mott transition in the multiorbital Hubbard model." In: *Phys. Rev. B* 70.16 (2004), p. 165103. DOI: 10.1103/PhysRevB.70.165103 (cit. on p. 21).

[142] S Biermann, L de'Medici, and A Georges. "Non-fermi-liquid behavior and double-exchange physics in orbital-selective mott systems." In: *Phys. Rev. Lett.* 95.20 (2005), p. 206401. DOI: 10.1103/PhysRevLett.95.206401 (cit. on p. 21).

[143] L. de'Medici, S. R. Hassan, M. Capone, et al. "Orbital-selective Mott transition out of band degeneracy lifting." In: *Phys. Rev. Lett.* 102.12 (2009), p. 126401. DOI: 10.1103/PhysRevLett.102.126401 (cit. on p. 21).

[144] M Mourigal, S. Wu, M. Stone, et al. "Block magnetic excitations in the orbitally selective Mott insulator $BaFe_2Se_3$." In: *Phys. Rev. Lett.* 115.4 (2015), p. 047401. DOI: 10.1103/PhysRevLett.115.047401 (cit. on pp. 21, 56).

[145] J Herbrych, N. Kaushal, A. Nocera, et al. "Spin dynamics of the block orbital-selective Mott phase." In: *Nat. Commun.* 9.1 (2018), pp. 1–10. DOI: 10.1038/s41467-018-06181-6 (cit. on pp. 21, 83).

[146] J Herbrych, J Heverhagen, N. Patel, et al. "Novel magnetic block states in low-dimensional iron-based superconductors." In: *Phys. Rev. Lett.* 123.2 (2019), p. 027203. DOI: 10.1103/PhysRevLett.123.027203 (cit. on p. 21).

[147] Y. Zhang, L. Lin, J.-J. Zhang, et al. "Pressure-driven phase transition from antiferromagnetic semiconductor to nonmagnetic metal in the two-leg ladders AFe_2X_3 (A= Ba, K; X= S, Se)." In: *Phys. Rev. B* 95.11 (2017), p. 115154. DOI: 10.1103/PhysRevB.95.115154 (cit. on p. 22).

[148] S. Chi, Y. Uwatoko, H. Cao, et al. "Magnetic precursor of the pressure-induced superconductivity in Fe-ladder compounds." In: *Phys. Rev. Lett.* 117.4 (2016), p. 047003. DOI: 10.1103/PhysRevLett.117.047003 (cit. on p. 22).

[149] S. Wu, J. Yin, T. Smart, et al. "Robust block magnetism in the spin ladder compound $BaFe_2Se_3$ under hydrostatic pressure." In: *Phys. Rev. B* 100.21 (2019), p. 214511. DOI: 10.1103/PhysRevB.100.214511 (cit. on pp. 22, 23, 81, 82).

[150] G Lawes, A. B. Harris, T. Kimura, et al. "Magnetically driven ferroelectric order in $Ni_3V_2O_8$." In: *Phys. Rev. Lett.* 95.8 (2005), p. 087205. DOI: 10.1103/PhysRevLett.95.087205 (cit. on p. 24).

[151] M. Kenzelmann, A. B. Harris, S Jonas, et al. "Magnetic inversion symmetry breaking and ferroelectricity in $TbMnO_3$." In: *Phys. Rev. Lett.* 95.8 (2005), p. 087206. DOI: 10.1103/PhysRevLett.95.087206 (cit. on p. 24).

[152] I. A. Sergienko, C. Şen, and E. Dagotto. "Ferroelectricity in the magnetic E-phase of orthorhombic perovskites." In: *Phys. Rev. Lett.* 97.22 (2006), p. 227204. DOI: 10.1103/physrevlett.97.227204 (cit. on p. 24).

[153] Y. T. Chan, S. Roh, S. Shin, et al. "Three-dimensional hopping conduction triggered by magnetic ordering in the quasi-one-dimensional iron-ladder compounds $BaFe_2S_3$ and $BaFe_2Se_3$." In: *Phys. Rev. B* 102.3 (2020), p. 035120. DOI: 10.1103/PhysRevB.102.035120 (cit. on p. 25).

[154] K. Du, L. Guo, J. Peng, et al. "Direct visualization of irreducible ferrielectricity in crystals." In: *npj Quantum Mater.* 5.1 (2020), pp. 1–7. DOI: 10.1038/s41535-020-00252-y (cit. on pp. 25, 63, 65, 72).

[155] F. Du, K. Ohgushi, Y. Nambu, et al. "Stripelike magnetism in a mixed-valence insulating state of the Fe-based ladder compound $CsFe_2Se_3$." In: *Phys. Rev. B* 85.21 (2012), p. 214436. DOI: 10.1103/PhysRevB.85.214436 (cit. on p. 25).

[156] J. Caron, J. Neilson, D. Miller, et al. "Orbital-selective magnetism in the spin-ladder iron selenides $Ba_{1-x}K_xFe_2Se_3$." In: *Phys. Rev. B* 85.18 (2012), p. 180405. DOI: 10.1103/PhysRevB.85.180405 (cit. on pp. 25–27, 63, 82).

[157] M. Wang, M. Yi, S. Jin, et al. "Spin waves and magnetic exchange interactions in the spin-ladder compound $RbFe_2Se_3$." In: *Phys. Rev. B* 94.4 (2016), p. 041111. DOI: 10.1103/PhysRevB.94.041111 (cit. on p. 25).

[158] K. Klepp, W Sparlinek, and H Boller. "Mixed valent ternary iron chalcogenides: AFe_2X (A= Rb, Cs; X= Se, Te)." In: *J. Alloys Compd.* 238.1-2 (1996), pp. 1–5. DOI: 10.1016/0925-8388(95)02087-X (cit. on p. 26).

[159] T. Balić-Žunić, L. Karanović, and D. Poleti. "Crystal Structure of Picotpaulite, $TlFe_2S_3$, from Allchar, FYR Macedonia." In: *Acta Chimica Slovenica* 55.4 (2008) (cit. on p. 26).

[160] G. Amthauer and K Bente. "Mixed-valent iron in synthetic rasvumite, KFe_2S_3." In: *Naturwissenschaften* 70.3 (1983), pp. 146–147. DOI: 10.1007/BF00401605 (cit. on p. 26).

[161] R. H. Mitchell, K. C. Ross, and E. G. Potter. "Crystal structures of $CsFe_2S_3$ and $RbFe_2S_3$: synthetic analogs of rasvumite KFe_2S_3." In: *J Solid State Chem* 177.6 (2004), pp. 1867–1872. DOI: 10.1016/j.jssc.2004.01.007 (cit. on p. 26).

[162] T. Hawai, Y. Nambu, K. Ohgushi, et al. "Temperature and composition phase diagram in the iron-based ladder compounds $Ba_{1-x}Cs_xFe_2Se_3$." In: *Phys. Rev. B* 91.18 (2015), p. 184416. DOI: 10.1103/PhysRevB.91.184416 (cit. on p. 26).

[163] T. Hawai, C. Kawashima, K. Ohgushi, et al. "Pressure-Induced Metallization in Iron-Based Ladder Compounds $Ba_{1-x}Cs_xFe_2Se_3$." In: *J. Phys. Soc. Japan* 86.2 (2017), p. 024701. DOI: 10.7566/JPSJ.86.024701 (cit. on p. 27).

[164] H. Takahashi, R. Kikuchi, C. Kawashima, et al. "Pressure-Induced Superconductivity in Iron-Based Spin-Ladder Compound $BaFe_{2+\delta}(S_{1-x}Se_x)_3$." In: *Materials* 15.4 (2022), p. 1401. DOI: 10.3390/ma15041401 (cit. on pp. 27–29).

[165] F. Du, Y. Hirata, K. Matsubayashi, et al. "Doping-and pressure-induced change of electrical and magnetic properties in the Fe-based spin-ladder compound $BaFe_2Se_3$." In: *Phys. Rev. B* 90.8 (2014), p. 085143. DOI: 10.1103/PhysRevB.90.085143 (cit. on p. 27).

[166] R. D. Shannon. "Revised effective ionic radii and systematic studies of interatomic distances in halides and chalcogenides." In: *Acta crystallographica section A: crystal physics, diffraction, theoretical and general crystallography* 32.5 (1976), pp. 751–767. DOI: 10.1107/S0567739476001551 (cit. on p. 27).

[167] J. Yu, M. Wang, B. A. Frandsen, et al. "Structural, magnetic, and electronic evolution of the spin-ladder system $BaFe_2S_{3-x}Se_x$ with isoelectronic substitution." In: *Phys. Rev. B* 101.23 (2020), p. 235134. DOI: 10.1103/PhysRevB.101.235134 (cit. on p. 28).

[168] S. Imaizumi, T. Aoyama, R. Kimura, et al. "Structural, electrical, magnetic, and optical properties of iron-based ladder compounds $BaFe_2(S_{1-x}Se_x)_3$." In: *Phys. Rev. B* 102.3 (2020), p. 035104. DOI: 10.1103/PhysRevB.102.035104 (cit. on p. 28).

[169] H. Sun, X. Li, Y. Zhou, et al. "Nonsuperconducting electronic ground state in pressurized $BaFe_2S_3$ and $BaFe_2S_{2.5}Se_{0.5}$." In: *Phys. Rev. B* 101.20 (2020), p. 205129. DOI: 10.1103/PhysRevB.101.205129 (cit. on p. 28).

[170] F. Du, Y. Ueda, and K. Ohgushi. "Large Magnon Contributions to Thermal Conductance in Quasi-One-Dimensional Fe-Based Ladder Compounds $BaFe_2(S_{1-x}Se_x)_3$." In: *Phys. Rev. Lett.* 123.8 (2019), p. 086601. DOI: 10.1103/PhysRevLett.123.086601 (cit. on p. 28).

[171] G. L. Squires. *Introduction to the Theory of Thermal Neutron Scattering*. 3rd ed. Cambridge University Press, 2012. DOI: 10.1017/CBO9781139107808 (cit. on pp. 31, 32).

[172] Y. Waseda, E. Matsubara, and K. Shinoda. *X-ray diffraction crystallography: introduction, examples and solved problems*. Springer Science & Business Media, 2011 (cit. on pp. 34, 39).

[173] H. Wondratschek, U. Müller, and U. internationale de cristallographie. *International tables for crystallography*. Wiley Online Library, 2004 (cit. on pp. 35, 41, 64).

[174] M. Eckert. *Max von Laue and the discovery of X-ray diffraction in 1912*. 2012. DOI: 10.1002/andp.201200724 (cit. on p. 41).

[175] W. H. Bragg and W. L. Bragg. "The reflection of X-rays by crystals." In: *Proceedings of the Royal Society of London. Series A, Containing Papers of a Mathematical and Physical Character* 88.605 (1913), pp. 428–438. DOI: 10.1098/rspa.1913.0040 (cit. on p. 41).

[176] R. J. d. C. Roque. "X-ray imaging using 100 μm thick Gas Electron Multipliers operating in Kr-CO_2 mixtures." PhD thesis. Universidade de Coimbra, 2018 (cit. on pp. 42, 43).

[177] J. A. Seibert. "X-ray imaging physics for nuclear medicine technologists. Part 1: Basic principles of x-ray production." In: *Journal of nuclear medicine technology* 32.3 (2004), pp. 139–147 (cit. on p. 43).

[178] S. Gaudet. "L'impact de la texture sur la Reaction en phase solide du Ni avec le Si." PhD thesis. École Polytechnique de Montréal, 2011 (cit. on p. 44).

[179] M. Ladd and R. Palmer. "Examination of single crystals: Optical and X-ray diffraction practice." In: *Structure Determination by X-ray Crystallography*. 2013, pp. 187–233. DOI: 10.1007/978-1-4614-3954-7_5 (cit. on p. 44).

[180] W. Peng. "Influence of the Pressure on the Multiferroicity of RMn_2O_5." PhD thesis. Université Paris-Saclay (ComUE), 2018 (cit. on p. 45).

[181] J. Chadwick. "Possible existence of a neutron." In: *Nature* 129.3252 (1932), pp. 312–312. DOI: 10.1038/129312a0 (cit. on p. 46).

[182] J. Terrell. "Neutron yields from individual fission fragments." In: *Phys. Rev.* 127.3 (1962), p. 880. DOI: 10.1103/PhysRev.127.880 (cit. on p. 48).

[183] T. Strassle, S Klotz, K Kunc, et al. "Equation of State of Lead from High-Pressure Neutron Diffraction up to 8.9 GPa and Its Implication for the NaCl Pressure Scale." In: *Phys. Rev. B* (2014), p. 8. DOI: 10.1103/PhysRevB.90.014101 (cit. on pp. 49, 78, 79).

[184] W. G. Marshall and D. J. Francis. "Attainment of near-hydrostatic compression conditions using the Paris-Edinburgh cell." In: *Journal of Applied Crystallography* 35.1 (2002), pp. 122–125. DOI: 10.1107/S0021889801018350 (cit. on p. 50).

[185] W. Zheng, V. Balédent, M. Lepetit, et al. "Room Temperature Polar Structure and Multiferroicity in $BaFe_2Se_3$." In: *Phys. Rev. B* 101 (2020), p. 020101. DOI: 10.1103/PhysRevB.101.020101 (cit. on p. 57).

[186] V. Petricek, M. Dusek, and L. Palatinus. "Crystallographic Computing System JANA2006: General features." In: *Z. Kristallogr.* 229 (2014), pp. 345–352. DOI: 10.1515/zkri-2014-1737 (cit. on p. 58).

[187] W. Schutte and J. De Boer. "Valence fluctuations in the incommensurately modulated structure of calaverite $AuTe_2$." In: *Acta Crystallographica Section B: Structural Science* 44.5 (1988), pp. 486–494. DOI: 10.1107/S0108768188007001 (cit. on p. 59).

[188] K. Hirota, D. E. Cox, J. E. Lorenzo, et al. "Dimerization of $CuGeO_3$ in the Spin-Peierls State." In: *Phys. Rev. Lett.* 73 (5 1994), pp. 736–739. DOI: 10.1103/PhysRevLett.73.736 (cit. on p. 59).

[189] S Ivantchev, E Kroumova, G Madariaga, et al. "SUBGROUPGRAPH: a computer program for analysis of group-subgroup relations between space groups." In: *Journal of Applied Crystallography* 33.4 (2000), pp. 1190–1191. DOI: 10.1107/S0021889800007135 (cit. on p. 61).

[190] M. Weseloh, V Balédent, W Zheng, et al. "Space Group Symmetry of $BaFe_2Se_3$: ab initio-Experiment Phonon Study." In: *arXiv preprint arXiv:2202.10039* (2022) (cit. on pp. 63, 72).

[191] V. Balédent, S. Chattopadhyay, P. Fertey, et al. "Evidence for Room Temperature Electric Polarization in RMn_2O_5 Multiferroics." In: *Phys. Rev. Lett.* 114 (11 2015), p. 117601. DOI: 10.1103/PhysRevLett.114.117601 (cit. on p. 63).

[192] W. Lv, A. Moreo, and E. Dagotto. "B_{1g}-like pairing states in two-leg ladder iron superconductors." In: *Phys. Rev. B* 88 (9 2013), p. 094508. DOI: 10.1103/PhysRevB.88.094508 (cit. on p. 66).

[193] H. Hegger, C. Petrovic, E. G. Moshopoulou, et al. "Pressure-Induced Superconductivity in Quasi-2D $CeRhIn_5$." In: *Phys. Rev. Lett.* 84 (21 2000), pp. 4986–4989. DOI: 10.1103/PhysRevLett.84.4986 (cit. on p. 68).

[194] G. Knebel, W. Knafo, A. Pourret, et al. "Field-Reentrant Superconductivity Close to a Metamagnetic Transition in the Heavy-Fermion Superconductor UTe_2." In: *J. Phys. Soc. Jpn.* 88 (2019), p. 063707. DOI: 10.7566/JPSJ.88.063707 (cit. on p. 68).

[195] Jérome, D., Mazaud, A., Ribault, M., et al. "Superconductivity in a synthetic organic conductor $(TMTSF)_2PF_6$." In: *J. Physique Lett.* 41.4 (1980), pp. 95–98. DOI: 10.1051/jphyslet:0198000410409500 (cit. on p. 68).

[196] Y. Uemura. "Energy-Scale Phenomenology and Pairing via Resonant Spin–Charge Motion in FeAs, CuO, Heavy-Fermion and Other Exotic Superconductors." In: *Physica B Condens. Matter* 404 (2009), pp. 3195–3201. DOI: 10.1016/j.physb.2009.07.110 (cit. on p. 68).

[197] H. Chen, Y. Ren, Y. Qiu, et al. "Coexistence of the Spin-Density Wave and Superconductivity in $Ba_{1-x}K_xFe_2As_2$." In: *EPL* 85 (2009), p. 17006. DOI: 10.1209/0295-5075/85/17006 (cit. on p. 68).

[198] S. Sanna, G. Allodi, G. Concas, et al. "Nanoscopic Coexistence of Magnetism and Superconductivity in $YBa_2Cu_3O_{6+x}$ Detected by Muon Spin Rotation." In: *Phys. Rev. Lett.* 93 (2004), p. 207001. DOI: 10.1103/PhysRevLett.93.207001 (cit. on p. 68).

[199] J. Rodríguez-Carvajal. "Recent Advances in Magnetic Structure Determination by Neutron Powder Diffraction." In: *Physica B Condens. Matter* 192 (1993), pp. 55–69. DOI: 10.1016/0921-4526(93)90108-I (cit. on pp. 69, 77).

[200] D. B. Litvin. "Magnetic group tables." In: *IUCr e-book. Freely available from http://www. iucr. org/publ/978-0-9553602-2-0* (2013) (cit. on p. 71).

[201] J. Perez-Mato, S. Gallego, E. Tasci, et al. "Symmetry-based computational tools for magnetic crystallography." In: *Annual Review of Materials Research* 45 (2015), pp. 217–248. DOI: 10.1146/annurev-matsci-070214-021008 (cit. on p. 71).

[202] C. Prescher and V. B. Prakapenka. "DIOPTAS: a program for reduction of two-dimensional X-ray diffraction data and data exploration." In: *High Pressure Research* 35.3 (2015), pp. 223–230. DOI: 10.1080/08957959.2015.1059835 (cit. on p. 77).

[203] P. Vinet, J. R. Smith, J. Ferrante, et al. "Temperature effects on the universal equation of state of solids." In: *Phys. Rev. B* 35.4 (1987), p. 1945. DOI: 10.1103/PhysRevB.35.1945 (cit. on p. 77).

[204] J.-P. Rueff, J. M. Ablett, D. Céolin, et al. "The GALAXIES beamline at the SOLEIL synchrotron: inelastic X-ray scattering and photoelectron spectroscopy in the hard X-ray range." In: *Journal of Synchrotron Radiation* 22.1 (2015), pp. 175–179. DOI: 10.1107/S160057751402102X (cit. on p. 78).

[205] H. Yamaoka, Y. Yamamoto, J.-F. Lin, et al. "Electronic structures and spin states of $BaFe_2As_2$ and $SrFe_2As_2$ probed by x-ray emission spectroscopy at Fe and As K-absorption edges." In: *Phys. Rev. B* 96 (8 2017), p. 085129. DOI: 10.1103/PhysRevB.96.085129 (cit. on p. 79).

[206] B. W. Lebert, V. Balédent, P. Toulemonde, et al. "Emergent high-spin state above 7 GPa in superconducting FeSe." In: *Phys. Rev. B* 97 (18 2018), p. 180503. DOI: 10.1103/PhysRevB.97.180503 (cit. on p. 79).

[207] J.-P. Rueff, C.-C. Kao, V. V. Struzhkin, et al. "Pressure-Induced High-Spin to Low-Spin Transition in FeS Evidenced by X-Ray Emission Spectroscopy." In: *Phys. Rev. Lett.* 82 (1999), pp. 3284–3287. DOI: 10.1103/PhysRevLett.82.3284 (cit. on p. 82).

[208] M. R. Norman. "Colloquium: Herbertsmithite and the search for the quantum spin liquid." In: *Rev. Mod. Phys.* 88 (2016), p. 041002. DOI: 10.1103/RevModPhys.88.041002 (cit. on p. 83).

[209] J.-F. Lin, H. Watson, G. Vankó, et al. "Intermediate-spin ferrous iron in lowermost mantle post-perovskite and perovskite." In: *Nature Geoscience* 1 (2008), pp. 688–691. DOI: doi.org/10.1038/ngeo310 (cit. on p. 84).